UNIVERSITY OF CALIFORNIA SAN DIEGO

Theoretical Modeling of Water Confined in Metal-Organic Frameworks for Atmospheric Water Capture

A dissertation submitted in partial satisfaction of the
requirements for the degree Doctor of Philosophy

in

Chemistry

by

Kelly Marie Hunter

Committee in charge:

Professor Francesco Paesani, Chair
Professor Partho Ghosh
Professor Shirley Meng
Professor John Weare
Professor Wei Xiong

2022

The dissertation of Kelly Marie Hunter is approved, and it is acceptable in quality and form for publication on microfilm and electronically.

University of California San Diego

2022

DEDICATION

To my Mom and Dad. Thank you for being my biggest supporters in everything I have done. I love you more than words could every say.

TABLE OF CONTENTS

LIST OF FIGURES

LIST OF TABLES

ACKNOWLEDGEMENTS

First and foremost, I would like to thank my advisor Francesco Paesani. Grad school would not have been possible without your endless support. Thank you for always inspiring me to discover more. I feel so lucky to have been a part of your group for the past five years and to have learned from all your knowledge and expertise. Thank you for always encouraging me to follow my passions in research and in teaching. I am truly thankful to have you as an advisor!

I would also like to thank all the members of the Paesani Lab, both past and present, for being the best coworkers throughout grad school. Thank you for all the helpful science discussions as well as all the fun coffee runs, boba runs, and lunchtime meals shared together. Pirates forever! I would like to give a special thank you to Kartik and Teri for all the support and encouragement throughout grad school. I couldn't imagine anyone better to journey with through the past five years.

Furthermore, I would like to thank all my friends. To my UCSD friends, thank you for all the fun adventures getting out of lab together. I am so grateful for all your support as we have navigated our time in grad school. To my Newman friends, thank you for offering me a community of friendship and belonging, a place I could always turn to for comfort. Finally, to my LMU friends, thank you for sticking with me throughout grad school, for the phone calls catching up, and for always being there for me.

I would not be who I am today without the love and support of my family. To my extended family, thank you for encouraging me from a young age to pursue my passion in science. It is all of you who helped transform me into the person and scientist that I currently am. Words cannot express how grateful I am to each and every one of you. To my siblings Matt, Melissa, and Nicole, thank you for the endless laughs. Those bursts of entertainment throughout grad school have helped propel me forward. Thank you for encouraging me to achieve all that I can, I am so thankful to call you my siblings. The biggest thank you of all goes to my Mom and Dad. The two of you have had the biggest influence on me throughout my entire life. Thank you for giving me

every chance and opportunity to succeed. You have been my two biggest inspirations and role models; if I could be half the person that you are, I will know that my life has been a success. Thank you for supporting me in everything I have done, from school to sports and all the other activities I was involved in. I feel like the luckiest person in the world to have the two of you as parents. I am eternally grateful for you, and I love you.

Finally, I would like to thank my best friend and partner-in-crime Steven. I can't begin to express how much your support has meant to me over these last few years. Thank you for always motivating and inspiring me. The passion you have for your work has made me more passionate about the science I am doing. Thank you for all the coffee runs, the delicious meals, the movie nights, and all the adventures throughout grad school. I truly could not have made it here without you. Thank you for always being there for me, I can't wait to see what life has in store for us together.

Chapter 2, in full, is a reprint of the material as it appears in "Disentangling Coupling Effects in the Infrared Spectra of Liquid Water", Hunter, K.M.; Shakib, F.A.; Paesani, F.; J. Phys. Chem. B, 122, 10754-10761, 2018. The dissertation author was the primary investigator and author of this paper.

Chapter 3, in full, is a reprint of the material as it appears in "Hydrogen Bonding Structure of Confined Water Templated by a Metal-Organic Framework with Open Metal Sites", Rieth, A.J.; Hunter, K.M.; Dincă, M.; Paesani, F.; Nat. Commun., 10, 4771, 2019. The dissertation author was the co-primary investigator and co-author of this paper.

Chapter 4, in full, is a reprint of the material as it appears in "Simulation Meets Experiment: Unraveling the Properties of Water in Metal-Organic Frameworks through Vibrational Spectroscopy", Hunter, K.M.; Wagner, J.C.; Kalaj, M.; Cohen, S.M.; Xiong, W.; Paesani, F.; J. Phys. Chem. C, 125, 12451-12460, 2021. The dissertation author was the primary investigator and author of this paper.

Chapter 5, in full, is a reprint of the material as it appears in "Water Capture Mechanisms

at Zeolitic Imidazolate Framework Interfaces", Wagner, J.C.; Hunter, K.M.; Paesani, F.; Xiong, W.; J. Am. Chem. Soc., 143, 50, 21189-21194, 2021. The dissertation author was the co-primary investigator and co-author of this paper.

Chapter 6, in full, is a reprint of the material as it is being prepared for publication in "Molecular Mechanisms of Water Harvesting in the Ni_2X_2BTDD (X = F, Cl, Br) Metal-Organic Frameworks", Hunter, K.M.; Paesani, F. The dissertation author is the primary investigator and author of this paper.

VITA

2017	Bachelor of Science in Biochemistry, Loyola Marymount University
2017-2018	Teaching Assistant, Department of Chemistry and Biochemistry, University of California San Diego
2019	Master of Science in Chemistry, University of California San Diego
2022	Doctor of Philosophy in Chemistry, University of California San Diego

PUBLICATIONS

Hunter, K.M., Paesani, F. "Molecular Mechanisms of Water Harvesting in the Ni_2X_2BTDD (X = F, Cl, Br) Metal-Organic Frameworks." *In preparation.*

Gartner III, T.E., Hunter, K.M., Lambros, E., Caruso, A., Riera, M., Medders, G.R., Panagiotopoulos, A.Z., Debenedetti, P. G., Paesani, F. "The Anomalies and Local Structure of Liquid Water from Boiling to the Supercooled Regime as Predicted by the Many-Body MB-pol Model." *J. Phys. Chem. Lett.,* 13, 3652-3658, **2022.**

Wagner, J.C., Hunter, K.M., Paesani, F., Xiong, W. "Water Capture Mechanisms at Zeolitic Imidazolate Framework Interfaces." *J. Am. Chem. Soc.,* 143, 50, 21189-21194, **2021.**

Hunter, K.M., Wagner, J.C., Kalaj, M., Cohen, S.M., Xiong, W., Paesani, F. "Simulation Meets Experiment: Unraveling the Properties of Water in Metal-Organic Frameworks through Vibrational Spectroscopy." *J. Phys. Chem. C* 125, 12451-12460, **2021.**

*Easley, C.J., *Erickson, B.A., *Hunter, K.M. "Viewpoints on the 2020 Pacific Conference on Spectroscopy and Dynamics." *J. Phys. Chem. A* 124, 14, 2731-2735, **2020.** *Equal contributions.

*Rieth, A.J., *Hunter, K.M., Dincă, M., Paesani, F. "Hydrogen Bonding Structure of Confined Water Templated by a Metal-Organic Framework with Open Metal Sites." *Nat. Commun.* 10, 4771, **2019.** *Equal contributions.

Hunter, K.M., Shakib, F.A., Paesani, F. "Disentangling Coupling Effects in the Infrared Spectra of Liquid Water." *J. Phys. Chem. B* 122, 10754-10761, **2018.**

ABSTRACT OF THE DISSERTATION

Theoretical Modeling of Water Confined in Metal-Organic Frameworks for Atmospheric Water Capture

by

Kelly Marie Hunter

Doctor of Philosophy in Chemistry

University of California San Diego, 2022

Professor Francesco Paesani, Chair

Water is essential to life, yet a majority of people in the world currently experience water scarcity. New methods of obtaining clean drinking water are required so that all people may have access to safe water. The process of atmospheric water capture, or harvesting water from the air, has emerged as one of the most promising methods for obtaining clean water. Metal-organic frameworks (MOFs) are materials that can operate at a wide range of temperatures and quantity of water in the atmosphere, being able to function in water harvesting. Therefore, it is necessary to understand the properties of water confined in MOFs to obtain an overall depiction of atmospheric water capture. In this work, we investigate the behavior of both bulk and confined water through

molecular dynamics simulations. Developing accurate models for MOFs, computer simulations then provide a molecular-level picture of water present in various environments. In combination with experiment, we unravel the mechanism of pore filling in various MOFs. Systems that have open metal sites allow water to form strong interactions with the framework, serving as nucleation sites for water adsorption. Water also exhibits different properties in various regions of these MOFs with large pore spaces, having limited mobility near the MOF interface but resembling bulk water in the middle of the pore. On the other hand, MOFs that do not have open metal sites but contain hydrophilic groups allow water clusters to form in single pores, filling one pore at a time rather than all pores simultaneously. It is further investigated how the interactions between water and the MOF are critical for a correct description of these systems in order to achieve agreement with experimental properties. The comparison of water–water and MOF–water interactions reveals the strongest properties that contribute to water adsorption, which vary between different MOFs. Utilizing accurate models for both water and MOFs, we are able to obtain a deeper understanding of water confined in MOFs. With this information, future water harvesting MOFs can be developed that can provide a source of clean drinking water to the world.

Chapter 1

Introduction

1.1 Water in the world

Water is one of the most ubiquitous molecules in nature, yet over fifty percent of the world's population are currently experiencing water stress,[2] making water scarcity one of society's most prominent issues today. This matter is even further intensified for certain geographical regions of the world; land-locked areas that are far from bodies of water, such as rivers, lakes, and oceans, tend to have the highest water vulnerability and most limited access to clean drinking water.[3] These regions are also typically the hottest, driest areas of the planet.[2,3] Therefore, there is an urgent need to develop methods and technologies that can provide safe drinking water to all areas the world.

Current technologies that can obtain and purify drinking water include desalination,[4–7] wastewater treatment,[8–11] and atmospheric water capture.[2,12,13] While desalination can remove the contaminants present in salt water,[5] it traditionally suffers high-energy costs and is only possible in coastal regions near large bodies of water.[2,4,6] Additionally, many desalination membranes have a selectivity/permeability trade-off.[14] Permeable membranes allow water molecules to pass through them but may not be selective to remove certain contaminants from water, of which there

exists a greater need.[14] Wastewater treatment further suffers this selectivity/permeability trade-off,[11] incurs high-energy costs,[8] and often has to go through multiple iterations of purification to remove a large number of pollutants present in wastewater.[9] Finally, while atmospheric water capture has presented some challenges, it also holds much promise. Water harvesting through fog collection can be difficult as it requires the constant presence of fog, which restricts it to areas that frequently have fog, such as coastal regions.[2,12] Water can also be cooled below its dew point, but cooling can require large amounts of energy or heat depending on the local climate of the area.[12] Capture of atmospheric water by an adsorbent, however, is one of the most promising techniques as adsorption can occur at multiple temperature and humidity ranges, which reflect the different environments and areas of the world.[2] Deserts and arid regions typically vary between 5-35% relative humidity (RH), a measure of the water content in the air.[15] It is therefore essential to investigate materials that can adsorb water when there is little water vapor in the atmosphere at low RH values. Utilizing a material that can capture and release water at various temperatures and humidities would provide a source of clean drinking water to every area of the world.

1.2 Metal-organic frameworks (MOFs)

Metal-organic frameworks (MOFs) are a popular class of materials that are used in a variety of applications such as catalysis,[16–20] liquid and gas adsorption,[2,21–24] chemical separation,[9,11,25–27] drug delivery,[28–30] electronic devices,[31–33] and in countless other areas. The diverse chemical nature of MOFs are what make them of interest and application to many different fields. MOFs are constructed from a metal-containing unit, also called a secondary building unit (SBU), and an organic linker, which combine to form three-dimensional repeating structures that have large surface areas and high porosity.[34] Although MOFs are synthesized from two components, the variation of the metal center or the modification of the organic linker creates MOFs with different structures, establishing a vast number of MOFs that have unique properties. For example,

utilizing different metal centers (Al, Cr, Fe, etc.) in the MIL (Matériaux de l'Institut Lavoisier) family of MOFs affects the adsorption and catalytic properties of each MOF.[35] Furthermore, changing the functional group on the organic linker (methyl, ethyl, carboxyaldehyde, etc.) of zeolitic imidazolate frameworks (ZIFs) produces MOFs with different three-dimensional structures and adsorption capacities.[36] Finally, within the UiO (Universitetet i Oslo) family of MOFs, incorporating one benzene ring (UiO-66), two benzene rings (UiO-67), or three benzene rings (UiO-68) into a MOF structure results in different water adsorption properties for each MOF.[37] Exchanging any component of the material affects its structure and properties; it is therefore essential to study the properties of various MOFs for their use in atmospheric water capture.

MOFs have been widely used in liquid and gas adsorption because of their large pore volumes and tunable structures,[21–24] which make them promising candidates for atmospheric water capture.[2] However, many MOFs are not stable in water; water can displace the organic linker to interact with the metal center, causing pore collapse and preventing further use of the MOF.[38–40] It is therefore imperative to utilize MOFs that remain stable in water for long periods of time during water adsorption. Properties such as the basicity of the organic linker, shielding of metal–linker coordination sites, and the extent of coordination between the metal and the linker all contribute to the stability of MOFs in water.[39] While some MOFs have metal centers that are fully coordinated to the organic linker, other MOFs contain open metal sites, which are not fully coordinated to linkers.[39,40] These systems allow water to interact with and bind directly to the metal center, creating a strong MOF–water interaction which can lead to water adsorption at low RH values.[40,41] Adsorption at low RH is essential for MOFs to harvest water from the atmosphere in arid desert regions that vary between 5-35% RH.[15]

Another important consideration in atmospheric water capture is the total amount of water a MOF can adsorb, which often relies on the size of the pore.[2] While large pore sizes are ideal for maximum water uptake, releasing the water from these pores could exert forces on the pore walls that can lead to pore collapse,[42] creating a limit to the size of the pore. For example,

ZIF-90, which will be discussed in Chapters 4-5, has spherical pores with a diameter of 11 Å.[43] While ZIF-90 adsorbs water around 30% RH, ZIF-90 can only adsorb about 30% of its weight in water.[36] On the other hand, Ni_2F_2BTDD and Ni_2Cl_2BTDD, which will be discussed in Chapter 6, have cylindrical pores with diameters of 23 Å.[44] These two systems can adsorb water at 32% RH, and they can also adsorb over 100% of their weight in water, one of the largest values for MOFs.[44] This balance between adsorption at low RH and total amount of water adsorption is critical for atmospheric water capture so that MOFs can provide clean drinking water.

Obtaining a complete understanding of the process of atmospheric water capture is essential to develop MOFs that can efficiently harvest water from the air. Here, theoretical and computational chemistry can contribute by providing a molecular-level insight into water adsorbed in MOFs. Simulations of water filling the MOF pores depict how water interacts with and binds to the MOF, allowing future MOFs to be designed that have similar or different interactions. Furthermore, the structural, dynamical, and thermodynamic properties of water in MOFs can be calculated to obtain an understanding of how water behaves while confined in the MOF pores. A comparison of MOF–water interactions along with water–water interactions is important to reveal how water first fills the pores, interacting with the MOF interface, but then nucleates pore filling by forming hydrogen bonds with other water molecules. A detailed, molecular-level description of both water and MOFs is therefore necessary to understand the process of atmospheric water capture and to develop future water harvesting MOFs that can adsorb large amounts of water at low RH values.

1.3 The many-body potential energy function (MB-pol)

In order to study atmospheric water capture, it is imperative to have an accurate understanding of how water behaves in various environments. Although water contains only three atoms, one oxygen atom and two hydrogen atoms, the properties of water are unique compared to

other molecules.[45] These anomalous properties, such as the density maximum at 4 °C and high surface tension, have often been attributed to the formation of strong hydrogen bonds with other water molecules.[45] The properties of small water clusters as well as bulk water have been well described by both theory and experiment.[46–51] However, describing the properties of water in confinement, specifically water confined in MOFs, requires much attention, needing an accurate description of water, the MOF, and the interactions between the two. Therefore, an understanding of the properties of bulk water (Chapter 2) is required in order to describe the behavior of water in confinement (Chapters 3-6).

Multiple potential energy functions (PEFs) exist that accurately describe the properties of water, such as CC-pol,[52–54] WHBB,[55–57] HBB2-pol,[58,59] and MB-pol.[60–62] As a many-body PEF, MB-pol has been shown to correctly predict the properties of water from the gas to the condensed phase.[63] It is built upon a many-body expansion of the interaction energy as given by:

$$E_N = \sum_{i=1}^{N} V^{1B}(i) + \sum_{i<j}^{N} V^{2B}(i,j) + \sum_{i<j<k}^{N} V^{3B}(i,j,k) + ... + V^{NB}(1,...,N) \tag{1.1}$$

Equation 1.1 represents the total interaction energy for a generic N-molecule system, described as a sum of one-body (1B) monomer distortion energies, two-body (2B) pairwise interactions, up to N-body (NB) interaction energies.[63]

MB-pol can reproduce the vibration-rotation tunneling spectrum of the water dimer,[60] the energetics of small clusters,[61] the isomeric quantum equilibria and tunneling pathways of the water hexamer,[64,65] and the structural, thermodynamic, and dynamical properties of liquid water.[62,63] Furthermore, the energetics of the ice phases,[66] the X-ray absorption spectrum of liquid water,[67] and the electron affinity of water[68] have been reproduced. MB-pol has also been shown to accurately reproduce the THz spectra of the octamer cluster[69] and the vibrational spectra of water clusters,[60,65,70] liquid water,[71–74] the air/water interface,[75,76] and ice.[77–79] Therefore, MB-pol is an ideal model to describe the properties of water in various environments. When MB-pol is combined with accurate models for MOFs, a realistic picture of atmospheric water

capture can be obtained.

1.4 Force fields and force field development

1.4.1 Force fields

Similar to the PEFs that are used to simulate water, force fields can be developed and utilized to simulate various systems, including MOFs. A force field calculates the energy of a system based on its atomic coordinates at any point in time.[80] This energy consists of both bonded parameters (bonds, angles, dihedrals, impropers, inversions, etc.), which describe intramolecular distortions of a particular molecule, and nonbonded parameters (electrostatics and van der Waals (VDW)), which represent intermolecular interactions between similar or different molecules.[80] An example of the energy of a specific configuration given by a force field is:

$$V(r^N) = \sum_{bonds} \frac{k_i}{2}(l_i - l_{i,0})^2 + \sum_{angles} \frac{k_i}{2}(\theta_i - \theta_{i,0})^2 + \sum_{torsions} \frac{V_n}{2}\Big(1 + cos(n\omega - \gamma)\Big) + \sum_{i=1}^{N}\sum_{j=i+1}^{N}\Big(4\varepsilon_{ij}\Big[\Big(\frac{\sigma_{ij}}{r_{ij}}\Big)^{12} - \Big(\frac{\sigma_{ij}}{r_{ij}}\Big)^{6}\Big] + \frac{q_i q_j}{4\pi\varepsilon_0 r_{ij}}\Big) \tag{1.2}$$

where there is summation over all the bonds, angles, torsions, and electrostatic and VDW parameters of the system.[80] Equation 1.2 represents the potential energy of the system, which can be modified by using different functional forms to describe the various parameters in the force field. For example, bonds can be described through a harmonic potential (as used in Equation 1.2), through a Morse potential, or through another potential. Similarly, the VDW parameters can be represented by a Lennard-Jones potential (as used in Equation 1.2), a Buckingham potential, or any other VDW term.

Numerous force fields currently exist that can be used to describe a variety of chemical systems. Well-known force fields include the General Amber Force Field (GAFF)[81] and the

Universal Force Field (UFF).[82] These force fields have the benefit of being applicable to a wide range of systems, such as the organic linkers of MOFs, although they suffer from the transferability of not being able to describe the metal centers of MOFs, which have high coordination numbers and are often charged.[83,84] More specific force fields have therefore recently been developed to try to mitigate the lack of accuracy in describing the metal centers of MOFs. Force fields such as MOF-FF[85] and QuickFF,[83] extensions of UFF for MOFs (UFF4MOF),[84,86] and a zeolitic imidazolate framework force field (ZIF-FF)[87] have been used to describe the unique coordination environments of MOFs. While these force fields have been successful at describing the properties of certain MOFs, the high degree of variability in the components and structures of MOFs sometimes requires a greater level of specificity in their force field description.

1.4.2 Force field development

Two important factors to take into account for MOF force fields are framework flexibility, or the ability of MOF atoms to move and vibrate in solution, and polarizability, or the ability of MOF atoms to change charge. It has previously been shown that flexibility of the framework atoms can affect both the structure and dynamics of guest molecules adsorbed in MOFs,[88] so including this flexibility in the force field is essential. Framework polarizability, on the other hand, can affect the distribution of water molecules within the MOF pores.[89] However, MB-pol water molecules are both flexible and polarizable,[60–62] so using a non-polarizable force field for the MOF can still result in agreement with experimental properties, which will be shown in Chapters 3-6. The development of accurate, flexible, and non-polarizable force fields for MOFs that can be utilized with the MB-pol water model is needed. A systematic procedure for developing these force fields is also crucial so that the process can be applied to any number of MOFs with many different properties.

The general process for developing MOF force fields as used by our group is as follows. After optimization of the MOF structure, the charges are calculated for the atoms through

a periodic charge calculation (such as the density derived electrostatic and chemical DDEC charges)[90] or for a subset of the MOF atoms (such as the charge model 5 CM5 charge scheme).[91] All bonded parameters involving the organic linker are taken from GAFF.[81] However, all bonded parameters involving the metal center are fit using a genetic algorithm. After obtaining all the bonded parameters for the MOF, nonbonded parameters between water and the MOF need to be derived, which are represented through either Lorentz-Berthelot mixing rules or through fitting the metal–water interaction. With the force field developed for the MOF and MB-pol being utilized for water, comparison of the theoretical properties of water confined in the MOF can be compared to experiment. If theory and experiment do not agree, further refinement of the force field or the MOF–water interactions can be made until qualitative and quantitative agreement is reached. Details of this force field development process as well as the refinement of force fields are given in Chapters 3-6. In the future, this force field development process can be improved by adding polarizability to the MOF so that both water and the MOF are flexible and polarizable.

1.5 Summary

In the following chapters, the behavior of water in various environments is investigated. First, in Chapter 2, the properties of bulk water are studied to ensure that simulations are accurate and achieve agreement with experiment. Following the study of bulk water, water confined in various MOFs can be investigated. In Chapter 3, the Co_2Cl_2BTDD MOF is studied, dissecting the properties of water as a function of distance from the pore surface. Then, in Chapters 4 and 5, it is shown how the description of the interactions between water and ZIF-90 is essential to obtain quantitative agreement with experiment, as well as how the combination of theory and experiment can elucidate the mechanism of pore filling. Chapter 6 investigates how the structure of water varies in Ni_2X_2BTDD (X = F, Cl, Br), where only the halide atom is exchanged in the MOF structure. Finally, in Chapter 7, conclusions from all previous studies are drawn.

Chapter 2

Disentangling Coupling Effects in the Infrared Spectra of Liquid Water

2.1 Introduction

Despite its apparent simplicity, with only 3 atoms and 10 electrons, water displays a unique behavior across the phase diagram which still befuddles scientists. As the most essential liquid on Earth, water exhibits several anomalous properties that are directly related to its ability to form dynamic hydrogen-bond (H-bond) networks that continually fluctuate via the breaking and forming of H-bonds. Vibrational spectroscopy is a powerful tool to investigate both structure and dynamics of the H-bond network of water in different environments.[50,92–94] However, an unambigous assignment of the vibrational spectra of water is highly nontrivial due to the fluctuating nature of the H-bond network and the presence of both intramolecular and intermolecular couplings.

Through selective isotopic substitutions, different types of coupling within the H-bond network can be separated to allow for the investigation of both individual and multiple coupling effects at the same time. On the experimental side, infrared (IR) spectroscopy has been widely

used to probe either fully coupled or completely isolated OH stretches of neat H_2O or diluted HOD in D_2O solutions, respectively.[95–103] However, it has proven experimentally difficult to disentangle intermediate levels of couplings due to relatively fast H/D exchange in solution that effectively precludes the monitoring of OH stretches of diluted H_2O molecules in D_2O as well as diluted HOD molecules in H_2O, which would be ideal systems for independently characterizing intramolecular and intermolecular couplings, respectively. On the other hand, the majority of theoretical studies have focused on fully coupled or isolated OH stretches in order to provide molecular interpretations of the experimental spectra.[51,71,72,104–120] These limitations on both experimental and theoretical sides have so far prevented a quantitative assessment of coupling effects in the structural rearrangements of the water H-bond network.

The introduction of highly accurate many-body potential energy functions (PEFs) for water, such as CC-pol,[52–54] WHBB,[55–57] HBB2-pol,[58,59] and MB-pol,[60–63,121] has effectively transformed the landscape of water simulations, enhancing the prospect for predictive theoretical studies of water at the molecular level. Among the existing many-body PEFs, we and others have shown that MB-pol correctly predicts the properties of water from the gas to the condensed phase, reproducing the vibration-rotation tunneling spectrum of the water dimer,[60] the energetics of small clusters,[61] the isomeric quantum equilibria and tunneling pathways of the water hexamer,[64,65] structural, thermodynamic, and dynamical properties of liquid water,[62,63] and the energetics of the ice phases.[66] MB-pol has also been shown to accurately reproduce the THz spectra of the octamer cluster,[69] the infrared and Raman spectra of liquid water,[71–73] the temperature-dependence of the sum-frequency generation spectra of the air/water interface,[76] and the infrared and Raman spectra of ice I_h.[77] More recently, molecular configurations extracted from classical and path-integral molecular dynamics simulations with MB-pol have been used in many-body perturbation theory calculations to model the X-ray absorption spectrum of liquid water as well as to determine the electron affinity of water, both in the bulk and at the air/water interface.[67,68]

Building upon the demonstrated predictive power of MB-pol and taking advantage of the

fact that isotope exchange is a rare event in computer simulations of water, which is completely turned off when using non-dissociable models, we present a systematic investigation of IR OH-stretch lineshapes calculated for different isotopic mixtures. Specifically, we report the results of centroid molecular dynamics (CMD) simulations for four different solutions: neat H_2O, diluted HOD in H_2O, diluted H_2O in D_2O, and diluted HOD in D_2O, corresponding to solutions with fully coupled OH stretches, only intermolecularly coupled OH stretches, only intramolecularly coupled OH stretches, and fully decoupled OH stretches, respectively. The combination of MB-pol, a water model exhibiting chemical and spectroscopic accuracy, with quantum dynamics simulations carried out within the CMD formalism allows for unambiguously disentangling intramolecular and intermolecular coupling effects on both the frequency shift and intensity of the OH-stretch lineshape in liquid water, which has so far remained elusive. Furthermore, by combining the local mode[122,123] and local monomer[57] (LM) methods, calculations carried out on molecular configurations extracted along the CMD trajectories allow for further dissecting the IR OH-stretch lineshape by quantifying contributions due to Fermi resonances.

2.2 Computational Methods

To investigate coupling effects on the vibrational dynamics of the H-bond network in liquid water, four isotopic solutions (neat H_2O, diluted HOD in H_2O, diluted H_2O in D_2O, and diluted HOD in D_2O) with different degrees of intramolecular and intermolecular couplings, as depicted in Figure 2.1, are investigated. Within each solution, we focus our analysis on the OH stretch vibrations; for neat H_2O, we investigate both intramolecular and intermolecular couplings (Fig. 2.1a), for HOD in H_2O, we specifically monitor the OH vibrations of the "solute" HOD molecules which are intermolecularly coupled to the OH vibrations of the "solvent" H_2O molecules (Fig. 2.1b), for H_2O in D_2O, we consider the OH stretches of the "solute" H_2O molecules which are intramolecularly coupled but completely decoupled from the OD vibrations

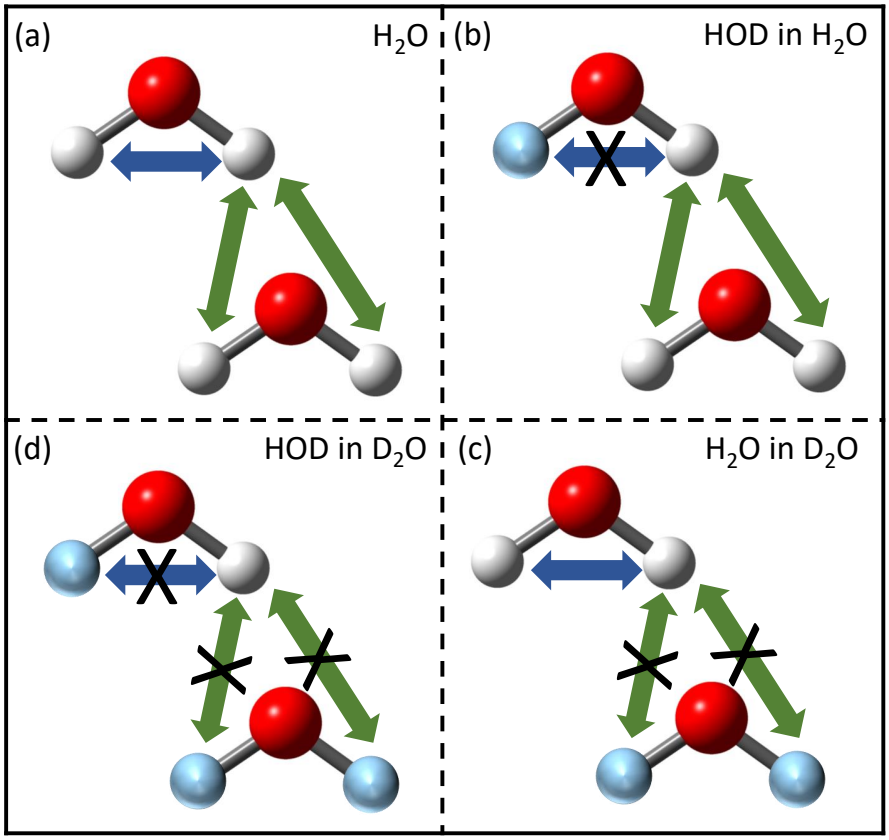

Figure 2.1: Depiction of the different coupling effects in the four isotopic solutions analyzed in this study. The oxygen atoms are shown in red, the hydrogen atoms in white, and the deuterium atoms in blue. The top left molecule in each panel represents the "solute" molecule being probed in the calculations of the corresponding IR OH-stretch lineshape, and the bottom right molecule is one of the "solvent" molecules. Blue arrows represent intramolecular coupling, and green arrows represent intermolecular coupling.

of the solvent D_2O molecules (Fig. 2.1c), and for HOD in D_2O, we investigate the uncoupled OH vibrations of the "solute" HOD molecule (Fig. 2.1d). Analogous simulations, presented in the Supporting Information, were also performed to characterize coupling effects on the OD-stretch vibrational dynamics.

Nuclear quantum effects (NQE) are accounted for within the CMD formalism, which approximates the exact quantum expressions in terms of phase space representations amenable to classical-like interpretations of the variables of interest.[124–128] In all CMD simulations, each atom is represented by a Feynman's ring-polymer discretized with 32 beads, and the centroid variables

are propagated according to the velocity-Verlet algorithm using the partially adiabatic separation scheme of Refs. 127 and 129, with an adiabaticity parameter $\gamma = 0.25$ and a time step of 0.05 fs. A Nosé-Hoover chain of four thermostats is attached to each degree of freedom to ensure adequate canonical sampling at 298.15 K. Short-range interactions are truncated at an atom-atom separation of 9.0 Å, while the electrostatic interactions are treated using the Ewald sum.[80] Each isotopic solution consists of 216 molecules total, with two "solute" molecules surrounded by 214 "solvent" molecules (e.g. two HOD molecules in 214 D_2O molecules) to mimic the 1% concentration typically used in experiments.[93] 20 independent CMD trajectories are collected for each isotopic solution, starting from initial configurations extracted from previous path-integral molecular dynamics (PIMD) simulations carried out for H_2O and D_2O solutions at the corresponding experimental densities.[72,73] Cubic simulation boxes with sides of 18.6428 Å and 18.6506 Å are thus used for isotopic mixtures with H_2O and D_2O as the "solvents", respectively.

In all simulations, the water interactions are described by MB-pol, a many-body PEF rigorously derived from the many-body expansion of the interaction energy between water molecules,[60–62] which has been shown to provide an accurate representation of water across different phases.[63] The IR spectra for all isotopic solutions are calculated within the time-dependent formalism according to

$$I_{IR}(\omega) = \left[\frac{2\omega}{3V\hbar c\varepsilon_0}\right] \tanh(\beta\hbar\omega) \int_{-\infty}^{\infty} dt\, e^{i\omega t} \langle \mu(0)\mu(t)\rangle \tag{2.1}$$

where V is the system volume, c is the speed of light in vacuum, ε_0 is the permittivity of free space, and $\beta = (k_B T)^{-1}$, with k_B being Boltzmann's constant. In Eq. 2.1, $\langle \mu(0)\mu(t)\rangle$ is the ensemble averaged quantum dipole-dipole time correlation function obtained for each isotopic solution by averaging $\mu(0)\mu(t)$ over the corresponding 20 independent CMD trajectories, with $\mu(t)$ given by the many-body MB-μ function introduced in Ref. 71. MB-μ includes explicit one-body (1B) and two-body (2B) terms, with all higher-order N-body (NB) terms being described by classical

induction.

Finally, to quantify Fermi resonance contributions deemed to be important to the H_2O IR lineshape,[130] local mode and local monomer (LM) calculations[57,122,123] are performed on molecular clusters consisting of 16 D_2O molecules around a H_2O molecule, which were extracted from the corresponding CMD simulations carried out for the diluted H_2O in D_2O solution. In the LM calculations, the coordinates of the D_2O molecules as well as the oxygen atom of the H_2O molecule are kept fixed to their CMD values, while constrained optimizations of the hydrogen positions are performed by interfacing the ORCA package[131] with our in-house MB-pol software.

2.3 Results and Discussion

To first assess the accuracy of our theoretical and computational approach, the IR lineshapes calculated from CMD simulations of neat H_2O and diluted HOD in D_2O solutions are compared with the corresponding experimental spectra in Figure 2.2. Similar comparisons were reported in different contexts in previous studies with MB-pol.[71,72] As discussed in detail in Refs. 71 and 72, MB-pol slightly underestimates the H-bond strength in liquid water, which results in OH stretching frequencies that are approximately 57 cm^{-1} blue-shifted compared to experiment. After accounting for this shift, overall good agreement is found between the theoretical and experimental lineshapes, which is nearly quantitative for the HOD in D_2O system. However, some noticeable differences exist in the low-frequency region of the neat H_2O lineshape with the CMD band lacking intensity between 3000 cm^{-1} and 3300 cm^{-1}, as originally observed in Ref. 71.

The IR lineshapes calculated for the "solute" molecules (i.e., H_2O or HOD) of the four different isotopic solutions are shown in Fig. 2.3. To further characterize the interplay between vibrational and electrostatic couplings, the IR lineshapes for each isotopic solution are calculated using different representations of the dipole moment in Eq. 2.1, corresponding to

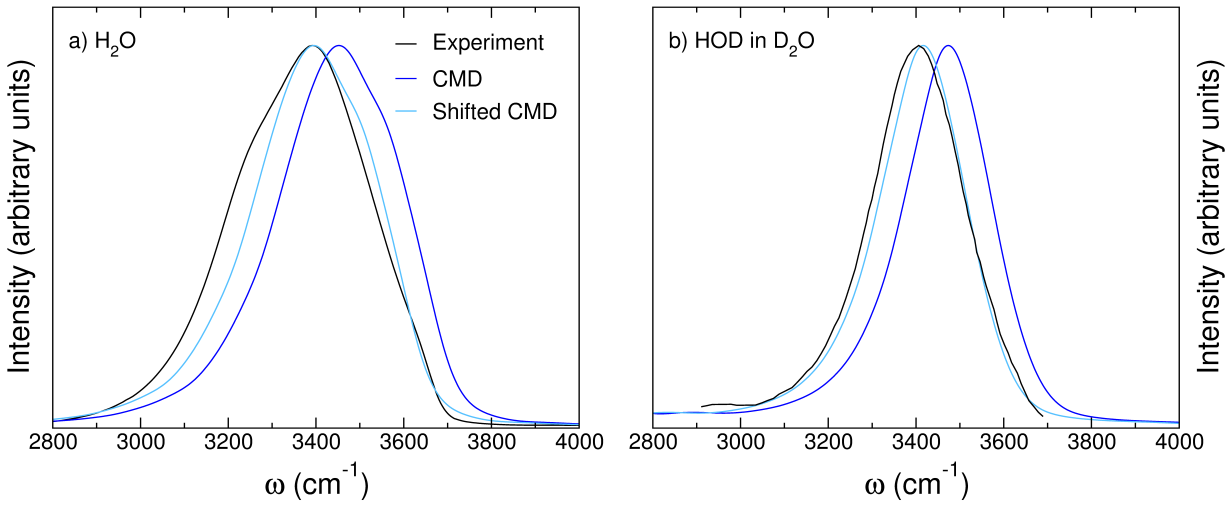

Figure 2.2: IR OH-stretch lineshapes (blue traces) calculated from CMD simulations of neat H_2O (a) and diluted HOD in D_2O (b) solutions compared with the corresponding experimental results (black traces) from Refs. 95 and 97, respectively. Also shown are the CMD lineshapes (light blue) red-shifted by 57 cm^{-1} to facilitate comparisons with the experimental results. See main text for details.

different approximations to many-body effects on the water dipole moment within the MB-μ expression.[71] Specifically, each panel of Fig. 2.3 shows comparisons between IR lineshapes computed using the gas-phase (1B) term (red traces), the 1B+NB representation including many-body effects through classical induction (green traces), and the full many-body (1B+2B+NB) MB-μ representation which, in addition to inductive many-body effects, accounts for explicit short-range 2B contributions (blue traces). In this analysis, all lineshapes are normalized with respect to the number of OH oscillators of the "solute" molecules to allow for comparisons of both frequency shifts and intensities as a function of different levels of coupling. The full-width at half maximum (fwhm) and frequency of maximum absorbance (fma) are calculated and compared among different approximations to the many-body dipole moment in Table 2.1. The fwhm for neat H_2O and HOD in D_2O calculated with the 1B+2B+NB representation of the dipole moment are 337 cm^{-1} and 237 cm^{-1}, respectively, which are in good agreement with the corresponding experimental values of 378 cm^{-1} and 255 cm^{-1}.[95,97]

Fig. 2.3 shows that, at the 1B level of electrostatic coupling (red traces), the IR lineshapes

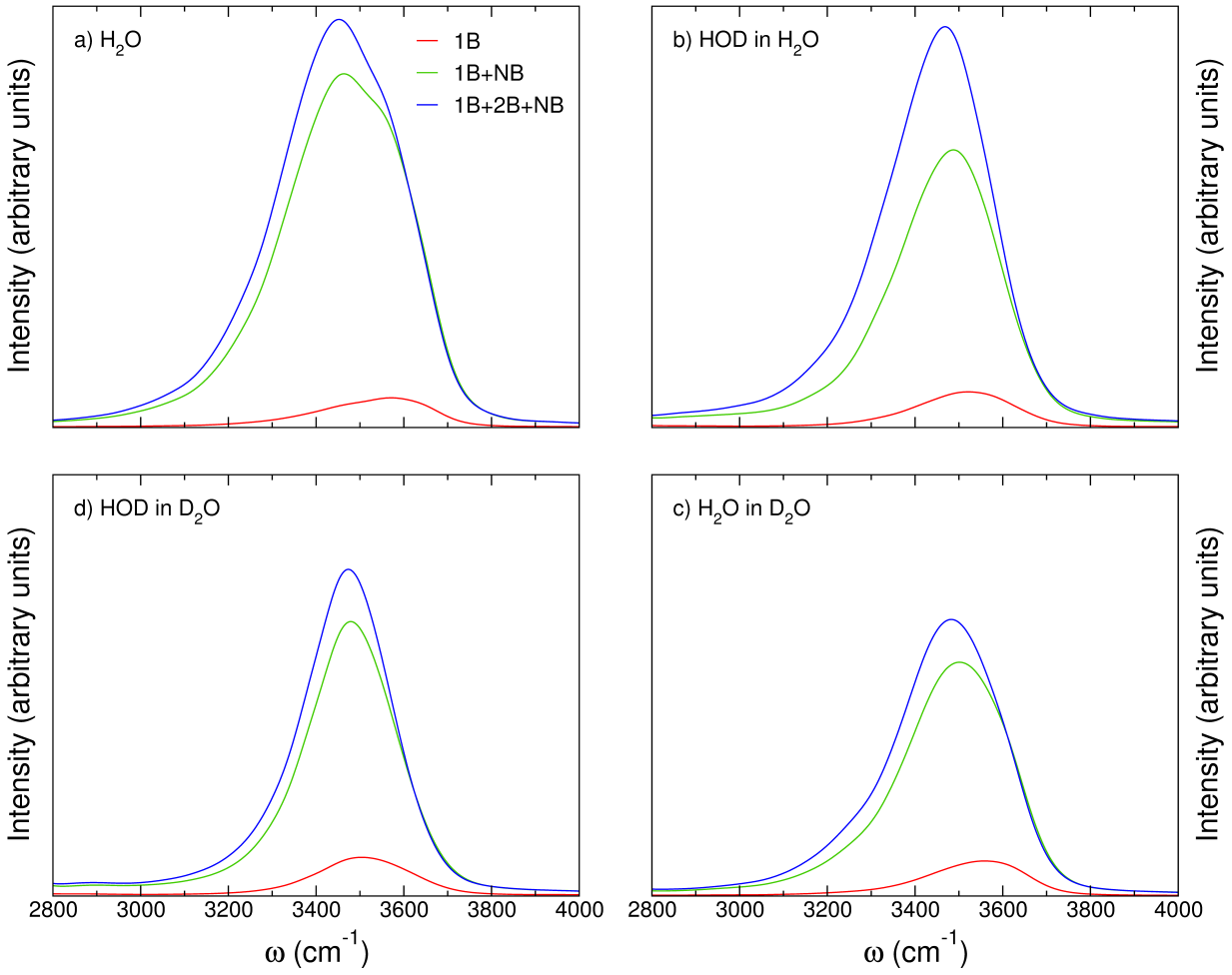

Figure 2.3: IR OH-stretch lineshapes calculated from CMD simulations of neat H_2O (a), diluted HOD in H_2O (b), diluted H_2O in D_2O (c), and diluted HOD in D_2O (d). For each isotopic solution, the OH-stretch lineshape is calculated using the 1B, 1B+NB, and 1B+2B+NB hierarchy of approximations to the dipole moment (see main text for details). All lineshapes are on the same intensity scale and are normalized to the number of OH oscillators of the "solute" molecule.

calculated for "solutes" with intramolecular coupling (i.e., neat H_2O and H_2O in D_2O) are the most blue-shifted. As discussed in Ref. 72, due to the lack of electrostatic coupling with the surrounding "solvent" molecules, these 1B lineshapes only report on "solute" dipole moment fluctuations associated with intramolecular distortions. Since changes in the 1B (gas-phase) dipole moment due to stretching and bending vibrations in solution are relatively smaller than those associated with induction interactions,[72] the transition dipole moment remains approximately constant, independently of the instantaneous "solute" configuration. This makes the 1B lineshapes

Table 2.1: Full-width at half maximum (fwhm) and frequency of maximum absorbance (fma) in cm^{-1} of the OH-stretch lineshape calculated for the four different isotopic solutions using the 1B, 1B+NB, and 1B+2B+NB hierarchy of approximations to the dipole moment (see main text for details).

	1B		1B+NB		1B+2B+NB	
	fwhm	fma	fwhm	fma	fwhm	fma
H_2O	294	3570	344	3463	337	3453
HOD in H_2O	260	3520	273	3486	281	3470
H_2O in D_2O	259	3560	287	3500	287	3483
HOD in D_2O	252	3503	239	3480	237	3473

effectively identical to the corresponding lineshapes calculated within the Condon approximation using the full many-body representation of the dipole moment.[72] The blue shifts observed in the 1B lineshapes of neat H_2O and H_2O in D_2O thus indicate that intermolecular coupling is responsible for slightly stronger H-bonds and, consequently, weaker OH bonds.

Inclusion of N-body electrostatic effects (green traces) results in an overall increase in intensity of all lineshapes. Specifically, the lineshape for the fully coupled neat H_2O solution exhibits the highest intensity, while the lowest intensity is found for the lineshape of the intramolecularly coupled H_2O in D_2O solution. The lineshapes for the intermolecularly coupled HOD in H_2O and fully decoupled HOD in D_2O solutions display nearly identical intensities. Comparisons with the corresponding 1B lineshapes demonstrate that N-body electrostatic effects are clearly responsible for significant redistribution of the IR intensity over the entire frequency range of the OH vibrations, resulting in changes to the lineshapes which directly correlate with the specific level of vibrational coupling present in each solution. In particular, the 1B+NB lineshapes of both solutions with intermolecular coupling (i.e., neat H_2O and HOD in H_2O) display relatively higher intensities between 3250 cm^{-1} and 3400 cm^{-1} (see Supporting Information for specific details). Since this frequency range is associated with stronger H-bonds, these results thus emphasize the importance of many-body electrostatic effects in the vibrational dynamics of strongly coupled OH stretches in liquid water. On the other hand, it should be noted that the lineshape of the intramolecularly coupled H_2O in D_2O solution grows in intensity below 3250

cm^{-1}.

When the dipole moments in Eq. 2.1 are represented by the full many-body MB-μ function, which includes a short-range 2B term in addition to a classical representation of many-body effects, further increase in the IR intensity is observed for the corresponding lineshapes (blue traces) shown in Fig. 2.3, particularly in the low-frequency region. The comparison among IR lineshapes calculated as a function of the level of electrostatic coupling (Table 2.1) shows that the fwhm calculated for the diluted HOD in H_2O, diluted H_2O in D_2O, and neat H_2O solutions increase by 21 cm^{-1}, 28 cm^{-1}, and 43 cm^{-1}, respectively, going from the 1B to the 1B+2B+NB representation of the dipole moment, while the fwhm calculated for the diluted HOD in D_2O decreases by 15 cm^{-1}. Since the 1B lineshape depends only on the gas-phase dipole moment of the HOD molecule, the narrowing of the linewidth with the increase of electrostatic coupling demonstrates that, when integrated in the H-bond network, the dipole moment of a fully decoupled OH oscillator samples a narrower distribution of values than in the gas phase. Table 2.1 shows that, depending on the isotopic solution, the changes in linewidths are accompanied by red shifts in the frequencies of maximum absorbance in the range of 30 to 117 cm^{-1} going from the 1B to the 1B+2B+NB representation of the dipole moment.

These changes are particularly pronounced in the lineshape of diluted HOD in H_2O. While this isotopic mixture cannot be probed in experiments, the theoretical predictions shown in Fig. 2.3b can be used to characterize the nature of intermolecular coupling, isolated from any other competing effects. Since, as discussed in detail in Ref. 119, the 2B term of the MB-μ function recovers electrostatic contributions associated with quantum-mechanical effects (e.g., charge transfer and penetration, and Pauli repulsion) that cannot be described by classical expressions, the large difference in IR intensity between 1B+NB and 1B+2B+NB lineshapes of diluted HOD in H_2O provides direct evidence for the partially quantum-mechanical nature of H-bonds in liquid water. The 1B+2B+NB lineshape for the diluted H_2O in D_2O solution also exhibits higher intensity than its 1B+NB analog in the low-frequency region, although the differences are not as

large as those observed for the diluted HOD in H_2O solution. While these results provide further support for the partially quantum-mechanical nature of H-bonds in liquid water, the differences between the lineshapes for diluted H_2O in D_2O and diluted HOD in H_2O solutions clearly indicate that 2B quantum-mechanical effects in H-bonding are enhanced by intermolecular coupling.

The analysis of the IR lineshapes for the diluted H_2O in D_2O solution (Fig. 2.3c), which cannot be probed experimentally, provides the unique opportunity to isolate the contributions due to intramolecular coupling. As mentioned above, compared to the lineshapes for both fully decoupled HOD in D_2O and intermolecularly coupled HOD in H_2O solutions, the lineshape for the intramolecularly coupled H_2O in D_2O solution grows in intensity below 3250 cm^{-1}. To determine the origin of this intensity enhancement, we performed LM calculations.[57,122,123] Since, by construction, the LM method provides a rigorous theoretical framework for identifying both fundamental and overtone transitions, it allows for the dissection of the OH lineshape in terms of actual OH stretching vibrations and HOH bending overtones, which may give rise to Fermi resonances.[116,118,130] However, due to the associated computational cost, LM calculations are only carried out on clusters consisting of a H_2O molecule solvated by 16 D_2O molecules, which are extracted from the CMD trajectories for the diluted H_2O in D_2O solution. The LM results, decomposed in contributions associated with HOH bending overtones (dark green) and OH stretching vibrations (light green) are shown along with the corresponding 1B+2B+NB (light blue) lineshape in Fig. 2.4a. Also shown for reference are both experimental (black) and CMD (blue) lineshapes for neat H_2O. The comparison between LM and CMD results indicates that the relative increase in intensity observed below 3250 cm^{-1} in the 1B+2B+NB lineshape for the diluted H_2O in D_2O solution can be attributed to Fermi resonances arising from quantum-mechanical mixing between HOH bending overtones and OH stretching fundamentals as recently suggested.[71,72,118,120,130]

This analysis also sheds light on the missing intensity in the low-frequency region of the CMD IR lineshape for the neat H_2O solution compared to experiment. As mentioned above and

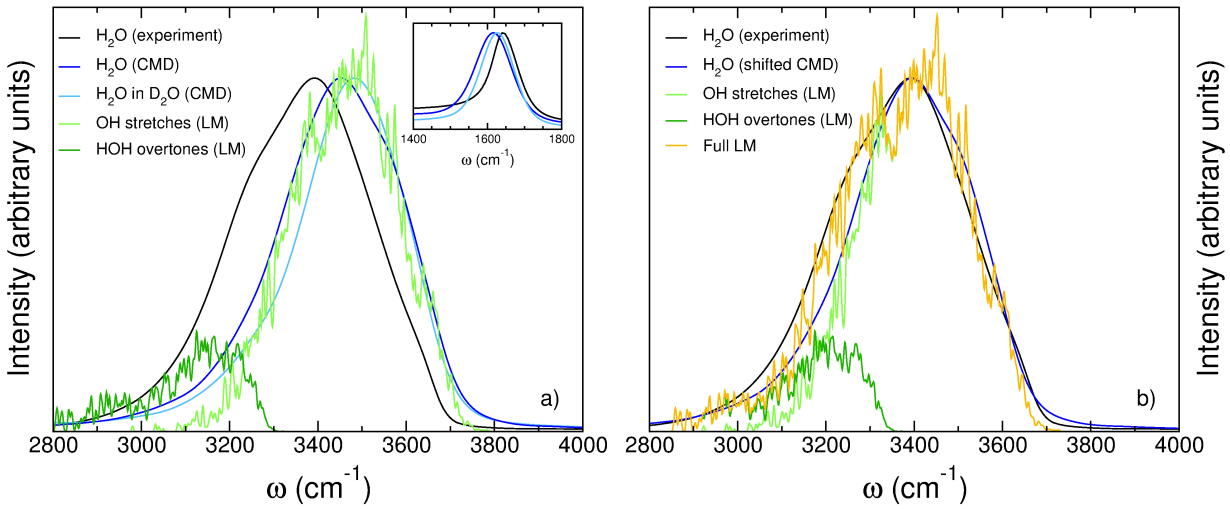

Figure 2.4: a) LM frequency distributions of OH stretches (light green) and HOH-bend overtones (dark green) calculated for diluted H_2O in D_2O, experimental (black) and CMD (blue) IR OH-stretch lineshapes of neat H_2O, and CMD (light blue) IR OH-stretch lineshape of diluted H_2O in D_2O. b) LM frequency distributions of OH stretches (light green) and HOH-bend overtones (dark green) calculated for diluted H_2O in D_2O and shifted by -57 cm^{-1} and 50 cm^{-1}, respectively, full LM lineshape (yellow), experimental (black) and CMD (blue) IR OH-stretch lineshapes of neat H_2O, with the latter being shifted by -57 cm^{-1}. See main text for details.

discussed in detail in Refs. 71 and 72, MB-pol slightly underestimates the strength of H-bonds in liquid water, which translates into a 57 cm^{-1} blue shift of the calculated OH stretch lineshape relative to experiment. At the same time, weaker H-bonds also lead to a $\sim$25 cm^{-1} red shift of the calculated HOH bend lineshape (see inset in Fig. 2.4a). After correcting for these inaccuracies by shifting the LM OH-stretch and HOH-bend-overtone frequency distributions by -57 cm^{-1} and 50 cm^{-1} (twice the difference from the bending region), respectively, Figure 2.4b shows that the lineshape obtained by adding the two LM components is in excellent agreement with the experimental lineshape, recovering, almost completely, the missing intensity below $\sim$3300 cm^{-1}. The results reported in Fig. 2.4b thus demonstrate that the differences between the CMD and experimental OH-stretch lineshapes can be traced back to MB-pol slightly underestimating the strength of H-bonds in liquid water which, in turn, results in the underestimation of Fermi resonance contributions due to the predicted weaker coupling between OH stretches and HOH bend overtones. In this regard, it should be noted that a deviation of 57 cm^{-1}, corresponding to

0.16 kcal/mol, is well within what is currently defined chemical accuracy (1 kcal/mol), which is achieved by MB-pol. This implies that, as originally suggested in Ref. 71, a quantitative representation of the IR OH-stretch lineshape might effectively require "exact" knowledge of the multidimensional Born-Oppenheimer potential energy surface of liquid water, including an accurate description of autoionization, which is currently beyond reach of even the most sophisticated electronic structure methods.

2.4 Conclusions

In this study, we have combined accurate modeling of water through the use of the MB-pol potential energy function with CMD simulations that account for nuclear quantum effects. Building upon our previous studies,[71,72] we have investigated four isotopic solutions with different levels of vibrational coupling, including neat H_2O, diluted HOD in H_2O, diluted H_2O in D_2O, and diluted HOD in D_2O solutions. Our analysis, carried out with different approximations to many-body effects in the representation of the water dipole moment, indicates that the IR OH-stretch lineshapes of all four isotopic solutions increase in intensity and shift toward lower frequencies as electrostatic couplings are taken into account. In this regard, the narrowing of the lineshape for the diluted HOD in D_2O solution going from the 1B to the 1B+2B+NB representation of the dipole moment demonstrates that the dipole moment of a fully decoupled OH oscillator immersed in the D_2O H-bond network samples a narrower distribution than in the gas phase.

Comparisons between the IR OH-stretch lineshapes for the diluted HOD in H_2O and diluted H_2O in D_2O solutions, which cannot be probed experimentally due to isotope exchange, have allowed us to further disentangle the IR OH-stretch lineshape of neat H_2O into effects associated with intermolecular and intramolecular couplings. In particular, the analysis of the IR lineshape of the intermolecularly coupled OH stretch of HOD in H_2O provides direct evidence

for the partially quantum-mechanical nature of H-bonds in liquid water, with intermolecular coupling becoming larger for stronger H-bonds. On the other hand, the IR lineshape of the intramolecularly coupled OH stretch of H_2O in D_2O shows the presence of significant overlap between the frequencies of the IR OH-stretch fundamentals and HOH-bend overtones. Additional LM calculations carried out for the OH stretches of H_2O in D_2O have allowed us to quantify the role played by Fermi resonances in modulating the IR OH-stretch lineshape. In particular, by taking into account that MB-pol slightly underestimates the H-bond strength in liquid water, the present results quantitatively demonstrate that Fermi resonances are responsible for the shoulder at $\sim$3250 cm^{-1} of the IR OH-stretch lineshape of neat H_2O.

2.5 Supporting Information

Additional comparisons of the IR OH-stretch lineshapes along with the analogous IR OD-stretch lineshapes are presented. It is shown that similar conclusions about the role of intramolecular and intermolecular couplings can be drawn from the analysis of the IR OD-stretch lineshapes.

2.6 Acknowledgments

This research was supported by the National Science Foundation through grant no. CHE-1453204 and used resources of the Extreme Science and Engineering Discovery Environment (XSEDE),[132] which is supported by the National Science Foundation through grant no. ACI-1053575, under allocation TG-CHE110009 as well as computational resources of the Air Force Office of Scientific Research through grant no. FA9550-16-1-0327.

Chapter 2, in full, is a reprint of the material as it appears in "Disentangling Coupling Effects in the Infrared Spectra of Liquid Water", Hunter, K.M.; Shakib, F.A.; Paesani, F.; J. Phys.

Chem. B, 122, 10754-10761, 2018. The dissertation author was the primary investigator and author of this paper.

Chapter 3

Hydrogen Bonding Structure of Confined Water Templated by a Metal-Organic Framework with Open Metal Sites

Due to the formation of frustrated hydrogen-bond (H-bond) networks, water confined within pores or at interfaces exhibits significantly altered physical properties compared to bulk water, with important implications for different fields, including chemistry,[133,134] biology,[135–137] and atmospheric science.[138,139] As a consequence of the unique structural and dynamical properties of frustrated H-bond networks, confinement of water gives rise to anomalous behavior, as inferred from measurements of various quantities, such as the dielectric constant[140] and diffusion coefficient.[141] Significant progress has recently been made in developing a more complete picture of the water H-bonding structure,[142] especially due to the introduction of accurate many-body molecular models.[143] Nevertheless, a precise prediction of the properties of water across different phases and in different environments remains a challenge due to the dynamic nature of the H-bond network which results from the subtle balance between energetic, entropic, and nuclear quantum effects.[143–145]

As confinement increases, so too does the importance of interactions between the water molecules and the confining environment, with distinct consequences for the H-bonding structure.[146,147] Studies aiming to characterize the thermodynamic and dynamic properties of water in confinement have targeted various porous materials, such as hydrophobic carbon nanotubes[148–152] and hydrophilic zeolites and silicas, as water containers.[153] It was found that water inside carbon nanotubes forms one-dimensional and tightly H-bonded chains, while ordered phases were identified in water confined in zeolites. On the other hand, water adsorbed on metal surfaces often displays well-defined patterns that are templated by the strength and anisotropy of the underlying water–metal interactions.[154] However, the uniformity of the hydrophobicity or hydrophilicity associated with these materials engenders mostly predictable water–substrate interactions that may differ significantly from those observed in heterogeneous environments, such as aquaporins and other structures found in biological systems,[135] where both hydrophilic and hydrophobic patches coexist and lead to a variety of competing H-bonding domains.[133–139]

Metal–organic frameworks (MOFs) have recently received attention as water containers exhibiting tunable hydrophilicity of potential use in adsorption heat pumps[15,38,155–158] and for atmospheric water harvesting.[41,159] In this regard, we posit that a MOF termed Co_2Cl_2BTDD (H_2BTDD=bis(1*H*-1,2,3-triazolo[4,5-b],[4',5'-i]) dibenzo[1,4]dioxin)), which was recently investigated for its record reversible water uptake (Fig. 3.1), will provide a relevant crystalline analog for investigating the H-bonding structure of water in heterogeneous confinement.[41] Here we combine diffuse reflectance infrared Fourier transform spectroscopy (DRIFTS) measurements with many-body molecular dynamics (MB-MD) simulations.[60–63,71] Our analysis implicates the initial formation of distinct one-dimensional (1-D) chains of adsorbed water molecules bridging between the framework hydrophilic open metal sites as the critical step for pore filling in Co_2Cl_2BTDD. As the relative humidity (RH) increases, these 1-D chains template the subsequent formation of cylindrical water shells that extend along the hydrophobic pore channels and exhibit progressively faster rotational and translational mobility as a function of the distance from the

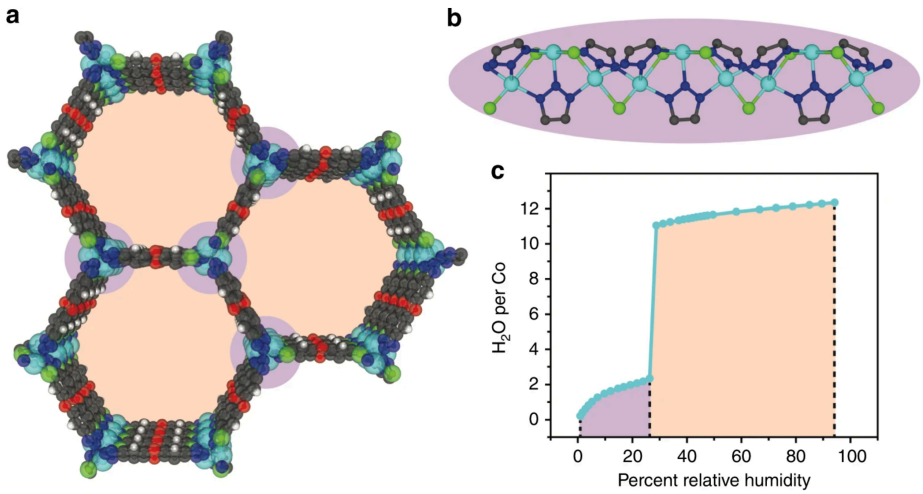

Figure 3.1: Structure and Water Adsorption of Co_2Cl_2BTDD. **a** Structure of Co_2Cl_2BTDD viewed down the z-axis. C – gray, H – white, O – red, N – dark blue, Cl – green, Co – light blue. Hydrophilic regions are indicated in purple and hydrophobic regions in orange. **b** Structure of the secondary building unit along the z-axis. **c** Water adsorption isotherm at 20 °C for Co_2Cl_2BTDD exhibiting complete pore hydration at 28% RH, data adapted from ref. 41

pore surface.

3.1 Results

3.1.1 Infrared measurements of the water adsorption process

Co_2Cl_2BTDD was synthesized as previously reported,[160] with a consistent powder X-ray diffraction pattern and N_2 adsorption isotherm (Supplementary Figs. 6, 7). The structure exhibits hexagonal pores 2.2 nm in diameter linked by secondary building units consisting of infinite chains of cobalt chloride bridged by triazolate groups, wherein each nitrogen atom is ligated to a distinct Co^{2+} (Fig. 3.1a, b). DRIFTS spectra were measured at 20 °C under variable RH (Fig. 3.2b and Supplementary Fig. 8). With increasing RH, notable changes in the infrared spectrum appear around 600 cm^{-1} for the water librational mode, at 1600 cm^{-1} for the HOH bending mode, and near 3500 cm^{-1} for the water OH-stretching band (Supplementary Fig. 8).[161,162] At low RH, the

OH-stretching region displays several well-defined peaks, indicating that the water molecules experience distinct environments within the pore, which are non-equivalent on the IR timescale (Fig. 3.2a). The highest frequency peak at 3700 cm^{-1} can be attributed to the presence of free OH bonds, i.e., OH bonds that are not engaged in H-bonding.[163] Although free OH bonds are short-lived in bulk water,[164] they are present at the air/water interface,[165,166] which thus seems to provide a closer reference for water adsorbed at low RH in the Co_2Cl_2BTDD pores. The remaining series of peaks suggests a complicated interplay between water–framework and water–water interactions that lead to a broad range of H-bond strengths.

As the RH increases, the individual peaks coalesce into a single broad band resembling that of bulk water.

3.1.2 Simulating water in confinement using the MB-pol model

A molecular-level interpretation of the origin and evolution of the different spectral features as a function of RH is obtained from classical MB-MD simulations carried out combining the MB-pol water model,[60–63,71] which has been shown to accurately predict the properties of water from the gas to the condensed phase,[167] with a flexible force field for Co_2Cl_2BTDD (see the Supplementary Methods, Supplementary Figs. 1-5, and Supplementary Tables 1-4 for details). All simulations were carried out at a temperature of 300 K (Supplementary Figs. 14, 15). To allow for direct comparison with the experimental data, all theoretical infrared (IR) spectra, which are calculated from the dipole-dipole time correlation function (see the Supplementary Methods for details), are red-shifted by 175 cm^{-1} in the OH-stretching region to account for zero-point energy effects that are neglected in classical MB-MD simulations, as discussed in detail in Refs. 71, 75. Accounting for zero-point energy effects, good agreement is obtained with the experimental data (Fig. 3.2b and Supplementary Fig. 8), with the theoretical spectra reproducing the same distinct series of peaks at low RH and the emergence of a progressively broader band as the RH increases.

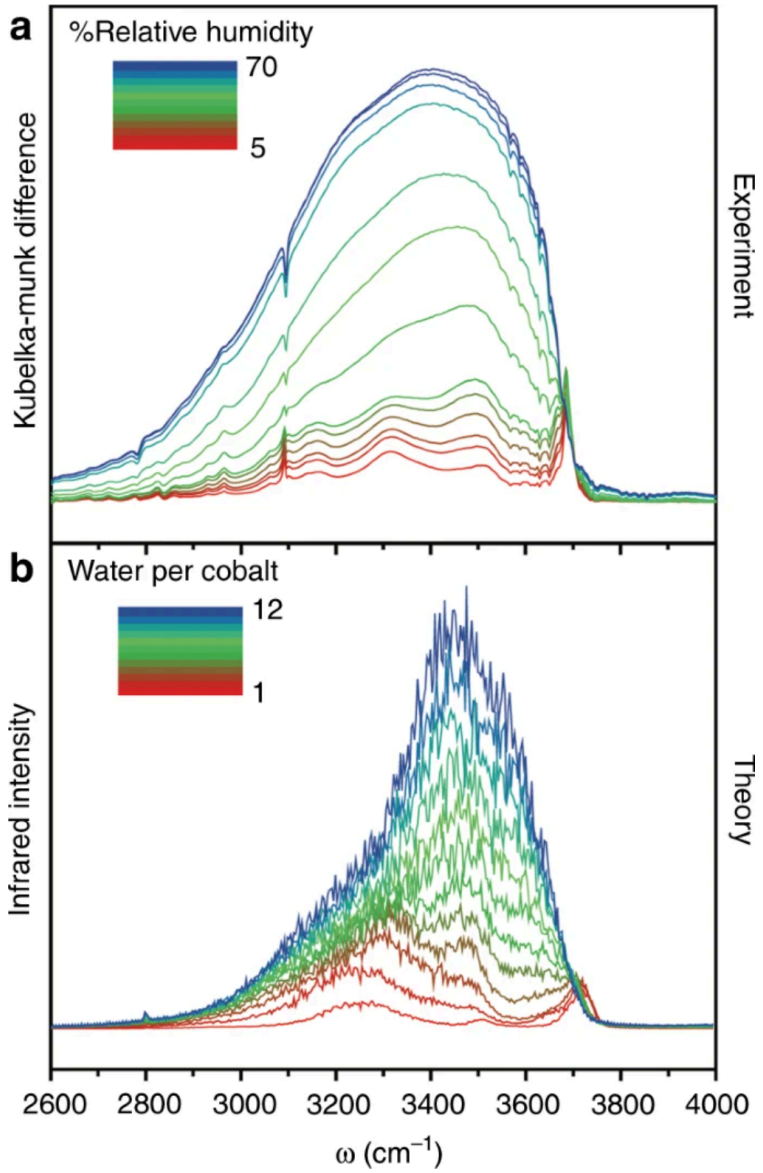

Figure 3.2: Experimental and Theoretical Infrared Spectra of Water in Co_2Cl_2BTDD. **a** Difference Diffuse-Reflectance IR spectra of the water OH-stretch region in Co_2Cl_2BTDD under variable RH conditions. **b** Calculated IR intensity using the MB-pol model of water in Co_2Cl_2BTDD ranging from one water molecule per cobalt (1) to twelve water molecules per cobalt (12)

3.2 Discussion

To characterize the evolution of the H-bond network during pore filling, the results of separate MB-MD simulations carried out with only one and two water molecules in the simulation box are examined in Fig. 3.3a. The most favorable location of a single water molecule in the

Co_2Cl_2BTDD pores corresponds to coordination with one of the open cobalt sites. In this configuration, the two OH bonds of the water molecule are not equivalent on a picosecond timescale due to different interactions with the framework. This results in two peaks at 3550 cm^{-1} and 3700 cm^{-1} (orange trace in Fig. 3.3b) that, while reminiscent of the symmetric and asymmetric stretches, correspond to two distinct OH-stretch vibrations (see Supplementary Fig. 9 for specific details, and Supplementary Tables 6–17 and Supplementary Figs. 14, 15 for details concerning simulation temperature at various water loadings). The peak at lower frequency is associated with the stretching vibration of the OH bond weakly interacting with a triazolate group of the framework while the peak at higher frequency is associated with the OH bond weakly interacting with the nearest chloride atom of the framework.

The addition of a second water molecule leads to the formation of a H-bonded dimer, with the first molecule remaining coordinated with the open cobalt site. MB-MD simulations indicate that the two OH bonds on the second water are relatively free to rotate (on a timescale of 0.50 ps) due to lack of specific interactions with the framework. The decomposition of the theoretical IR spectrum in terms of individual OH-stretch contributions (pink trace in Fig. 3.3b) reveals that the second water molecule is primarily responsible for the peaks at 3550 cm^{-1} and 3700 cm^{-1}. The cobalt-bound water is instead responsible for the emergence of the two new peaks at 3300 cm^{-1} and 3650 cm^{-1}, with the first peak corresponding to the H-bonded OH-stretch and the second peak being associated with the non-H-bonded OH bond. Being relatively free to rotate, the non-H-bonded OH bond experiences a wide range of local environments and is thus found to also contribute to the peaks at 3550 cm^{-1} and 3700 cm^{-1} (see Supplementary Fig. 9 for specific details).

A nearly one-to-one correspondence is found in Fig. 3.3b between the theoretical IR spectra calculated for one and two water molecules and the experimental DRIFTS spectra measured at low RH. Based on the equilibrium water isotherm data (Fig. 3.1c), the experimental water uptake at 2, 4, and 6% RH corresponds to approximately 0.5, 0.9, and 1.2 water molecules

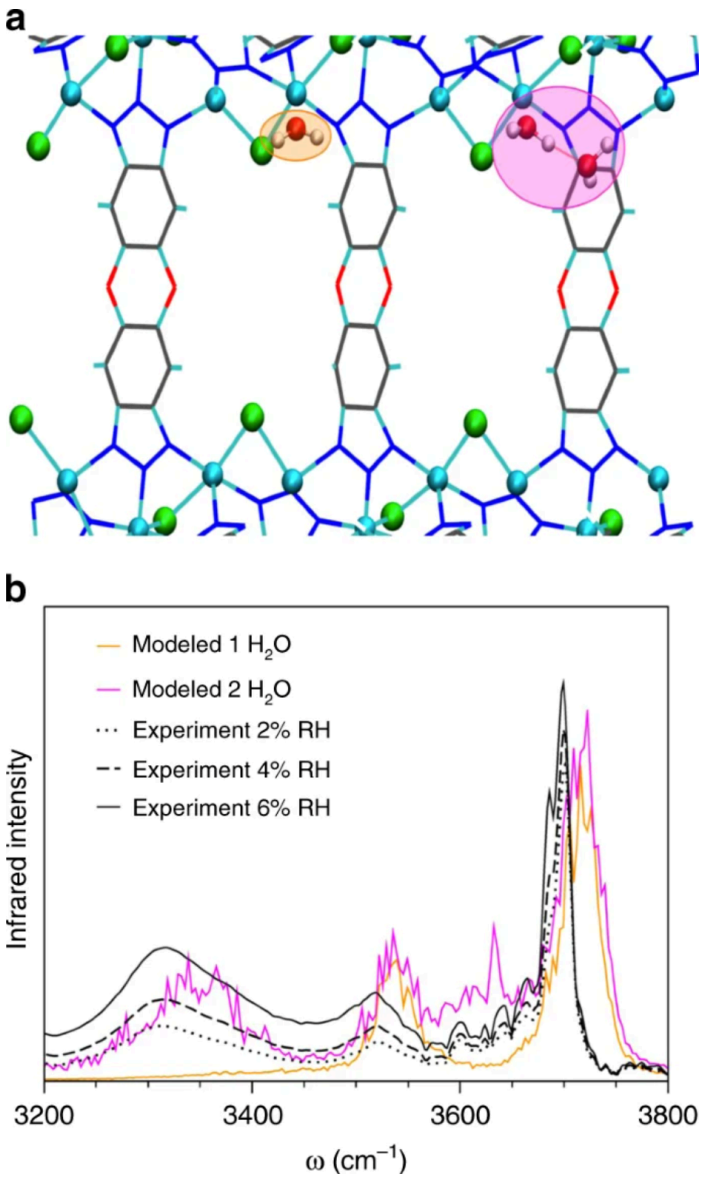

Figure 3.3: Water at Low Loadings in Co_2Cl_2BTDD. **a** Simulations with one (orange) and two (pink) water molecules. Distance shown along the z-axis is 24 Å. **b** Calculated IR OH-stretches of one (orange) and two (pink) water molecules with corresponding experimental DRIFTS spectra at RH 2% (dotted black), 4% (dashed black), and 6% (solid black)

per cobalt atom, respectively. Although water molecules interact more strongly with the open Co^{2+} sites, the presence of the spectral feature at 3300 cm^{-1} , indicative of the water dimer at the cobalt site, thus implies that water begins forming localized H-bonded clusters seeded by cobalt-bound water molecules prior to full saturation of the open Co^{2+} sites.

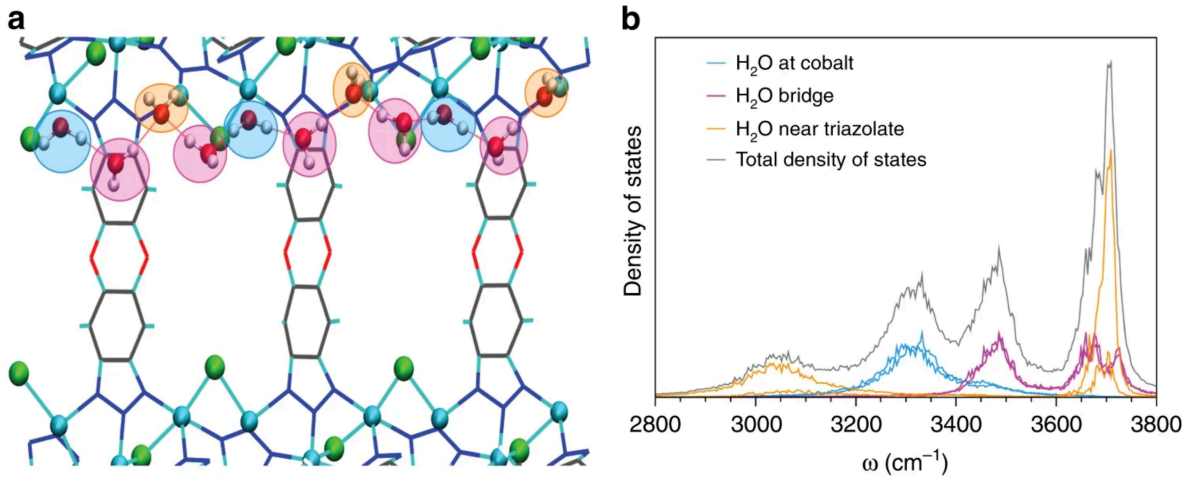

Figure 3.4: Chains of Water Bridge Between Cobalt Sites. **a** Structure of the one-dimensional water chain with water at cobalt (blue), water bridges (pink), and water near the triazolate (orange) highlighted. Distance shown along the z-axis is 24 Å. **b** Density of states calculated for individual hydrogen atoms

Simulating the adsorption of additional water molecules reveals the formation of 1-D water chains bridging between cobalt sites. These chains consist of three types of water molecules residing in three distinct local environments. Water molecules of the first type correspond to those bound to the open Co^{2+} sites (light blue in Fig. 3.4a), which engage in two H-bonds, one each to two adjacent water molecules of the second type. These second-type water molecules (pink in Fig. 3.4a) act as bridging molecules (similar to the second water molecule in Fig. 3.3a) by accepting and donating one H-bond and do not interact directly with the framework. Water molecules of the third type (orange in Fig. 3.4a) correspond to those that interact with the framework by pointing one OH bond to the π-system of the neighboring triazolate group, while accepting two H-bonds, one each from two adjacent bridging water molecules.

Further insights into the nature of the interactions between the framework and the water molecules residing in the three different local environments are gained by dissecting the density of states (DOS), corresponding to the theoretical spectra, into individual contributions associated with each type of water molecule along the 1-D chains. It is found that the cobalt-bound water molecules only contribute to the peak at 3300 cm^{-1} (light blue trace in Fig. 3.4b), which is a

spectral feature characteristic of double donor H-bonded water molecules. Since these molecules are pinned to the open Co^{2+} sites and engage in two H-bonds, which are equivalent on the IR timescale, their mobility is highly frustrated (Supplementary Fig. 10). The water-bridging molecules contribute to the two peaks at 3500 and 3700 cm^{-1} (pink trace in Fig. 3.4b), which are associated with the stretching vibrations of the H-bonded and free OH bonds, respectively. Due to the absence of directional interactions with the framework, these molecules can easily switch H-bond partners and display significantly faster orientational mobility than the cobalt-bound molecules (Supplementary Fig. 10). Finally, the water-to-triazolate molecules contribute to the two bands at 3050 and 3700 cm^{-1} (orange trace in Fig. 3.4b), with the lower frequency peak being associated with the stretching vibrations of the OH bonds pointing toward the π-systems of the triazolate groups and the higher frequency peak corresponding to the stretching vibrations of the other (free) OH bonds, respectively. Due to relatively stronger interactions with the triazolate groups, these water molecules exhibit rotational mobility that is intermediate between those displayed by cobalt-bound and bridging water molecules (Supplementary Fig. 10). The combination of the theoretical DOSs calculated for the three types of water molecules along the 1-D chains results in a vibrational lineshape (gray trace in Fig. 3.4b) that reproduces the main peaks of the experimental DRIFTS spectra measured below 30% RH, before the MOF pores become fully hydrated (Fig. 3.2a and Supplementary Table 5). Although connecting every open Co^{2+} site with water chains would require four water molecules per cobalt, the isotherm data indicate that pore hydration is initiated at 2.3 water molecules per cobalt (Fig. 3.1c). This suggests that disconnected 1-D chains form in various locations within the framework before all cobalt sites are saturated, which is supported by our MB-MD simulations showing that 1-D chains bridging multiple cobalt sites begin to appear at a loading of two water molecules per cobalt.

At higher water loadings, the 1-D water chains bridging the hydrophilic open Co^{2+} sites act as nucleators for the pore filling process, templating the formation of concentric cylindrical shells that extend along the hydrophobic pore channels. As the water loading increases, the MB-

MD simulations indicate that the water molecules become, on average, more mobile (Fig. 3.5a). Because the orientational correlation functions reflect the extent of molecular rotation over time, this suggests the emergence of liquid-like behavior. However, at the experimental maximum loading of 12 H_2O/Co^{2+}, the average orientational mobility of the water molecules in the Co_2Cl_2BTDD pores remains intermediate between that calculated for ice and bulk water. A similar slowdown was predicted for water adsorbed in MIL-53.[168]

The evolution of the dynamical behavior of water adsorbed in Co_2Cl_2BTDD as a function of RH can be further characterized by analyzing the variation of the water mobility from the surface to the center of the pore. To this purpose, the water molecules along the MB-MD trajectories are classified based on their distances from the surface of the pore and thus assigned to three concentric cylindrical sectors (shown in dark yellow, orange, and red in Fig. 3.5b, e), with a width of 4.0 Åeach.

As discussed above, at low RH corresponding to a loading of 1 H_2O/Co^{2+}, the water molecules are primarily coordinated to the open cobalt sites, although there is not a one-to-one correspondence, and Co^{2+}-pinned water dimers and trimers also form within the pores as inferred by the DRIFTS lineshapes. These water molecules thus reside in sector 1, providing an outer shell of H-bonding sites that effectively template the development of the H-bonding structure inside the pores at high RH (Fig. 3.5b, c). Water molecules enter sector 2 at a loading of 2 H_2O/Co^{2+} and start filling sector 3 at a loading of 7 H_2O/Co^{2+} (Fig. 3.5d and Supplementary Figs. 11, 12). At the loading of 11 H_2O/Co^{2+}, the water molecules fill the pore completely although they tend to cluster around the open cobalt sites as shown in Fig. 3.5e, f. Similar templating effects of the framework on adsorbed water were predicted from computer simulations of water in [Zn(L)(X)] (L = 3-methyl-2-(pyridin-4-ylmethylamino)-butanoic acid and X = Cl and Br),[169] and MOF-74.[88] Analysis of both orientational and translational mobility shows that water molecules occupying different sectors exhibit significantly different dynamical behavior (Table 3.1 and Supplementary Figs. 11, 12). While water molecules in sector 1 reorient very slowly and are

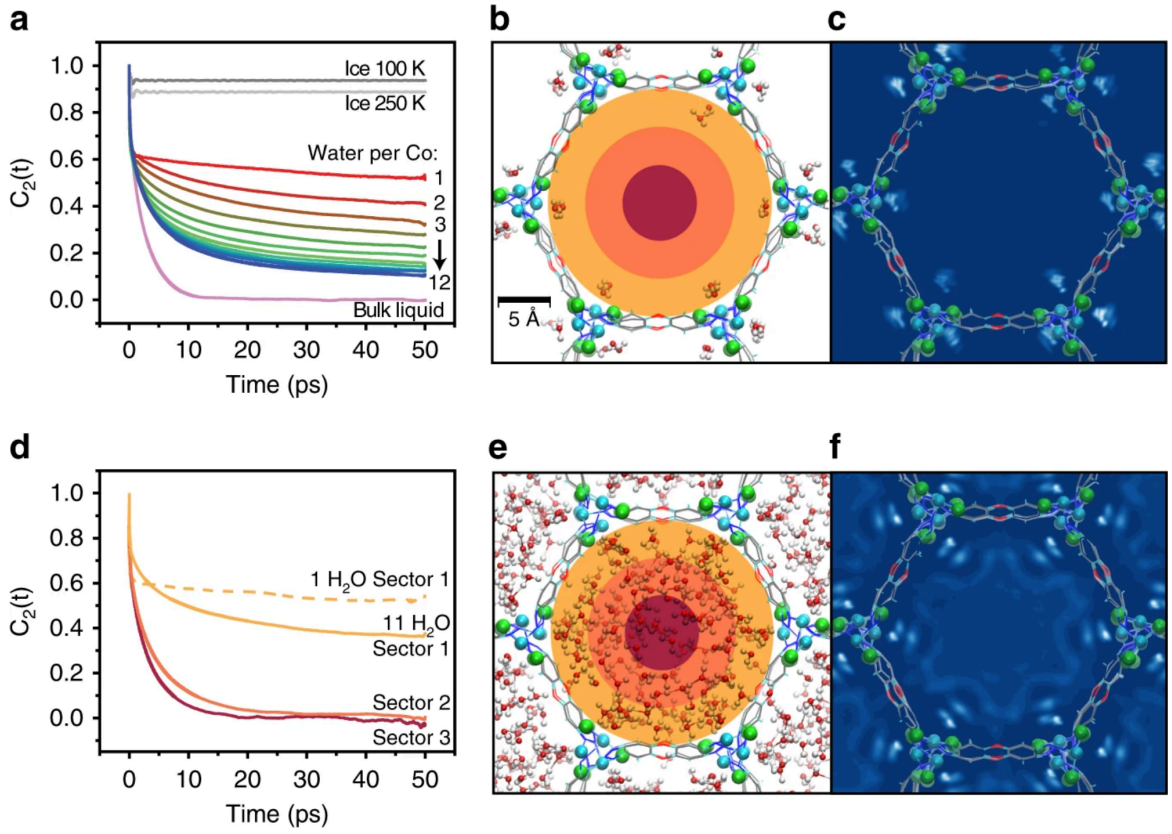

Figure 3.5: Dynamics of Water in Co_2Cl_2BTDD. **a** Orientational correlation functions calculated from MB-MD simulations carried out for various loadings of water inside the Co_2Cl_2BTDD pores. Also shown for reference are the corresponding orientational correlation functions calculated from MB-MD simulations of liquid water (pink) and ice (gray). **b** Snapshot from an MB-MD simulation of water in Co_2Cl_2BTDD for a loading of 1 H_2O/Co^{2+}. The three concentric colored sectors are defined according to their distance from the pore surface: Sector 1 from 0–4 Å(dark yellow), Sector 2 from 4–8 Å(orange), and Sector 3 from 8–12 Å(red). **c** Two-dimensional (2-D) density map of water calculated from MB-MD simulations carried out for a loading of 1 H_2O/Co^{2+} (lighter colors correspond to regions with higher water density). **d** Orientational correlation functions calculated for water in the three different sectors of the pore at either 1 H_2O/Co^{2+} (dashed line) or 11 H_2O/Co^{2+} (solid lines). **e** Snapshot of an MB-MD simulation of water in Co_2Cl_2BTDD for a loading of 11 H_2O/Co^{2+} (the three concentric colored sectors are defined as in b. **f** 2-D density map for a loading of 11 H_2O/Co^{2+} (lighter colors correspond to regions with higher water density)

effectively translationally immobile, being directly coordinated with the Co^{2+} atoms or H-bonded to the Co-bound molecules, water molecules in sectors 2 and 3 display progressively faster dynamics. In particular, water molecules at the center of the pore (sector 3) reorient on a timescale

of 4.4 ps and diffuse along the pore (z direction) by 0.24 $Å^2$ ps^{-1}, which suggests dynamical behavior similar to liquid water (Table 3.1). The overall difference in the orientational relaxation times and diffusion coefficients of Table 3.1 displays the dynamical heterogeneity that exists between the different sectors due to their distance from the pore surface. Additionally, it should be noted that, due to confinement, water mobility along the x and y directions is systematically lower than along the z direction.

Table 3.1: Dynamics of water in Co_2Cl_2BTDD orientational relaxation time (τ_2), calculated from $C_2(t) = Ae^{-t/\tau_2}$, along with the total diffusion coefficient (D_{tot}), diffusion coefficient along the xy-plane (D_{xy}), and diffusion coefficient along the z direction (D_z) for 11 H_2O/Co^{2+} with standard deviations. Experimental data for τ_2 and D_{tot} in bulk water are taken from refs. 170, 171, respectively. See the Supplementary Methods for specific details about the calculation of orientational relaxation time and diffusion coefficients.

	τ_2 (ps)	D_{tot} ($Å^2 \cdot ps^{-1}$)	D_{xy} ($Å^2 \cdot ps^{-1}$)	D_z ($Å^2 \cdot ps^{-1}$)
Sector 1	>70	0.03 ± 0.01	0.02 ± 0.01	0.04 ± 0.01
Sector 2	8.3 ± 1.8	0.11 ± 0.03	0.09 ± 0.03	0.15 ± 0.04
Sector 3	4.4 ± 0.9	0.19 ± 0.05	0.16 ± 0.05	0.24 ± 0.08
Exp. Bulk water	2.5	0.23		
No standard deviations were calculated for the orientational relaxation time in Sector 1 since it was only possible to determine that the relaxation time is longer than 70 ps				

In addition to the dynamical heterogeneity exhibited by water molecules in different pore environments, structural parameters reveal increasingly frustrated H-bond networks closer to the pore surface. At the maximum loading of 12 H_2O/Co^{2+}, Supplementary Fig. 13 shows that the distribution of the tetrahedral order parameter, q_{tet}, a metric of the local structure of the water H-bond network, displays two distinct features – a dominant one with a maximum at $q_{tet} \approx 0.4$, indicating less tetrahedrality and suggesting environments with interfacial character, and a second feature with a maximum at $q_{tet} \approx 0.8$, representative of liquid-like environments.[172] The structural and dynamical heterogeneity exhibited by water at the maximum loading thus mirrors the water adsorption process observed by DRIFTS, as the sites with the highest water density, the least tetrahedral H-bonding network, and the slowest mobility in the full pore correspond with the sites of initial water adsorption near the metal sites.

Water confined in Co_2Cl_2BTDD pores exhibits similarities and differences with water adsorbed on surfaces. For example, water at metal surfaces tends to display long-range order.[173] Although at low RH, water inside Co_2Cl_2BTDD displays a similar order due to coordination to the open cobalt sites, higher RH disrupts the long-range order, and water molecules display progressively liquid-like behavior as they approach the center of the MOF pores. This is reflected in the broadening of the OH-stretch vibrational lineshapes towards lower frequencies characteristic of H-bond networks.

In summary, water adsorbed in Co_2Cl_2BTDD displays heterogeneous structural and dynamical behavior which varies as a function of both RH and distance from the pore surface. By directly connecting adsorption isotherms with the evolution of IR spectra of water inside MOF pores as a function of RH, the foregoing combined experimental and theoretical approach provides detailed insights into the molecular mechanisms that determine water adsorption in porous materials exhibiting both hydrophilic and hydrophobic regions. These mechanistic insights can contribute to the design of next-generation porous materials for water harvesting. Fundamentally, our approach advances the understanding of water structure and dynamics within amphipathic confined and interfacial environments which are widespread in biology, atmospheric science, and chemistry.

3.3 Methods

3.3.1 Synthesis

Co_2Cl_2BTDD was synthesized and activated according to a previously published procedure.[160] Briefly, 200 mg H_2BTDD[135] (0.75 mmol) was dissolved in 200 mL N,N'- dimethylformamide (DMF) with heating, then cooled to room temperature. Separately, 1.5 mmol (2 eq.) cobalt chloride hydrate was dissolved in 200 mL ethanol and 4 mL concentrated hydrochloric acid. The clear solutions were combined, capped, and heated to 65 °C in an oven for 10 days.

The resulting solids were filtered, washed with DMF and methanol. Solvent exchange of DMF was carried out by Soxhlet extraction with methanol for approximately 48 h. The materials were then activated under dynamic vacuum at 150 °C for 24 h.

3.3.2 Spectroscopic measurements

Diffuse reflectance infrared Fourier transform spectroscopy (DRIFTS) measurements were performed using a Bruker Tensor 37 IR spectrometer equipped with a liquid nitrogen cooled mercury cadmium telluride detector and a Pike DiffusIR accessory. A sample of Co_2Cl_2BTDD, pre-activated at 150 °C under vacuum to remove all solvents, was diluted with KBr in a ratio of approximately 1:5 (MOF:KBr) in an argon-filled glovebox. The resulting solid solution was then packed into a ceramic cup and sealed in the DiffusIR cell. The cell was brought out of the box, and a static dry spectrum was recorded with the cell sealed. Two gas streams of flowing argon (UHP grade 5.0, Airgas), one wet (bubbled through a fine frit through MilliQ H_2O) and one dry, were each flow controlled using mass flow controllers (MFCs), and joined together at a T fitting before connecting to the DRIFTS cell. The wet stream and dry stream were controlled via the MFCs to change relative humidity (RH) every 20 min (a time period previously demonstrated to result in saturation of the IR spectrum at all loadings). The MFCs were controlled such that the total flow rate was constant at 1 liter per minute (LPM) (e.g. for 40% RH, 0.4 LPM wet, 0.6 LPM dry). The temperature for all measurements was 20 °C. Spectra were recorded at the end of the period at which the sample atmosphere was at each RH, every 20 min. Data was transformed using the Kubelka-Munk function.[174] The static dry spectrum was subtracted from the humid measurements in all cases.

3.3.3 Molecular dynamics simulations

All simulations utilized the many-body potential energy function (MB-pol) to describe water, which is built upon a many-body expansion of the interaction energy for water.[60–62] MB-pol has been previously shown to accurately reproduce the properties of water from the gas to the condensed phase.[63] The framework atoms of Co_2Cl_2BTDD were modeled with a flexible force field consisting of point charges (details in the Supplementary Methods). In simulating Co_2Cl_2BTDD, the first configuration utilizes one water molecule per cobalt atom (1, corresponding to 54 water molecules), and in each subsequent simulation at each loading, an additional water molecule is added per cobalt atom (2, 3, etc.). The initial configurations for each loading were generated using Packmol,[175] adding the specific number of water molecules to 756 MOF atoms. Classical many-body molecular dynamics (MB-MD) simulations were performed using in-house software based on the DL_POLY_2 simulation package,[176] which was modified to include the MB-pol potential energy function.[60–62] All simulations were carried out for a system consisting of $1 \times 1 \times 3$ primitive cells under periodic boundary conditions with cell dimensions 38.6590 Å, 33.4793 Å, and 25.6914 Å and angles 90°, 90°, and 120° along the x, y, and z dimensions, respectively. Each system was equilibrated through a constant volume and constant temperature (NVT) canonical ensemble at 300 K for 10 ps, and dynamical information was obtained through a constant volume and constant energy (NVE) microcanonical ensemble for 50 ps where the temperature remained stable around 300 K. Constant pressure and constant temperature (NPT) simulations at 1.0 atm and 300 K were also performed to investigate the flexibility of the framework throughout the simulation. During the NPT simulations, all three cell dimensions vary by 4.5% with average values of 36.6955 Å, 31.7789 Å, and 24.3865 Å along the x, y, and z dimensions, respectively. While the cell size varies slightly, the framework remains constant in size throughout the simulations. Twenty independent MB-MD trajectories starting from different initial configurations were performed for each loading with a time step of 0.2 fs. The equations of motion were propagated according to the velocity-Verlet algorithm, and the

temperature was maintained at 300 K by a Nosé-Hoover chain of four thermostats.[177] Short-range interactions were truncated at an atom–atom distance of 9.0 Å, and the electrostatics were calculated using the Ewald sum.[80] Standard long-range electrostatic interactions as implemented in DL_POLY_2 were applied to Lennard-Jones potentials to account for errors due to the truncation at 9 Å.[176] Cross interactions between water and the MOF were derived from Lorentz-Berthelot mixing rules.

3.4 Data availability

Any data generated and analyzed for this study that are not included in this Article and its Supplementary Information are available from the authors upon request.

3.5 Code availability

The MB-pol water model used in this study is available in OpenMM (http://paesanigroup.ucsd.edu/software/mbpol_openmm.html) and i-PI (http://paesanigroup.ucsd.edu/software/mbx.html). All computer codes used in the analysis presented in this study are available from the authors upon request.

3.6 Acknowledgments

Studies of small molecule interactions with metal nodes in MOFs are supported through a CAREER grant from the National Science Foundation to M.D. (DMR-1452612). A.J.R. is supported by the Martin Family Fellowship for Sustainability. A.J.R. and M.D. thank the Abdul Latif Jameel World Water and Food Security Lab for seed funding for water capture. Theoretical research is supported by the Department of Energy through grant no. DE-SC0019333 to F.P. and used computational resources of the Extreme Science and Engineering Discovery Environment

(XSEDE), which is supported by the National Science Foundation through grant no. ACI-1053575 under allocation TG-CHE110009, as well as of the Air Force Office of Scientific Research through grant no. FA9550-16-1-0327.

3.7 Author contributions

The paper was written through contributions of all authors. A.J.R. and K.M.H. contributed equally to this work. A.J.R. synthesized materials and designed and performed infrared experiments. K.M.H. designed and performed theoretical calculations. M.D. and F.P. designed and supervised research.

3.8 Competing interests

A.J.R. and M.D. are inventors on a patent pertaining to the materials discussed herein. K.M.H. and F.P. declare no competing interests.

3.9 Additional information

Supplementary information is available for this paper at https://doi.org/10.1038/s41467-019-12751-z.

Chapter 3, in full, is a reprint of the material as it appears in "Hydrogen Bonding Structure of Confined Water Templated by a Metal-Organic Framework with Open Metal Sites", Rieth, A.J.; Hunter, K.M.; Dincă, M.; Paesani, F.; Nat. Commun., 10, 4771, 2019. The dissertation author was the co-primary investigator and co-author of this paper.

Chapter 4

Simulation Meets Experiment: Unraveling the Properties of Water in Metal–Organic Frameworks through Vibrational Spectroscopy

4.1 Introduction

Hydrogen bonding (H-bonding) between water and host materials has proven to be important for the structure and function of the latter.[178–180] Strong H-bonds can lead to the formation of extended networks that modulate fundamental processes, including hydration processes,[181] chemical synthesis and reactions,[182,183] heat dissipation,[184,185] and macroscopic structural formations.[184,186–188] Under confinement, H-bonded networks are disrupted due to physical constraints and host–water interactions.[184,189] A variety of porous materials, such as carbon nanotubes,[150,152,190–192] zeolites,[153] silica pores and channels,[189,193] and other materials[194,195] have been used as model systems to determine the physical properties of water in confinement.

These model systems highlight the fact that the properties of the confining environment, whether hydrophobic or hydrophilic, influence H-bonding with the host.

Metal-organic frameworks (MOFs) are an attractive class of porous materials. Comprised of inorganic subunits, also known as secondary building units (SBUs), and organic linkers, MOFs assemble in crystalline three-dimensional structures with large surface areas and high porosity.[34] Because of their chemical diversity and tunability, MOFs have found a wide range of applications including, but not limited to, liquid and gas adsorption,[38,40,196,197] chemical separation,[9,26] catalysis,[198] chemical degradation,[199] and proton transport,[200] as well as in electronic devices[201] and magnets.[202] It has recently been shown that some MOFs display remarkable water capture capabilities under ambient conditions.[41,44,203–205] To further capitalize on the potential of MOFs as water harvesting materials, it is necessary to gain fundamental insights on the framework–water and water–water interactions in the confining pores, as these interactions determine both the onset and overall capacity of water adsorption.

An accurate description of the water H-bonding network in MOFs, which can allow for unambiguously disentangling framework–water and water–water interactions, is critical for understanding the physical mechanisms governing water adsorption in MOFs as a function of pore size and shape as well as the physicochemical properties of the framework. In this regard, an integrated approach that combines spectroscopic measurements and molecular simulations can provide such a level of detail. Linear infrared (IR) spectroscopy is sensitive to variations in the strength of the water H-bonding network,[93] although all measurements are performed at the ensemble-averaged level, and the decoding of structure from the spectra is often challenging. On the other hand, molecular dynamics (MD) simulations provides a means to directly connect different spectroscopic features to specific H-bonding motifs. However, the calculated spectra, and, therefore, the reliability of the comparisons with the experimental measurements depend sensitively on the ability of the molecular models to correctly describe the underlying molecular interactions.

Diffuse reflection infrared Fourier transform spectroscopy (DRIFTS) can provide functional group-specific information regarding the interaction between water and the framework. A study carried out on MIL-53(Al), which exhibits the so-called "breathing effect", highlighted the complex mechanisms that modulate water adsorption in this MOF.[206] It was determined that water interacts tightly with multiple sites of the framework at lower hydration levels, while at higher hydration levels the spectral signatures associated with the water OH stretching vibrations are localized to fewer sites of the framework. A study on the Co_2Cl_2BTDD MOF, a hydrophilic MOF that captures 82% water by weight below 30% relative humidity (RH),[41] used DRIFTS to elucidate the adsorption mechanism as a function of RH.[207] Results from Ref. 207 provide a different picture from that derived from the analysis of the IR spectra of water in MIL-53(Al). Water was found to strongly bind to the open Co^{2+} sites of the framework at low RH and to subsequently form disconnected one-dimensional chains of H-bonded molecules bridging between the Co^{2+} sites. Upon further increase in RH, these water chains were found to nucleate pore filling, with water molecules occupying the entire pore volume before the RH reaches 30%. The different results from Refs. 206 and 207 exemplify not only the power of IR spectroscopy in providing functional group-specific information about the water adsorption process but also the variety of hydration mechanisms that can be observed in MOFs, depending on the pore sizes, shapes, and nature of the framework.

On the modeling side, one of the major challenges faced by MD simulations of MOFs is the development of force fields (FFs) that can accurately describe the underlying molecular interactions. Common FFs such as the general Amber force field (GAFF)[81] and the universal force field (UFF)[82] have been used to represent the organic linkers of MOFs. These FFs have the advantage of being applicable to a wide range of systems, although they suffer from a lack of transferability in describing the coordination and geometry of metal centers in MOFs.[84,85] More specific FFs have been developed to address this deficiency, such as MOF-FF[85] and QuickFF,[83] extensions of UFF for MOFs (UFF4MOF),[84,86] and a zeolitic imidazolate framework force field

(ZIF-FF).[87] These FFs have been extensively used to simulate adsorption isotherms as well as structural, thermodynamic, and dynamical properties of various molecules (e.g., methane and small hydrocarbons, carbon dioxide, and water) adsorbed in the MOF pores. Recently, more sophisticated polarizable models have also been used to model guest–framework interactions.[89,208–212] Among different guest molecules, modeling water in MOFs presents particular challenges due to the complex nature of the water–water interactions, which is responsible for the anomalous behavior of water as a function of temperature and pressure.[45,144,147]

In this study, we integrate experimental and computational IR spectroscopy with MD simulations to investigate the properties of water in ZIF-90. Compared to most ZIFs that are highly hydrophobic (e.g., ZIF-8),[36,43,213] ZIF-90 gives rise to a sharp step in the water adsorption isotherm between 30% and 40% RH (Fig. 4.1A) due to the presence of the imidazolate-2-carboxyaldehyde linkers, which make the framework hydrophilic.[214] While the overarching goal of this study is to gain general insights into the interplay between framework–water and water–water interactions, direct comparisons between experimental and simulated IR spectra also provide the unique opportunity to assess both merits and shortcomings of current models for MOF simulations and computational IR spectroscopy as well as to identify possible areas of improvement, which are critical for *in silico* screening of MOFs for water harvesting.

4.2 Methods

4.2.1 Material Synthesis and Characterization

ZIF-90 was synthesized by fully dissolving imidazole-2-carboxaldehyde (ICA) in N,N-dimethyl-formamide (DMF) with heat as described in Ref. 215. The ICA/DMF solution was cooled to room temperature, and pyridine was added. A solution of zinc nitrate hexahydrate in methanol was poured into the ICA/pyridine/DMF solution rapidly and mixed overnight. ZIF-90 crystals were collected through 4 cycles of centrifugation with neat DMF. The collected product

was then washed with DMF and dried. To confirm the synthesis of ZIF-90, the product was analyzed using Powder X-Ray Diffraction (PXRD) and Scanning Electron Microscopy (SEM). PXRD data match well with theoretically simulated spectra, and obtained SEM images visually confirm the crystal structure of ZIF-90 (Figs. S1 and S2, respectively).

4.2.2 Spectroscopic Measurements

DRIFTS measurements were carried out on ZIF-90 crystal powder mixed with dry KBr at 5% (w/w) using a Thermo Fischer Nicolet S10 FTIR spectrophotometer fitted with a PIKE Technologies DiffusIR accessory. The enclosed internal space of the DiffusIR accessory was purged with varying degrees of D_2O humidified air using a humidity generator (Fig. S3). Briefly, dry air streams were mixed with D_2O humidified air until the desired humidity was generated. The enclosed internal space of the accessory was then allowed to equilibrate for 10 minutes before each spectrum and background were recorded. A background spectrum of solid potassium bromide (KBr) was taken for each RH value to correct for signal scatter using a Kubelka-Munk transform.

4.2.3 Molecular Models and Simulations

ZIF-90 was modeled using a flexible force field. All bonded parameters involving the zinc atom were taken from ZIF-FF,[87] while all bonded parameters involving the atoms of the ligand were taken from the General Amber Force Field (GAFF).[81] The MOF structure was optimized using periodic density functional theory (DFT) calculations carried out with the Vienna Ab initio Simulation Package (VASP),[216–219] using the PBE exchange-correlation functional[220] with Grimme's D3 dispersion correction[221] in combination with a projector-augmented wave (PAW) treatment[222,223] with a 700 eV kinetic energy cutoff. A $2\times2\times2$ k-point grid was used, and forces were converged to a tolerance of 0.03 eV/Å. Atomic point charges were calculated

for the optimized ZIF-90 structure using the density derived electrostatic and chemical (DDEC) charges.[90] The Lennard-Jones (LJ) parameters were taken from ZIF-FF with an initial guess used for the oxygen atom of the framework from the LJ r_{min} value in GAFF.[81] Atom types as well as all bonded and non-bonded parameters for the MOF force field are given in Fig. S4 and Tables S1-S4.

Water was modeled using the MB-pol potential energy function (PEF).[60–62] MB-pol has been shown to correctly predict the properties of water from the gas to the condensed phase,[63,167] which makes it particularly well-suited for modeling the properties of water adsorbed in MOFs as a function of RH. Furthermore, MB-pol enables accurate simulations of vibrational spectra of water clusters,[60,65,70] liquid water,[71–74] the air/water interface,[75,76] and ice,[77–79] and is thus an ideal model to monitor the evolution of the DRIFTS spectra of water adsorbed in MOFs as a function of RH.[207]

As in Ref. 207, the framework–water non-bonded interactions were represented in terms of permanent electrostatics and Lennard-Jones (LJ) interactions. Since the extension of our many-body models to generic molecules compatible with MB-pol is under development,[224,225] in this study the LJ parameters between the MOF atoms and water were obtained by applying the Lorentz-Berthelot mixing rules using the LJ parameters of the TIP4P/2005 water model,[226] which is the closest point-charge model to MB-pol.[137]

All MD simulations were carried out in periodic boundary conditions for systems consisting of $2\times2\times2$ primitive cells of ZIF-90 and various water loadings, ranging from 25% to 70% RH, using in-house software based on the DL_POLY_2 simulation package.[176] Constant pressure and constant temperature (NPT) simulations at 1.0 atm and 300 K were performed for 500 ps at each water loading. Since the average box dimensions do not deviate significantly from the experimental values (see Table S5 in the Supporting Information), the latter were used in all simulations to guarantee direct comparisons with the experimental measurements. Each system was equilibrated in the canonical (constant number of atoms, volume, and temperature, NVT)

ensemble at 300 K for 1 ns. All dynamical properties, including the IR spectra, were calculated in the microcanonical (constant number of atoms, volume, and energy, NVE) ensemble at 300 K by averaging over 20, 50 ps long independent trajectories. The equations of motion were propagated according to the velocity-Verlet algorithm with a time step of 0.2 fs, and the temperature was maintained at 300 K by a Nosé-Hoover chain of four thermostats. Short-range interactions were truncated at an atom–atom distance of 15.0 Å, and long-range electrostatics were calculated using the Ewald sum.[80]

To assess the importance of nuclear quantum effects in determining the structural and dynamical properties of water adsorbed in ZIF-90, centroid molecular dynamics (CMD) simulations[124–128] were also performed. In the CMD simulations, each atom was represented by a Feynman's ring polymer discretized with 32 beads, and the centroid variables were propagated using the partially adiabatic separation scheme of Refs. 127 and 129, with an adiabaticity parameter of γ=0.25 and a time step of 0.05 fs. Given the associated computational cost, all CMD simulations were only performed for systems consisting of $1\times1\times1$ primitive cells of ZIF-90 at 40% RH.

The theoretical IR spectra were calculated within the time-dependent formalism according to

$$I_{IR} = \left[\frac{2\omega}{3V\hbar c\varepsilon_0}\right] tanh\left(\beta\hbar\omega\right) \int_{-\infty}^{\infty} e^{i\omega t} \left\langle \mu(0)\mu(t)\right\rangle dt \tag{4.1}$$

where V is the system volume, c is the speed of light in vacuum, ε_0 is the permittivity of free space, and $\beta = (k_B T)^{-1}$, with k_B being Boltzmann's constant. In Eq. 4.1, $\langle\mu(0)\mu(t)\rangle$ is the ensemble-averaged dipole-dipole time correlation function that was calculated by averaging over 20 NVE trajectories at each water loading, with μ being represented by the MB-μ many-body dipole moment function.[71] Since MB-pol is a polarizable water model, the ZIF-90 atoms can polarize water confined in the MOF, and the induced dipole moment of MB-μ includes contributions from the MOF atoms.

Due to the neglect of nuclear quantum effects, classical MD simulations predict vibra-

tional spectra that are systematically blue-shifted relative to the corresponding experimental spectra.[71,75,227,228] Therefore, in all the analyses presented in the following sections, the theoretical spectra calculated from classical MD simulations are red-shifted by 137 cm^{-1} in the stretching region, as shown in Fig. S5 in the Supporting Information, to facilitate comparisons with the experimental DRIFTS spectra. Furthermore, MB-pol has been shown to slightly underestimate the strength of H-bonds in liquid water, which results in a blue-shift of 57 cm^{-1} in the OH stretching region of the quantum CMD spectra.[71] In the following analyses, the quantum CMD spectra are thus red-shifted by 57 cm^{-1} (Fig. S5) to facilitate comparisons with the experimental DRIFTS spectra.

Finally, Fermi resonances between the overtones of the bending vibrations and stretching vibrations of the water molecules in the liquid phase have been shown to be important for a quantitative representation of the OH-stretch lineshape in both water clusters[65,130] and liquid water.[74] To calculate the Fermi resonance contributions to the OD-stretch lineshape, local mode/local monomer (LM) calculations[57,122,123] were performed on clusters comprised of a central D_2O molecule surrounded by 16 H_2O molecules, which were used to model the intramolecular (bending and stretching) modes of D_2O in the liquid phase. These clusters were the same clusters used in Ref. 74, which were extracted from CMD simulations of a single H_2O in a D_2O solution. The two hydrogen atoms on the H_2O molecule were optimized, while every other atom was held fixed, using the ORCA package[229] interfaced with our in-house MB-pol software. After this optimization, the central H_2O molecule was converted to D_2O while the 16 surrounding D_2O molecules in the cluster were converted to H_2O for the LM calculations.

4.3 Results and Discussion

ZIF-90 exhibits a type V adsorption isotherm (Fig. 4.1A),[36] adsorbing water in one pore-filling step that begins at ∼30% RH and ends at ∼40% RH. To facilitate the analysis of the IR

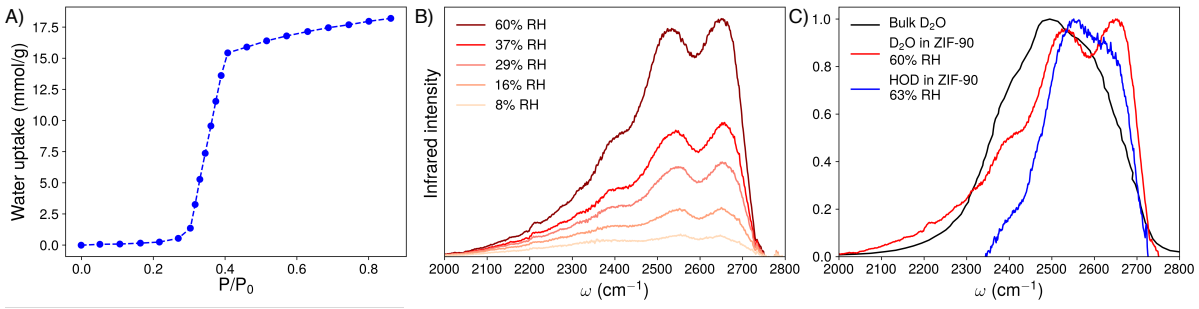

Figure 4.1: A) Water adsorption isotherm for ZIF-90 from Ref. 36. B) Experimental IR spectra of D_2O in ZIF-90 at 8% RH, 16% RH, 29% RH, 37% RH, and 60% RH. C) IR spectra of experimental bulk D_2O (black) from Ref. 1, D_2O in ZIF-90 at 60% RH (red), and HOD in ZIF-90 at 63% RH (blue). The spectra are normalized to a value of one.

spectra, all measurements and simulations were carried out with D_2O since the OD stretching vibrations do not overlap with any of the framework vibrations. The experimental IR spectra of D_2O in ZIF-90 in the OD stretching region, obtained after subtracting the spectrum measured at 0% RH from the spectra measured at different RH values, are shown in Fig. 4.1B. As the humidity increases to $\sim$10%, two peaks centered at $\sim$2550 and $\sim$2650 cm^{-1} begin to develop, with their intensity monotonically increasing as the RH increases. Importantly, Fig. 4.1B also shows that the spectral weight shifts from the lower to the higher frequency portion of the lineshape as the RH increases. The comparison with the IR spectrum of bulk D_2O (Fig. 4.1C) indicates that ZIF-90 induces a blue shift of $\sim$40 cm^{-1} to the OD lineshape of the adsorbed D_2O molecules. The OD lineshape in ZIF-90 displays appreciably higher intensity on the blue side of the maximum at 2650 cm^{-1}. Importantly, DRIFTS measurements carried out for HOD in ZIF-90 (Fig. 4.1C) provide a significantly narrower OD-stretch lineshape that lacks the two distinct peaks that characterize the analogous OD-stretch of D_2O in ZIF-90. Furthermore, the absence of intramolecular coupling in the HOD molecules results in a decrease of the IR intensity on the red side of the spectrum around $\sim$2400 cm^{-1}. The comparison of the IR spectra of D_2O and HOD in ZIF-90 thus allows us to unambiguously assign the shoulder at $\sim$2400 cm^{-1} in the D_2O spectrum to the Fermi resonances and not to particular ice-like structures of D_2O in the ZIF-90 pores.

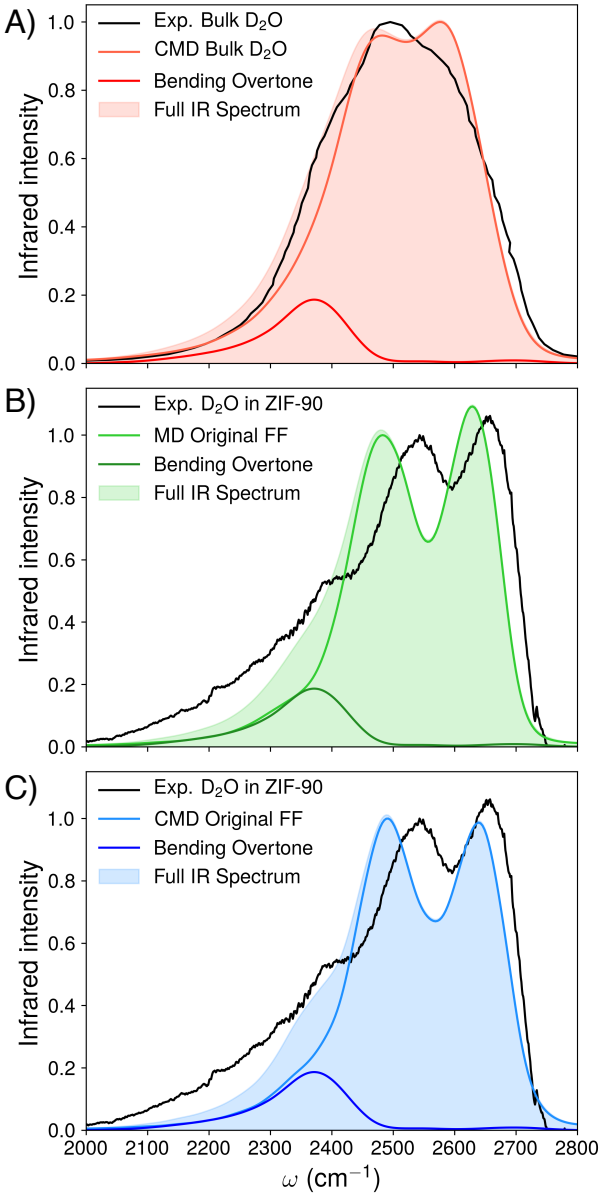

Figure 4.2: A) Experimental bulk D_2O IR spectrum (black) from Ref. 1, CMD bulk D_2O (pink) spectrum, Fermi resonance contribution (red), and CMD bulk D_2O spectrum with added Fermi resonance contribution (shaded pink). B) Experimental IR spectrum of water in ZIF-90 at 40% RH (black), MD 40% RH (green) spectrum, Fermi resonance contribution (dark green), and MD 40% RH spectrum with added Fermi resonance contribution (shaded green). C) Experimental IR spectrum of water in ZIF-90 at 40% RH (black), CMD 40% RH (light blue) spectrum, Fermi resonance contribution (blue), and CMD 40% RH spectrum with added Fermi resonance contribution (shaded light blue). All MD spectra are red-shifted by 137 cm^{-1}, CMD spectra are red-shifted by 57 cm^{-1}, DOD bending overtones are blue-shifted by 24 cm^{-1}, and all spectra are normalized to a value of one at the lower frequency peak.

To gain insights into the adsorption process, IR spectra were calculated from both MD and CMD simulations carried out at different D_2O loadings. Fig. 4.2 shows a comparison between the experimental, MD, and CMD OD-stretch lineshapes at 300 K. As discussed in Ref. 74, due to numerical limitations associated with using Cartesian coordinates to propagate the dynamical trajectories, the lineshape calculated using quantum CMD simulations is unable to quantitatively describe Fermi resonances.[230,231] On the other hand, the Fermi resonances do not appear in the lineshape calculated using classical MD simulations because, in this case, the overtones of the bending vibrations do not overlap with the OD stretching vibrations. Fig. 4.2A shows the experimental and simulated CMD IR spectrum of bulk D_2O. The CMD spectrum is able to reproduce the experimental D_2O spectrum fairly well, only lacking intensity around $\sim$2400 cm^{-1}, which is due to missing intensity from the Fermi resonances.[74] This inability to reproduce Fermi resonances leads to two distinct peaks in the CMD spectrum of bulk D_2O instead of the single, broad peak with two shoulders observed in the experimental spectrum (Fig. 4.2A). After adding the contributions from the Fermi resonances (red trace), the resulting CMD OD-stretch lineshape of bulk D_2O is in remarkably good agreement with the corresponding experimental lineshape.

Figs. 4.2B and 4.2C show comparisons between the experimental and theoretical lineshapes for D_2O in ZIF-90 at 40% RH calculated from both (classical) MD and (quantum) CMD simulations, respectively. While the simulated lineshapes correctly reproduce both the blue shift of the OD-stretch linesahpe measured experimentally (Fig. S7) and the presence of two distinct peaks, both MD and CMD lineshapes overestimate the separation between the two peaks compared to experiment.

The origin of the blue shift can be explained by investigating the structure of bulk D_2O and D_2O in ZIF-90. As shown in Table 4.1, D_2O molecules adsorbed in MOF pores form longer, and, consequently, weaker D-bonds compared to bulk. These longer D-bonds are associated with OD stretching vibrations that absorb at relatively higher frequencies, causing the blue shift of the OD-stretch lineshape found for D_2O confined in the ZIF-90 pores.

Table 4.1: Average OD bond, water–water (OW–OW) D-bond lengths, and water–MOF (OW–o) D-bond lengths calculated from MD and CMD simulations for bulk D_2O as well as ZIF-90 at 40% RH using both the original and modified force fields.

	simulation	OD bond (Å)	D-bond (Å) OW–OW	D-bond (Å) OW–o
bulk D_2O	CMD	0.976	1.916	
ZIF-90 40% RH (original FF)	CMD	0.973	1.937	2.146
ZIF-90 40% RH (original FF)	MD	0.969	1.943	2.147
ZIF-90 40% RH (modified FF)	CMD	0.975	1.945	1.713
ZIF-90 40% RH (modified FF)	MD	0.970	1.950	1.715

Since it has been shown that MB-pol correctly describes the properties[63] and IR spectrum of bulk D_2O (Fig. 4.2A), the differences between the experimental and simulated IR spectra of D_2O in ZIF-90 are likely due to an inaccurate representation of the interactions between the D_2O molecules and the ZIF-90 framework. The present simulations (Fig. S9) as well as other studies of water in ZIF-90[43] indicate that the D_2O molecules adsorbed in the ZIF-90 pores can D-bond to the carbonyl groups of the framework. Furthermore, Figs. 4.2B and 4.2C show that, compared to experimental results, the low-frequency peak in both MD and CMD OD-stretch lineshapes is red-shifted and misses intensity around $\sim$2550 cm^{-1}. This frequency region corresponds to OD stretching vibrations of D_2O molecules that are D-bonded to the carbonyl groups of the framework.[232]

In order to more accurately describe the strength of D-bonding between the D_2O molecules and the framework, we modified the LJ potential between the D_2O oxygen atom (OW) and the oxygen atom (o) of the carbonyl functional groups of the framework by decreasing σ_{OW-o} by 10%

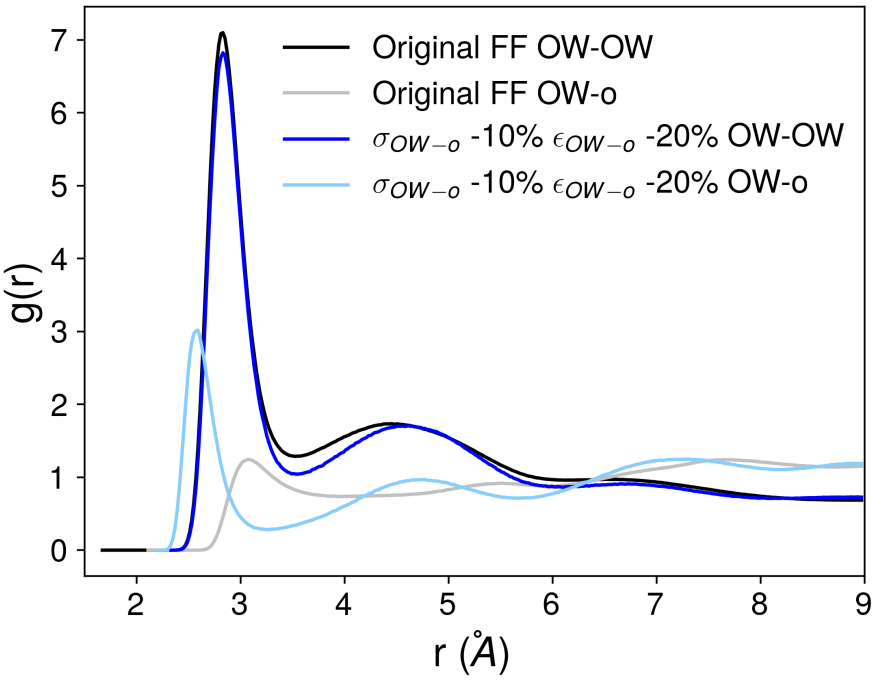

Figure 4.3: OW–OW (dark colors) and OW–o (light colors) RDFs of water confined in ZIF-90 in the original force field (black colors) and the modified force field (blue colors).

and ε_{OW-o} by 20%, which leads to a modified FF. By doing this, the OW–o repulsion decreases, which allows the D_2O molecules to approach the framework more closely and establish stronger D-bonds with the carbonyl groups.

The effects of modifying the OW–o LJ potential can be directly seen in the differences between the radial distribution functions (RDFs) calculated from MD simulations carried out with the original and modified FFs (Fig. 4.3) as well as in the average water–MOF D-bond length in Table 4.1. In the original FF, the first peak in the OW–OW RDF is located at 2.8 Å (black), while the first peak in the OW–o RDF is at 3.1 Å (gray), suggesting that the D_2O molecules approach each other closer than D_2O molecules can approach the MOF atoms. On the other hand, the first peak in the OW–OW RDF remains at 2.8 Å (royal blue) but the first peak in the OW–o RDF moves to 2.55 Å (light blue) with the modified FF. This indicates that, while the interaction between D_2O molecules is not affected by changes in the framework–D_2O interactions, the modified FF

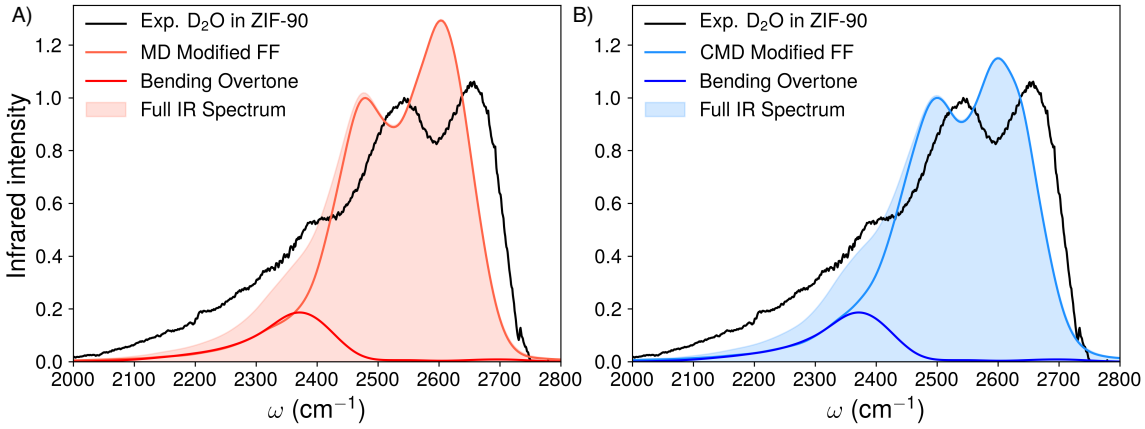

Figure 4.4: A) IR spectra of water in ZIF-90 at 40% RH from experiment (black), MD at 40% RH for the modified FF (pink), Fermi resonance contribution (red), and MD at 40% RH with added Fermi resonance contribution for the modified FF (shaded pink). B) IR spectra of water in ZIF-90 at 40% RH from experiment (black), CMD at 40% RH for the modified FF (light blue), Fermi resonance contribution (blue), and CMD at 40% RH with added Fermi resonance contribution for the modified FF (shaded light blue). All MD spectra are red-shifted by 137 cm^{-1}, CMD spectra are red-shifted by 57 cm^{-1}, and DOD overtones are blue-shifted by 24 cm^{-1}. All spectra are normalized to a value of one at the lower frequency peak.

leads to D_2O molecules forming shorter and stronger D-bonds with the framework than in the original FF (Table 4.1). It should be noted that other modifications of the original FF were also investigated and were found to significantly affect the D_2O structure in the ZIF-90 pores, leading to large deviations in both RDFs and IR spectra as shown in the Supporting Information (Figs. S10, S11, and S12).

The influence of modifying the OW–o LJ potential is clearly seen in the IR spectra calculated from MD and CMD simulations which are shown in Fig. 4.4A and Fig. 4.4B, respectively. Decreasing σ_{OW-o} by 10% and decreasing ε_{OW-o} by 20% in the modified FF redistributes the IR intensity between ~2500-2550 cm^{-1}. Specifically, the shorter water–MOF D-bonds in the modified FF move the IR intensity from the high-frequency range to the mid-frequency range of the OD-stretch lineshape, leaving the low-frequency peak of the strongest D-bonds between water molecules unchanged. With the modified FF, the CMD simulation closely reproduces the intensity of the two main peaks of the experimental spectrum at ~2550 and ~2650 cm^{-1}. Furthermore,

adding the Fermi resonance contributions increases the intensity on the red side of both the MD and CMD OD-stretch lineshapes, which makes the CMD lineshape reproduce the corresponding experimental lineshape nearly quantitatively. As seen in Table 4.1, simulations with the modified FF also lead to slightly longer OW–OW D-bond which results in the loss of some IR intensity from the lower-frequency peak at $\sim$2450 cm^{-1} (Fig. 4.4).

To provide further insights into the structural arrangements of the D_2O molecules in the ZIF-90 pores in connection with the OD-stretch lineshape, Fig. 4.5 shows the distribution of different D-bond topologies for both bulk D_2O and D_2O in ZIF-90 at 40% RH. The majority of bulk D_2O molecules donate and accept at least one D-bond, with the varying number of donors and acceptors resulting in the broad OD-stretch band. On the other hand, the MD simulations of D_2O in ZIF-90 carried out with the original FF indicate that, among D_2O molecules not involved in D-bonding with the framework (Fig. 4.5A), a relatively smaller fraction donates and accepts at least one D-bond compared to bulk D_2O. When the D_2O molecules donate one D-bond to the framework (Fig. 4.5B), the fraction of D_2O molecules that are involved in D-bonding with themselves is significantly smaller than in bulk D_2O. Therefore, due to the overall smaller number of D-bond donors and acceptors, the vibrations of the D_2O molecules confined in ZIF-90 retain some character of the symmetric and asymmetric stretches of gas-phase D_2O, which results in the two distinct peaks found in the IR spectra.

The comparison between the D-bonding topologies obtained with the original and modified FFs indicates that the latter leads to an overall decrease in the number of D_2O molecules that are D-bonded with themselves when the D_2O molecules are not involved in D-bonding with the framework (Fig. 4.5A). This is accompanied by an overall increase of D_2O molecules that donate D-bonds to the carbonyl groups of the framework, whose fraction increases from 25% in the MD simulations with the original FF to 40% in the MD simulations with the modified FF (Fig. 4.5B), resulting in a more tetrahedral arrangement of the D_2O molecules in the ZIF-90 pores (Fig. S13). The structure of the D-bonding network at 40% RH obtained from MD simulations with MB-pol

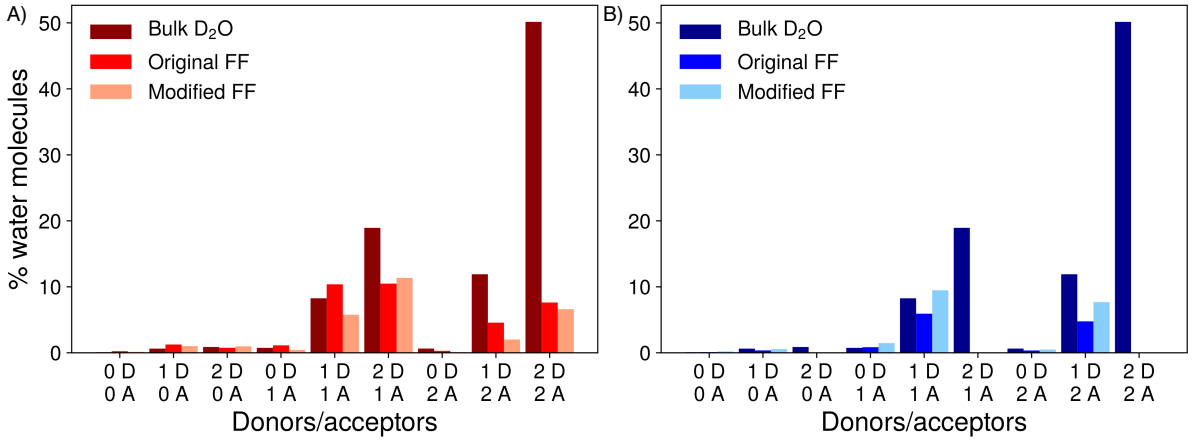

Figure 4.5: A) Donating (D) and accepting (A) D-bond distribution of water molecules when there are zero D-bonds donated to the MOF at 40% RH. D-bond distributions are shown for bulk D_2O (dark red), the original FF (red), and the modified FF (light red). D-bonds are plotted as a percent of the total number of water molecules in each simulation. B) Donating (D) and accepting (A) D-bond distribution of water molecules when there is one D-bond donated to the MOF at 40% RH. D-bond distributions are shown for bulk D_2O (dark blue), the original FF (blue), and the modified FF (light blue). D-bonds are plotted as a percent of the total number of water molecules in each simulation.

is compared in Fig. S14 of the Supporting Information to that obtained from simulations with the empirical and nonpolarizable q-TIP4P/f water model.[233] While the two sets of simulations provide similar trends, q-TIP4P/f overall predicts a larger number of water molecules donating two hydrogen bonds to other water molecules. These results are consistent with q-TIP4P/f also predicting a more tetrahedral structure of liquid water compared to MB-pol.[62] As shown in Ref. 89, the differences between polarizable and nonpolarizable models of water become more pronounced in MOFs with frameworks containing charged functional groups that polarize the water molecules and lead to the formation of strong hydrogen bonds. Given the differences in strength between the stronger D_2O–D_2O and weaker D_2O–carbonyl D-bonds,[232] this analysis demonstrates that the rearrangements of the D-bonding network predicted by the MD simulations with the modified FF are responsible for the redistribution of the IR intensity in the ∼2500-2550 cm^{-1} frequency range of the simulated OD-stretch lineshape shown in Fig. 4.4.

A small red shift between the experimental and simulated OD-stretch lineshapes still

remains after modifying the FF and including the Fermi resonances (Fig. 4.4). In this context, it should be reminded that the intrinsic shifts applied the simulated lineshapes are based on the analysis of the IR spectrum of bulk D_2O. As highlighted in Fig. 4.1C, there is a $\sim$40 cm^{-1} blue shift in the experimental spectra of D_2O confined in ZIF-90 relative to bulk D_2O. This blue shift accounts for the small differences that remain in the higher-frequency portion of the lineshape. Although the level of agreement with the experimental OD-stretch lineshape is nearly quantitative, the simulated lineshapes display slightly lower intensities between 2000 cm^{-1} and 2400 cm^{-1}. As discussed above, this frequency range is primarily associated with Fermi resonances. While this is the first study where Fermi resonance contributions are included in simulations of the IR spectra of water in MOFs, state-of-the-art calculations currently only allow for determining these contributions from simulations of relatively small gas-phase water clusters. This approximation is likely responsible for the remaining differences between experimental and simulated lineshapes in the 2000-2400 cm^{-1} frequency region.

4.4 Conclusions

In this study, we have characterized the structure of D_2O adsorbed in ZIF-90 as a function of relative humidity by integrating experimental and computational IR spectroscopy. Due to the confining environment provided by the framework, the D_2O molecules are found to establish longer and relatively weaker D-bonds that manifest in an OD-stretch band that is blue shifted compared to bulk. A systematic analysis of the OD-stretch band, carried out using both (classical) MD and (quantum) CMD simulations demonstrates the importance of explicitly taking into account both Fermi resonances and nuclear quantum effects. Our simulations indicate that the D_2O molecules preferentially interact with the carbonyl groups of the framework. However, it is found that "off-the-shelf" force fields commonly used in MD simulations of MOFs are unable to correctly represent the strength of the framework–water interactions. If polarizable

force fields similar to the MB-pol water model, such as those recently developed for small molecules,[224,225] were developed for MOFs, the description of framework–water interactions could be improved and could thus remove the need for modifications between various force fields. Guided by direct comparisons with the experimental OD-stretch lineshape, we have demonstrated that it is possible to use the comparison between experimental and simulated IR spectra to guide the refinement of the force field parameterization representing the framework–water interactions. This "reverse engineering" process has led to a refined set of Lennard-Jones parameters describing the interactions between the oxygen atoms of the water molecules and the carbonyl groups of the framework, which results in nearly quantitative agreement between the experimental and simulated OD-stretch lineshapes and, in turn, allows for an accurate, molecular-level characterization of the structural arrangements of the D_2O molecules inside the ZIF-90 pores. Our results suggest that the integration of experimental and computational vibrational spectroscopy can play an important role in characterizing the molecular properties of water adsorbed in MOFs and identifying key framework–water interactions, which is critical for the design of efficient MOF-based materials for water harvesting.

4.5 Supporting Information

Experimental PXRD, SEM, and humidity generator; all force field parameters for ZIF-90; additional comparisons of experimental and simulated IR spectra; structural and dynamical properties of water confined in ZIF-90.

4.6 Acknowledgments

This research was supported by the Department of Energy under contract DE-SC0019333 and the National Science Foundation through grant No. CHE-1704063. All simulations used

resources of the National Energy Research Scientific Computing Center (NERSC), which is supported by the Office of Science of the U.S. Department of Energy under contract DE-AC02-05CH11231, the Extreme Science and Engineering Discovery Environment (XSEDE), which is supported by the National Science Foundation through award No. ACI-1548562, as well as the Triton Shared Computing Cluster (TSCC) at the San Diego Supercomputer Center (SDSC). M.K. is supported by the Department of Defense (DoD) through the National Defense Science and Engineering Graduate (NDSEG) Fellowship and is the recipient of an Achievement Rewards for College Scientists (ARCS) Foundation Fellowship.

Chapter 4, in full, is a reprint of the material as it appears in "Simulations Meets Experiment: Unraveling the Properties of Water in Metal-Organic Frameworks through Vibrational Spectroscopy", Hunter, K.M.; Wagner, J.C.; Kalaj, M.; Cohen, S.M.; Xiong, W.; Paesani, F.; J. Phys. Chem. C, 125, 12451-12460, 2021. The dissertation author was the primary investigator and author of this paper.

Chapter 5

Water Capture Mechanisms at Zeolitic Imidazolate Framework Interfaces

Interest in atmospheric water capture materials has grown recently as the supply of fresh water becomes scarce. Metal-organic frameworks (MOFs), a class of porous crystalline solids composed of transition metal centers coordinated to organic linkers, hold great promise for water harvesting due to their high porosity and tunability. Understanding the water capture mechanisms is crucial to rationally designing MOFs for energy-efficient water capture.[2,38,40,234]

Among different water adsorption mechanisms in MOFs,[2,38,40] the layer/cluster adsorption is a common mechanism in which water clusters are first formed through nucleation on hydrophilic sites in the MOF (detailed description of water cluster in SI S6 Figure 13a). Then, water uptake at the center of the pore occurs through reversible pore filling.[38] While the mechanistic step is clear, molecular-level details are missing.[235,236] For example, water clustering and center pore filling could occur sequentially on single pore levels, but simultaneously overall (mechanism 1, Figure 5.1). Alternatively, water clusters could form in every pore at a certain relative humidity (RH) and, after all pores have water clusters near the hydrophilic sites, center pore filling starts (mechanism 2, Figure 5.1).

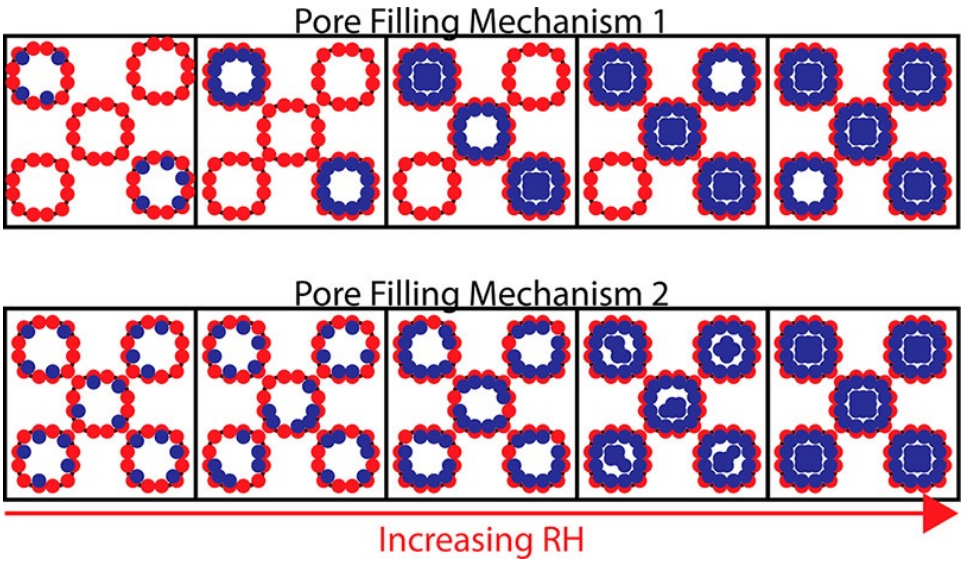

Figure 5.1: Proposed layer/cluster mechanism. In mechanism 1, individual pores are filled before additional pores are filled, while in mechanism 2, all pores fill simultaneously at a similar rate. Note: cluster and pore sizes are not to scale.

The lack of mechanistic detail is largely due to the difficulty in separately probing water clustering and pore filling. The initial water cluster formation happens at the interior surface of MOFs, which requires interfacial specific techniques to probe. Adsorption/desorption isotherms,[237–239] a common method to study MOFs, only report the number of water molecules in the pores. Diffuse reflectance infrared Fourier transform spectroscopy (DRIFTS) can only probe the molecular details of bulk water in MOFs.[207,240–244] Although diffraction techniques have revealed molecular-level details of water adsorption in MOFs, applications to investigating the pore filling mechanism have been limited.[15,245–247] On the other hand, molecular dynamics (MD) simulations can provide molecular-level insights into interfacial processes but often lack corresponding experimental comparison.[43,207,240,248,249]

Here, by selectively probing the water clustering step, using a spatially resolved vibrational sum-frequency generation (VSFG) spectroscopy and MD simulations with the MBpol[60–62] water model,[240] we study the water uptake mechanism of ZIF-90, a hydrophilic MOF that can adsorb water at low RH without open metal sites and be modified postsynthetically.[250,251] We find that

ZIF-90 adsorbs water by mechanism 1. This study emphasizes the importance of interface-specific techniques,[252–257] determining that the competition between water–water and water–framework interactions dictates the uptake mechanism. Understanding ZIF-90 water uptake mechanism lays the foundation to further optimize its and other MOF's water harvesting function through post synthesis.

Two crucial technical aspects enable the micron-resolved VSFG to probe adsorbed water at interior MOF surfaces. First, ZIF-90 lacks inversion symmetry ($I\bar{4}3m$ space group), making it VSFG active, which is evident by its strong second-order nonresonant signal (broad feature at 2600 cm^{-1}).[258] Then, when water adsorbs on the interior interfaces, it becomes VSFG active, because the interactions between water and the hydrophilic groups of ZIF-90 template the water network and transfer the symmetry from the framework to water.[184,259–263] This VSFG mechanism is different from the widely studied case of planar air/water interfaces.[264]

Second, the VSFG microscope[265] (1.6 μm resolution) is necessary to probe single crystals, avoiding signals from randomly oriented crystals which, when ensemble averaged, cancel each other out.[265] The necessity of this effort is evident from the fact that only a single crystal of ZIF-90, having a diameter >10 μm, (sample A, Figure 5.2a,c), has a signal, while the aggregates of ZIF-90 nanocrystals (sample B, Figure 5.2b,c, and SI Figure 3) do not. In the following, we only focus on sample A and we also choose to study D_2O, instead of H_2O adsorption, to distinguish atmospheric H_2O adsorption by ZIF-90 during the sample transfer under dry conditions.[266–268]

As the RH is increased from 0% to 29% (Figure 5.3a starts from 23% for clarity, full range data in SI Figure 8), the overall nonresonant signal reduces. Similar signal reduction occurs when H_2O is adsorbed in this RH range (SI Figure 6). Combining the fact that at this RH range no resonant molecular feature appears and the adsorption isotherms show very limited water uptake, we attribute the intensity reduction to an increase in refractive indices upon adsorption of a small amount of water,[269] which leads to a decrease in the Fresnel coefficients and ultimate reduction in the second-order response of the hydrated MOF (description in SI S2).[270] This small water

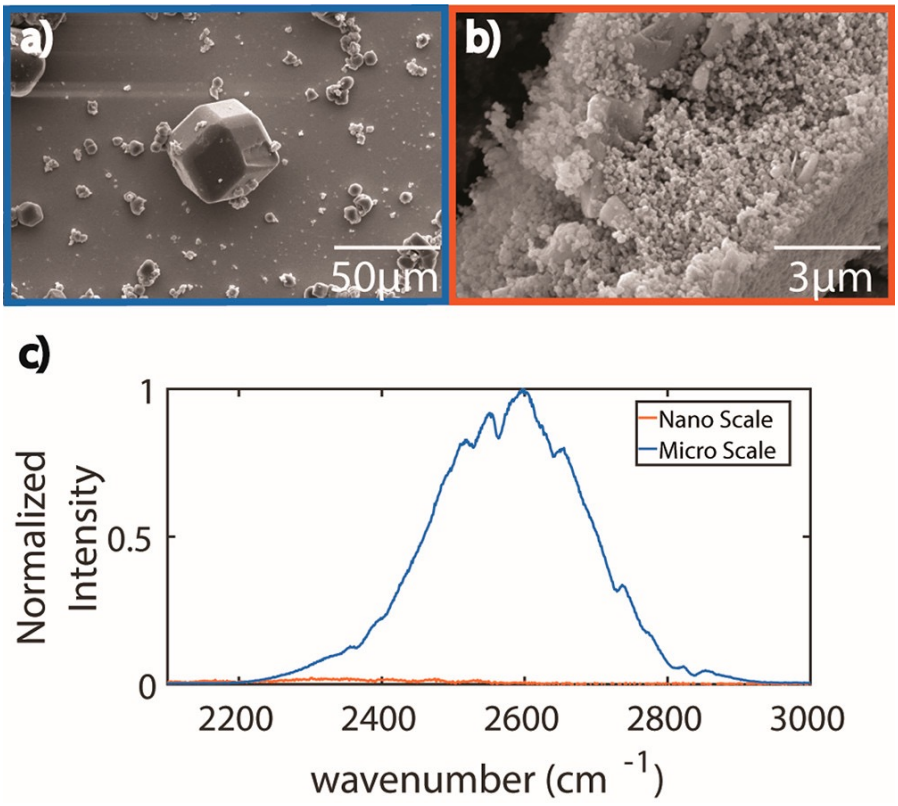

Figure 5.2: SEM images (a) micron-sized and (b) nanometer-sized ZIF-90 crystals. (c) The SFG signal is large for the micron-sized crystal but negligible for the nanocrystals.

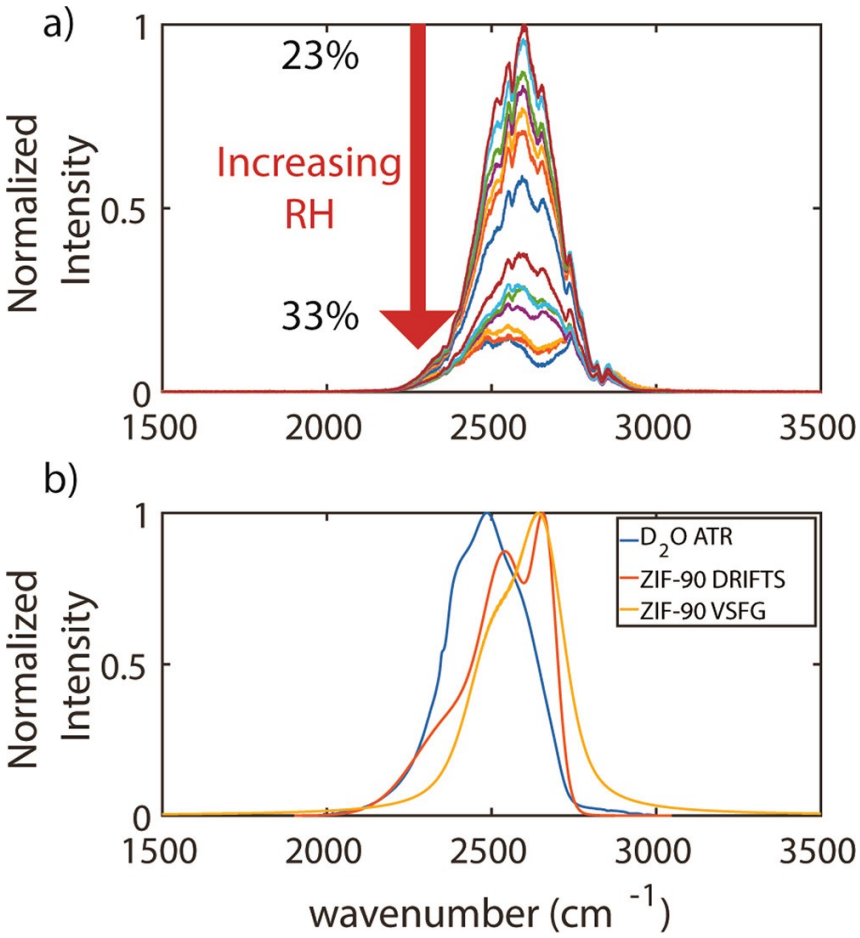

Figure 5.3: (a) Raw VSFG spectra from 23% to 33% RH and (b) an ATR spectrum of pure bulk D_2O, a DRIFTS spectrum at 43% RH, and an extracted VSFG spectra at 33%RH of D_2O adsorbed by ZIF-90. No VSFG line shape changes were observed above 33%.

adsorption prior to the major uptake is referred to as preadsorption.

As the RH increases, a dip near 2600 cm^{-1} becomes apparent at 31% RH (Figure 5.3a). This feature appears exclusively during D_2O (in contrast to H_2O) adsorption. Combined with its center frequency, it is assigned to the OD stretch of adsorbed D_2O on the ZIF-90 interior surface, due to the symmetry transfer from ZIF-90.[184,188,259,261,271] Other possible origins of this spectral change[272] were ruled out (SI Figure 5 and 6 for details).We extract the OD feature by treating the nonresonant signal as a local oscillator (see SI S4). Compared to bulk D_2O, OD features of both the bulk (DRIFTS) and interfacial (VSFG) D_2O in ZIF-90 exhibit blue shifts

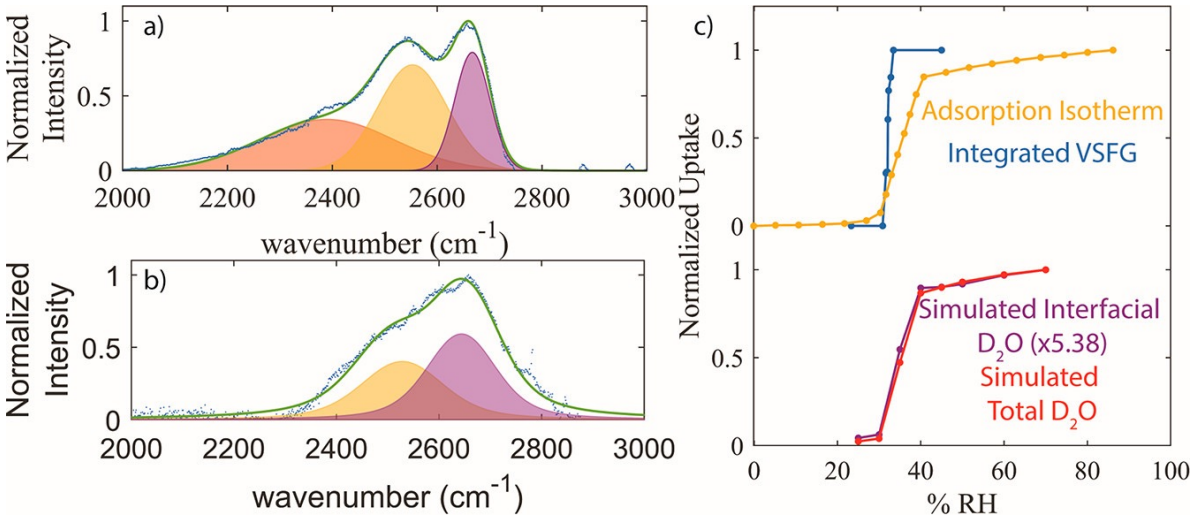

Figure 5.4: Fitting results for (a) DRIFTS and (b) VSFG at saturation. (c) Experimental integrated VSFG intensity (blue), adsorption isotherm (yellow), bound D_2O that contributes to the VSFG signal from simulation, N_{suf} (purple), and total simulated D_2O inside pore versus RH, N_{tot} (red). N_{suf} is calculated as the average number of water throughout the simulation that form a hydrogen bond to the carbonyl group of the framework (OW-o distance $\leq$3.5 Åand HW-OW-o angle $\leq$30°) for more than 400 fs, which is the coherent lifetime of the OD oscillation.

(Figure 5.3b), suggesting weaker hydrogen-bond interactions experienced by the D_2O molecules in ZIF-90, which is supported by our previous MD simulations.[240]

Spectral fittings show that the DRIFTS spectra have three peaks at 2400, 2550, and 2665 cm^{-1} (Figure 5.4a), while VSFG spectra have two peaks centered at ~2515 and 2630 cm^{-1} (Figure 5.4b). Besides the Fermi resonance at 2400 cm^{-1}, the 2550 and 2665 cm^{-1} peaks were assigned to the asymmetric and symmetric OD stretching modes.[240] The peak line shape difference between VSFG and DRIFTS spectra suggest that the VSFG signal is not a phantom signal due to liquid water absorption.[272]

Despite a small red shift between the DRIFTS and VSFG spectra (~35 cm^{-1}), the overall peak positions are similar, which is somewhat counterintuitive. As explained above, VSFG probes D_2O bound to the aldehyde groups at the step of water clustering, whereas DRIFTS probes all D_2O inside the pore, at both water clustering and pore filling steps (see SI S6 and SI Figure 13 for details). Based on MD simulations, if during the water cluster step D_2O is only bound to the

aldehyde groups of ZIF-90, its OD frequency should be $\sim$2720 cm^{-1}, significantly blue-shifted compared to D_2O in the bulk region of the pore ($\sim$2600 and 2660 cm^{-1}, SI Figure 14). This blue shift is observed because the hydrogen bonding between D_2O and aldehyde groups is weaker than that between D_2O molecules.[240] Thus, the similar spectral positions in the DRIFTS and VSFG spectra suggest that, instead of only binding to the organic linkers, D_2O molecules in the water clustering step experience a comparable local environment to the ones of pore filling steps.

A more unexpected result is that the RH dependence of the VSFG peak intensities closely follows the adsorption isotherm (Figure 5.4c). Since VSFG probes D_2O bound to the interior surfaces, the VSFG spectra are sensitive to the water clustering stages of D_2O uptake. In other words, the RH dependence of the VSFG signal suggests that the onset of water clustering and pore filling occur simultaneously. We note that the RH dependence of the DRIFTS intensity (SI Figure 10) differs drastically from that of the VSFG spectrum because DRIFTS intensity scales nonlinearly with the adsorbate concentration.[241–244]

MD simulations with the MB-pol model provide molecular-level insights into the underlying molecular mechanism of D_2O uptake by ZIF-90. At 30% RH, the simulations indicate that, instead of a uniform distribution across all pores, D_2O molecules localize into a single pore (Figure 5.5a).[248] Only at 40% RH do D_2O molecules nearly uniformly occupy all pores (Figure 5.5b). This result is robust against the initial distribution of D_2O molecules at every RH (SI S6 and SI Figures 15-17).

We further plot the number of D_2O molecules adsorbed at interior surfaces (N_{suf}), which can contribute to the VSFG signal, as well as the total number of adsorbed D_2O molecules (N_{tot}) as a function of RH (Figure 5.4c), to determine if water clustering and pore filling occur concurrently (mechanism 1) or sequentially (mechanism 2). Both N_{suf} and N_{tot} follow a similar trend and saturate at 40% when all pores are filled, agreeing with the RH dependence of the VSFG intensity and adsorption isotherm. This implies that water clustering and pore filling occur concurrently, with the D_2O molecules filling one pore after another, as in mechanism 1

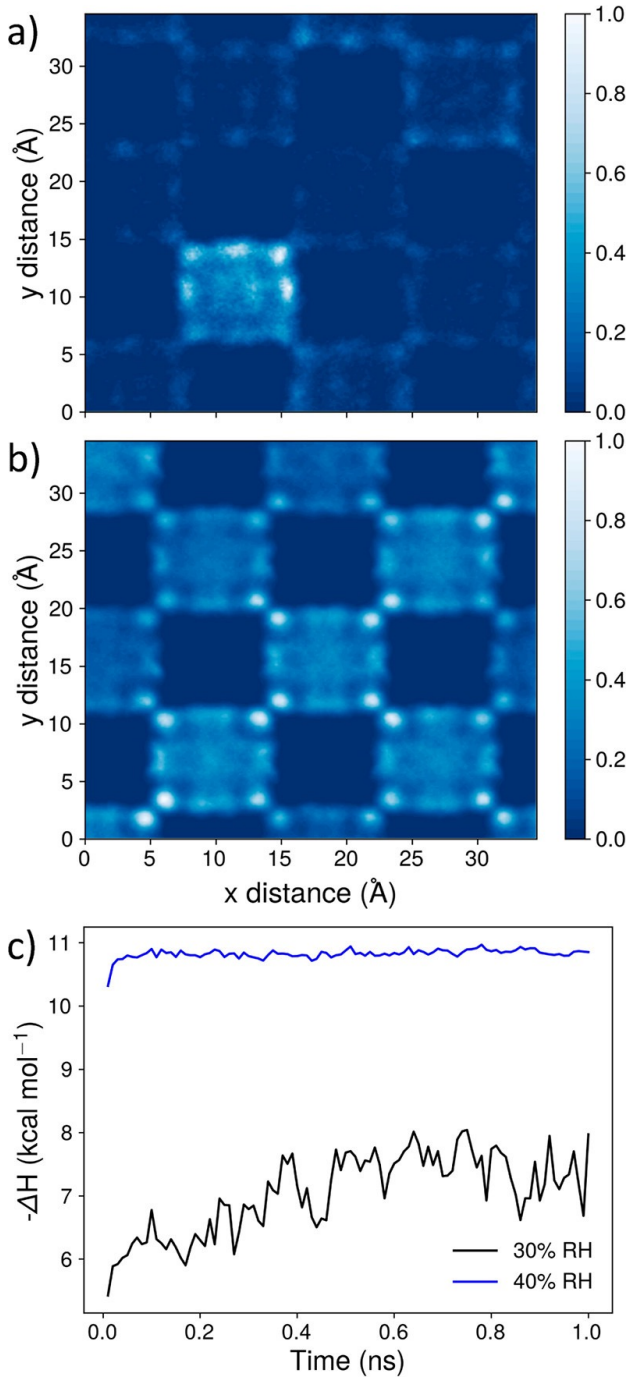

Figure 5.5: (a) At 30% RH, water preferentially clusters in single pores, and only the surface site on this specific unit cells are occupied, whereas (b) at 40% RH, water evenly distributes among pores with all surface sites occupied. (c) Enthalpy of adsorption at 30% RH (black) and 40% RH (blue). Each point represents an average over 10 ps of the simulation.

(Figure 5.1).

Our MD simulations further indicate that adsorption in a single pore is energetically favorable through the enthalpy of adsorption. At 30% RH, the enthalpy of adsorption is $\sim$2 kcal/mol lower at the beginning of the simulation when the D_2O molecules are uniformly distributed in the pores (Figure 5.5c and SI Figures 17 and 18). As the simulation progresses, the water molecules cluster into fewer pores, and the enthalpy of adsorption increases. Furthermore, the enthalpy of adsorption does not change throughout the simulation once all pores are filled at 40% RH (Figure 5.5c). This result is explained by considering that water–carbonyl interactions are weaker than water-water interactions in ZIF-90. It should be noted that, due to slower orientational dynamics, the entropy of the D_2O molecules in ZIF-90 is larger than in the bulk and decreases as the RH increases (SI Tables S3-S6).[273–276] At the very early stages of uptake, the entropic term thus drives D_2O molecules to the interior surface of a pore where they offer additional hydrogen-bonding sites. Due to stronger water–water interactions (i.e., larger enthalpic term) additional D_2O molecules prefer to form hydrogen bonds with the surface-bound D_2O molecules, instead of binding to aldehyde groups in other pores.

Since water clustering and pore filling occur simultaneously, it follows that, although VSFG detects D_2O involved in the clustering step, these molecules, at the same time, experience hydrogen-bonding interactions with other D_2O molecules in the pore, which explains why the positions of the D_2O peaks in the DRIFTS and VSFG spectra are similar. This conclusion is supported by the vibrational density of states calculated for bulk D_2O and D_2O adsorbed at the interior of the ZIF-90 pores (SI Figure 14).

For ZIF-90, water clustering and pore filling occur in single pores before other pores are filled, driven by initial entropic gains followed by increasing enthalpic contributions due to stronger water–water interactions than water–framework interactions. This mechanism is similar to the nucleation of water dispersed in a hydrophobic medium[277] and was also reported for the hydrophobic ZIF-8.[248] However, it is unexpected for ZIF-90, which is hydrophilic. Thus, this

work shows that when designing new MOFs for water harvesting, it is important to consider both entropic effects and the relative strength of the water-framework and water-water interactions, in addition to the hydrophilicity/hydrophobicity of the framework which is often considered as the main factor that determines water uptake. Molecular-level mechanisms of water uptake evolution in MOFs remain to be further explored to guide fine-tuning of these materials for better performance.[247] The integration of advanced spectroscopic techniques and computer simulations described here provide such a capability to better understand and optimize guest molecules-capturing mechanism for many host materials.

5.1 Associated Content

The Supporting Information is available free of charge at https://pubs.acs.org/doi/10.1021/jacs.1c09097.

Experimental methods, control and characterization experiments, DRIFTS and VSFG fitting methods and results, and simulation methods and additional results

5.2 Author Information

5.2.1 Author Contributions

The manuscript was written through contributions of all authors. All authors have given approval to the final version of the manuscript.

5.2.2 Funding

This work is supported by Department of Energy, Basic Energy Science (BES) Office, Condensed Phase and Interfacial Molecular Science (CPIMS) Program (Award No. DESC0019333). All simulations used resources of the National Energy Research Scientific Computing Center

(NERSC), supported by Department of Energy BES Office under contract DE-AC02-05CH11231. The VSFG microscope is developed under the support of National Science Foundation, Division of Chemistry, Major Research Instrumentation program (MRI), CHE-1828666. SEM imaging was done in part at San Diego Nanotechnology Infrastructure (SDNI) of UCSD, an NSF designated National Nanotechnology Coordinated Infrastructure site, supported by NSF grant ECCS-1542148.

5.2.3 Notes

The authors declare no competing financial interest.

5.3 Acknowledgments

We acknowledge Dr. Mark Kalaj from Dr. Seth Cohen's group for synthesizing ZIF-90 MOF.

Chapter 5, in full, is a reprint of the material as it appears in "Water Capture Mechanisms at Zeolitic Imidazolate Framework Interfaces", Wagner, J.C.; Hunter, K.M.; Paesani, F.; Xiong, W.; J. Am. Chem. Soc., 143, 50, 21189-21194, 2021. The dissertation author was the co-primary investigator and co-author of this paper.

Chapter 6

Molecular Mechanisms of Water Harvesting in the Ni_2X_2BTDD (X = F, Cl, Br) Metal-Organic Frameworks

Half a billion people face severe water scarcity year-round, and two-thirds of the world's population face severe water scarcity at least one month out of the year, making access to clean water one of the biggest issues facing the world today.[278] Lack of clean water can have severe impacts for humanity, such as decreased food production[279] and negative impacts on human health.[12,280] Because of the world's limited water supply, there exists an urgent need for newer methods and technologies that can obtain clean water. Desalination, which is a well-established method of water purification, requires large bodies of water such as rivers, lakes, and oceans as well as the subsequent transport of the purified water to more remote areas of land.[2,12,13] On the other hand, the atmosphere contains $\sim$10% of earth's freshwater[13] and is present across the planet. Atmospheric water capture is therefore not restricted to certain geographical regions since water can be harvested from the atmosphere anywhere in the world and does not face the challenge of transporting clean water to rural areas. Water harvesting also does not disrupt the hydrologic

cycle or utilize more limited water resources, such as rivers and lakes,[12,13] making atmospheric water capture a potential source of clean water across the globe.

In order to harvest water, materials that satisfy many working conditions are needed. The properties of an ideal water sorbent include low energy demand for water release, high water uptake, high cycling stability, and fast capture/release,[13] of which metal-organic frameworks (MOFs) fulfill many of these properties.[2] MOFs are a class of materials that contain a metal center in a secondary building unit (SBU) and an organic linker, which combine to form three-dimensional repeating structures that have large surface areas and high porosity.[34] Because of their large pores and various chemical properties, MOFs have applications in liquid and gas adsorption,[2,12,13,24,281] chemical separation,[9,11,25,27,282] catalysis,[16,21,283,284] and in numerous other areas.[34,285] The ability to tune MOF structures by varying the metal center or organic linker has allowed MOFs to be potential materials for water harvesting, and numerous MOFs have already been shown to be successful water sorbents.[2,13,41,44,159,203,205,238,247,286–291]

The MOF Ni_2X_2BTDD (X = F, Cl, Br) has recently emerged as one of the most promising materials for atmospheric water capture due to its record water uptake capacity at low relative humidity (RH) values.[44] The SBU of Ni_2X_2BTDD consists of open nickel (Ni^{2+}) metal centers bridged by the halides fluoride (F, Ni_2F_2BTDD), chloride (Cl, Ni_2Cl_2BTDD), or bromide (Br, Ni_2Br_2BTDD), and the organic linker bis(1H-1,2,3-triazolo[4,5-*b*],[4',5'-i])dibenzo[1,4]dioxin (H_2BTDD). Only the halide atoms (F, Cl, Br) are exchanged in each MOF, leaving the Ni^{2+} metal center and organic linker unchanged, yet the substitution of the halide atoms produces MOFs with various properties and water adsorption capacities. While the F and Cl MOFs have a pore diameter of 23 Å and can adsorb over 100% of their weight in water at 32% RH, the Br MOF has a pore dimater of 22 Å and can adsorb 64% of its weight in water below 25% RH, one of the best values reported to date.[44] Furthermore, the Cl MOF maintains 98% of its water uptake capacity after 400 cycles, and the Br MOF maintains its total water uptake capacity for more than 400 adsorption/desorption cycles.[44] However, the F MOF undergoes partial amorphization and

suffers a decline in its water adsorption capacity after one cycle.[44] From this data, it can be seen that the Ni_2Cl_2BTDD and Ni_2Br_2BTDD MOFs have a high water uptake capacity, high cycling stability, adsorb water over a narrow pressure and temperature range, and adsorb water reversibly, possessing many of the ideal properties for a water sorbent. It is therefore essential to obtain a molecular-level understanding of how halide subsitution in Ni_2X_2BTDD results in different water adsorption properties that benefit or hinder atmospheric water capture in these MOFs to aid in the design of future water harvesting MOFs.

One of the critical features in atmospheric water capture is understanding the water adsorption mechanism in MOFs, which has remained a challenge with only a few previous studies revealing the mechanisms of pore filling.[207,247,292] Disentangling the MOF–water and water–water interactions in various systems provides information on how water first adsorbs in the pore, interacting with the framework atoms, and then nucleates pore filling by forming hydrogen bonds (H-bonds) with additional water molecules. Although the first MOF–water interactions are important to initiate water adsorption at low RH values, these MOF–water interactions must not be too strong to prevent water desorption from the pore walls, a key property of water adsorbents.[13] It is therefore crucial to not only describe the process of pore filling in various MOFs, but it is imperative to understand how the interaction of water molecules with the framework atoms varies in a family of similar MOFs. By investigating the structural, dynamical, and thermodynamic properties of water in the Ni_2X_2BTDD MOF, the benefits of the Cl and Br MOFs along with the shortcomings of the F MOF can be understood.

In this study, we perform molecular dynamics (MD) simulations of water confined in the halide-substituted MOF Ni_2X_2BTDD (X = F, Cl, Br). After confirming that our force fields reproduce the experimental properties of water in each MOF, we demonstrate how the interaction strength of water with each MOF varies, with the F MOF having the strongest interactions. Water is shown to form strong H-bonds with the fluoride atom of the F MOF, but strong H-bonds are also formed with the nitrogen atoms in the Cl and Br MOFs. Because the strong interactions

between water and the F MOF lead to a decrease in the water uptake capacity after the first adsorption cycle,[44] the Cl and Br MOFs emerge as promising materials for atmospheric water capture. The Cl MOF, which has a larger pore volume than the Br MOF, adsorbs larger amounts of water, while the size of the pore in the Br MOF allows water to adsorb at a lower RH value, forming strong H-bonds with the nitrogen atom of the framework.

6.1 Results

6.1.1 Infrared spectra and experimental comparison

Infrared (IR) spectra reveal information about the H-bonding network of water confined in the Ni_2X_2BTDD MOFs, comparing the MOF–water and water–water interactions, and facilitate agreement with experiment to validate the MOF force fields and MD simulations. Fig. 6.1 shows a comparison of the simulated IR spectra with experiment for each MOF. At low loadings, distinct H-bonding environments exist that result in four features in the OH stretching region around $\sim$3700 cm^{-1}, $\sim$3500 cm^{-1}, $\sim$3300 cm^{-1}, and $\sim$3200 cm^{-1} in the experimental spectra. The highest frequency peak at 3700 cm^{-1} corresponds the free OH stretch, whereas the peaks at 3500 cm^{-1} and 3300 cm^{-1} can be attributed to H-bonded OH stretches. Furthermore, the lowest frequency peak at 3200 cm^{-1} is typically attributed to the Fermi resonance, or the coupling between the OH stretch fundamental and HOH bending overtone, which has been previously shown to be essential to the IR spectra of water clusters,[65,130] bulk water,[74] and confined water.[240] Adding the Fermi resonance contribution to the simulated IR spectra reproduces the experimental peak at the lowest frequency. As the water loading is increased, the distinct peaks then grow into one broad peak, indicating that the H-bonds are equivalent on the IR timescale (Supplementary Information Fig. S6). While small differences exist between the simulated and experimental IR spectra, the simulated spectra are able to reproduce the experimental features, ensuring accuracy of the MD simulations.

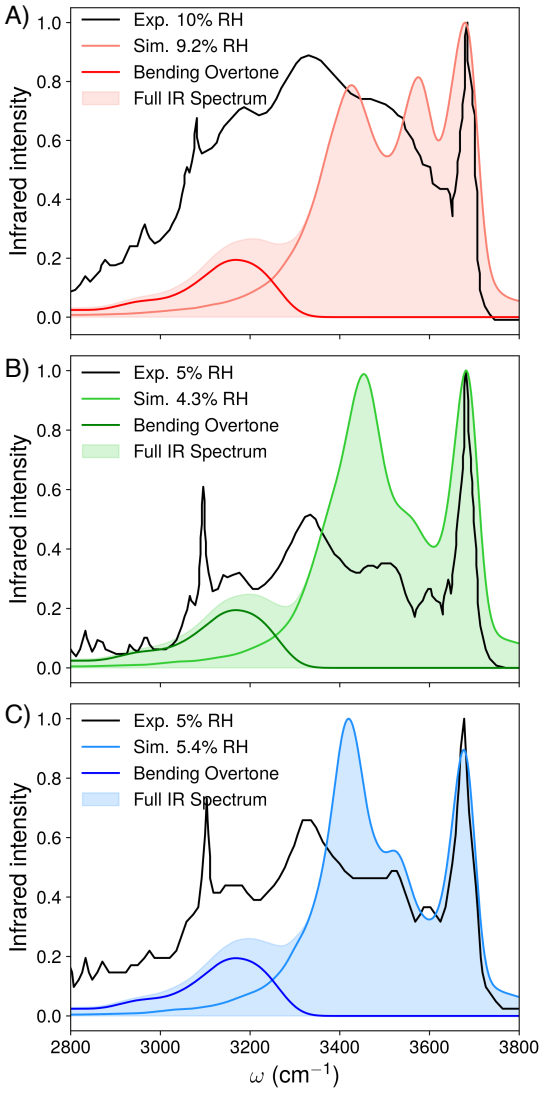

Figure 6.1: Theoretical and experimental infrared spectra of water in Ni_2X_2BTDD. A) Experimental IR spectra of water in the fluoride MOF at 10% RH from Ref. 44 (black), simulated 9.2% RH (2 H_2O/Ni^{2+}, pink), Fermi resonance contribution (red), and simulated 9.2% RH (2 H_2O/Ni^{2+}) with added Fermi resonance contribution (shaded pink). B) Experimental IR spectra of water in the chloride MOF at 5% RH from Ref. 44 (black), simulated 4.3% RH (1 H_2O/Ni^{2+}, light green), Fermi resonance contribution (green), and simulated 4.3% RH (1 H_2O/Ni^{2+}) with added Fermi resonance contribution (shaded green). C) Experimental IR spectra of water in the bromide MOF at 5% RH from Ref. 44 (black), simulated 5.4% RH (1 H_2O/Ni^{2+}, light blue), Fermi resonance contribution (blue), and simulated 5.4% RH (1 H_2O/Ni^{2+}) with added Fermi resonance contribution (shaded blue). All OH stretches are red-shifted by 215 cm^{-1} (F and Cl) or by 219 cm^{-1} (Br) to align with the experimental free OH stretch, HOH bending overtones are blue-shifted by 10 cm^{-1}, and all spectra are normalized to a value of one.

The IR spectra can be further decomposed by utilizing simulations of one and two water molecules in each MOF to observe the process of pore filling (Fig. 6.2). The first water molecule adsorbed in the pore interacts with the Ni^{2+} metal center (blue water molecules in Figs. 6.2A-C). This water molecule has two peaks in the IR spectra that are reminiscent of the symmetric and asymmetric stretches of water (Supplementary Information Fig. S7). The addition of a second water molecule (pink water molecules in Figs. 6.2A-C) initiates the formation of the H-bonding network, with the first water molecule donating a H-bond to the second water. The spectral features of these two water molecules can be broken down through the density of states (DOS) spectra (Figs. 6.2D-F). The first blue water molecule, which interacts with the Ni^{2+} metal center, exhibits a water–water H-bonded peak around $\sim$3450 cm^{-1} for all three MOFs in addition to a

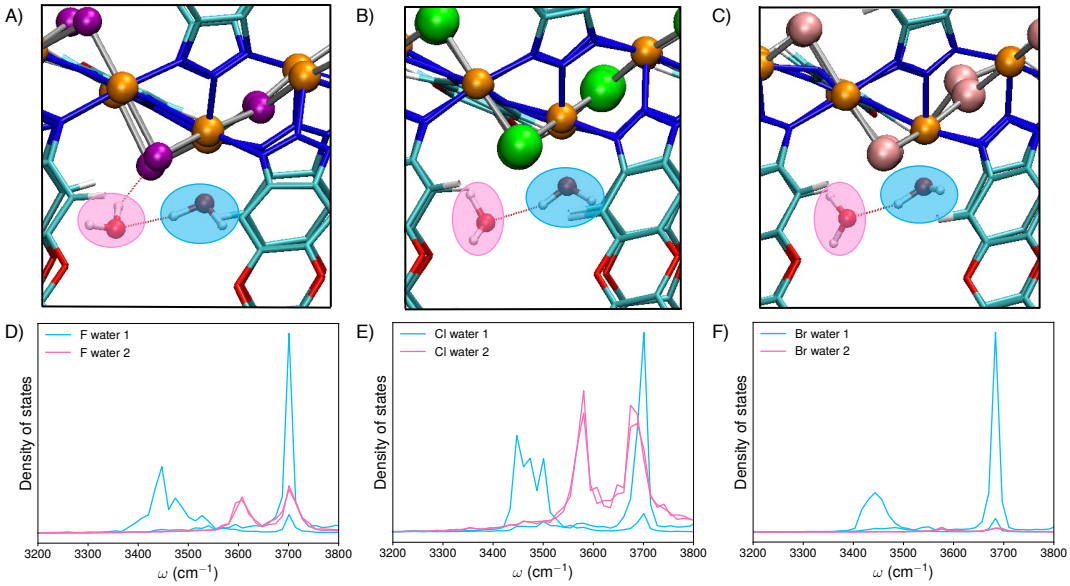

Figure 6.2: Density of states of two water molecules in Ni_2X_2BTDD. Snapshot of the MD simulation of two water molecules in the A) F MOF, B) Cl MOF, and C) Br MOF. The first water molecule interacting with the Ni^{2+} metal center in each MOF is highlighted in blue, and the second water molecule H-bonded to the first is highlighted in pink. Color scheme of atoms in panels A through C: Ni – orange, F – purple, Cl – green, Br – pink, N – blue, C – cyan, O – red, H – white. Hydrogen bonds are shown in dashed red lines. Density of states spectra of two water molecules in the D) F MOF, E) Cl MOF, and F) Br MOF. The colors of each peak correspond to the same colors of the water molecules in panels A through C. All OH stretches are red-shifted by 215 cm^{-1} (F and Cl) or by 219 cm^{-1} (Br).

free OH stretch, which does not donate a H-bond to another water molecule, at 3700 cm^{-1}. The second pink water molecule in each MOF exhibits a free OH stretch that points into the middle of the pore at 3700 cm^{-1} and has an additional feature around ∼3550-3600 cm^{-1}. While these two peaks can be reminiscent of the symmetric and asymmetric stretches of water, the lower frequency peak around ∼3550-3600 cm^{-1} is also caused by interactions with the MOF atoms. Water in the F MOF can form a H-bond with the F halide atom (Fig. 6.2A), whereas water in the Cl and Br MOFs can form a H-bond with the N atom of the MOF (Fig. 6.5C). The formation of these MOF–water H-bonds contribute to the spectral features around ∼3550-3600 cm^{-1}. Together with the Fermi resonance at 3200 cm^{-1}, these peaks correspond to the four main features in the experimental IR spectra at low RH values. Even with only two water molecules inside the MOF pores, a description of pore filling is beginning to unfold with the initial stage of the H-bonding network.

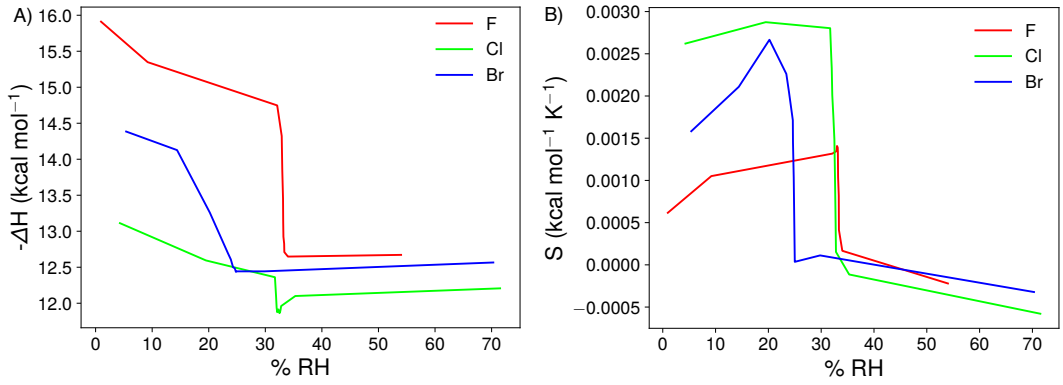

Figure 6.3: Enthalpy of adsorption and excess entropy for water in Ni_2X_2BTDD. A) Simulated enthalpy of adsorption for fluoride (red), chloride (green), and bromide (blue) as a function of RH. B) Simulated excess entropy compared to bulk water for fluoride (red), chloride (green), and bromide (blue) as a function of RH.

6.1.2 Thermodynamic information

The interactions of water molecules with the framework interface not only influence the adsorption process, but these interactions can have implications in the desorption process as well. The F MOF has the largest enthalpy of adsorption at all loadings; therefore, it has the strongest and most favorable interactions with water (Fig. 6.3A), while the chloride MOF has the lowest enthalpy of adsorption. As water fills the pores of each MOF (at 32% RH for F and Cl and 24% RH for Br), there is a decrease in the enthalpy of adsorption, suggesting that water has stronger interactions with the MOF than with other water molecules. It is important to note that the majority of energy adsorbed by the MOF (in the form of a change in temperature or an additional input of energy) is used to break the MOF–water interactions, which makes a lower enthalpy of adsorption more ideal for water desorption.[203] The large enthalpy of adsorption for the F MOF can therefore contribute to the partial amorphization and decline in water adsorption capacity in subsequent adsorption/desorption cycles.[44]

The trend for entropy is opposite that of the enthalpy of adsorption, where chloride has the largest entropy, and fluoride has the lowest entropy (Fig. 6.3B).[273–275] The first water molecules that fill the pores have an entropy larger than that of bulk water, which is due to the slower orientational dynamics resulting from the confining environment.[276,292] Similar to the enthalpy, there is a decrease in the entropy at the RH of pore filling because of the greater number of water molecules inside the pores. After the pores are filled, the entropy decreases below the value of bulk water, suggesting that it is energetically unfavorable for the MOFs to adsorb any further water molecules in the pores.

6.1.3 Structural information

The structure of water and H-bonding network in the various MOFs reveals further information for how water fills the pores and interacts with the framework atoms. When a single

water molecule is adsorbed in the F MOF, the spatial distribution of water is elongated across the F–Ni–F atoms, with water orienting toward the framework F atoms (Fig. 6.4A). Similarly, when a second water molecule is adsorbed in the pore, the spatial distribution of water remains elongated along the F–Ni–F atoms, even with the formation of a water–water H-bond (Supplementary Information Fig. S8). The spatial distribution of water in the Cl and Br MOFs, however, are different than in the F MOF (Fig. 6.4B and 6.4C for Cl and Br, respectively). In these MOFs, the distribution of water is more centralized around the Ni^{2+} metal center and not elongated toward the Cl or Br atoms.

Although water has similar interactions with the Ni^{2+} metal center in each MOF at low

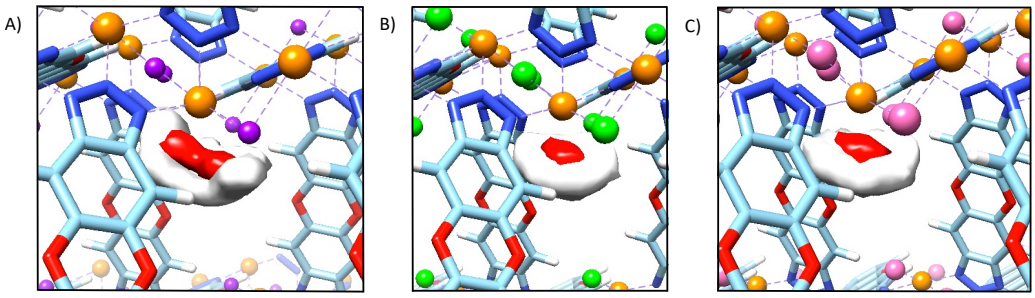

Figure 6.4: Spatial distribution of one water molecule in Ni_2X_2BTDD. One water molecule adsorbed in A) Ni_2F_2BTDD, B) Ni_2Cl_2BTDD, and C) Ni_2Br_2BTDD. Red isosurfaces correspond to water oxygen atoms, and white isosurfaces correspond to water hydrogen atoms. Color scheme of atoms in panels A through C: Ni – orange, F – purple, Cl – green, Br – pink, N – blue, C – cyan, O – red, H – white.

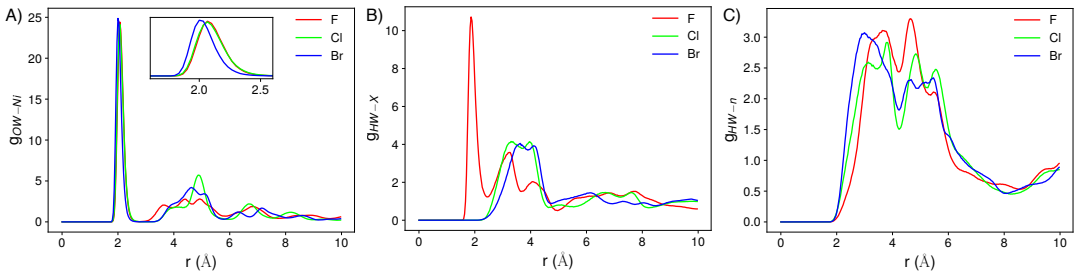

Figure 6.5: Radial distribution functions (RDFs) of water in Ni_2X_2BTDD. RDFs of Ni_2F_2BTDD (red), Ni_2Cl_2BTDD (green), and Ni_2Br_2BTDD (blue) MOFs at a loading of 1 H_2O/Ni^{2+} for A) OW–Ni (the first peak of the RDF is magnified in the inset), B) HW–X, and C) HW–n.

loadings (Fig. 6.5A), differences emerge in the H-bonding structure of water with the other framework atoms. The hydrogen atoms of water approach the F halide atom much closer than the other halides (Fig. 6.5B), suggesting the formation of a strong H_2O–F H-bond. These H-bonds at low RH reveal that water has favored interactions with the F atom and serve as an explanation for how the F MOF has the highest water adsorption capacity below $\sim$20% RH in the adsorption isotherm, before pore filling occurs in any MOF.[44] On the other hand, water molecules in the Cl and Br MOFs approach the MOF nitrogen (N) atoms at a closer distance, forming H_2O–N H-bonds with the framework. Even though the F, Cl, and Br atoms are all halogens, which have similar chemical properties, the presence of the N atom near the Ni^{2+} metal center causes differences for the structure of water filling the pore. Fluorine has the smallest atomic radius and largest electronegativity value among the four atoms (N, F, Cl, Br). Water is therefore attracted to the F atom due to the small atomic size and large electronegativity, forming strong H-bonds and leading to the large enthalpy of adsorption at all RH values (Fig. 6.3A). In comparing the N atom to the Cl and Br atoms, nitrogen and chlorine have similar electronegativity values, which are larger than bromine, but nitrogen has the smallest atomic radius. The smaller atomic radius of nitrogen allows water to approach the framework N atoms to a closer extent and thus form H-bonds with the N atoms compared to the Cl or Br atoms. The differences in these MOF–water interactions remain the same (and in fact become more pronounced for the H_2O–N H-bond) at the maximum water loading in each MOF (Supplementary Information Fig. S9).

At a loading of 1 H_2O/Ni^{2+} (Fig. 6.6A-C), the distribution of water in each MOF is similar to that of a single water molecule in Fig. 6.4. The distribution of water in the F MOF is elongated along the F–Ni–F atoms, adopting a circular geometry in the hexagonal pore, whereas water remains more localized around the Ni^{2+} metal centers in the Cl and Br MOFs. As the loading is increased to 3 H_2O/Ni^{2+} (Fig. 6.6D-F), greater differences in the water structure emerge in all the MOFs. The water molecules at different metal centers are beginning to connect to each other through the formation of bridging H-bonds, which is revealed by the increased water density

near the organic linkers. It is important to note here that a loading of 3 H_2O/Ni^{2+} corresponds to different RH values in all 3 MOFs due to the mass differences between the halide atoms. A loading of 3 H_2O/Ni^{2+} corresponds to 32.1% RH in Ni_2F_2BTDD, 31.7% RH in Ni_2Cl_2BTDD, and 20.2% RH in Ni_2Br_2BTDD. These RH values for F and Cl are at the step of water uptake in the adsorption isotherm, where water completely fills the pores. However, this RH value for Br is before pore saturation, which occurs at 24% RH. Therefore, while connected chains of water molecules bridging the various metal centers are beginning to appear at the water uptake step in F

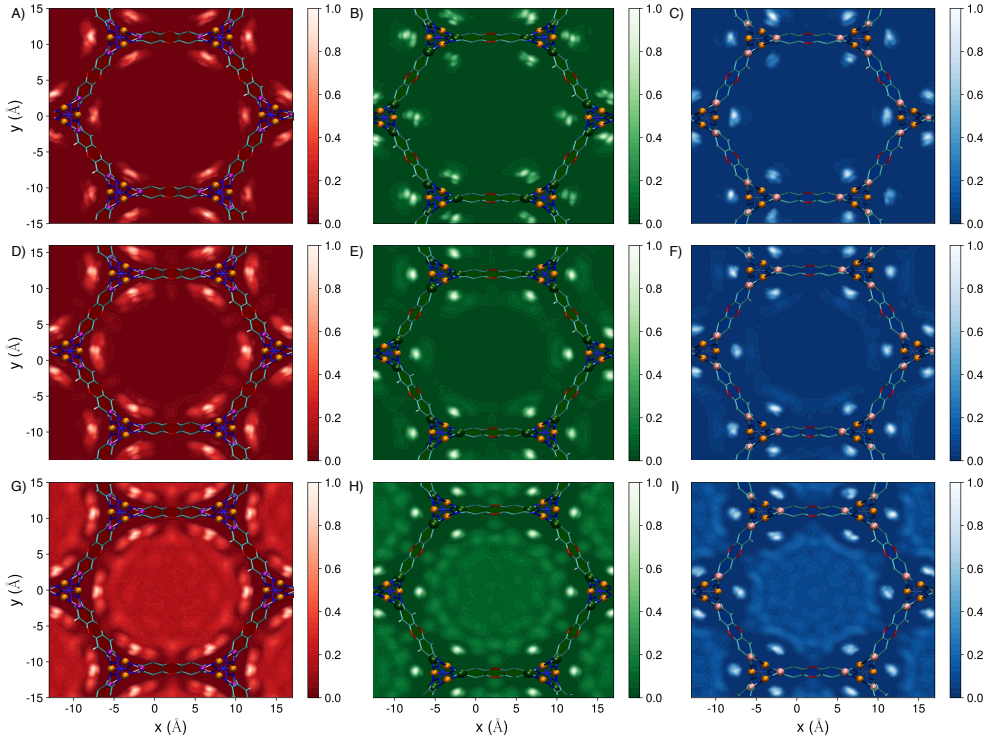

Figure 6.6: Two-dimensional density distribution of water in Ni_2X_2BTDD. Two-dimensional density distributions of water molecules in Ni_2F_2BTDD (A, D, and G red colors), Ni_2Cl_2BTDD (B, E, and H, green colors), and Ni_2Br_2BTDD (C, F, and I, blue colors). The top row represents the lowest water loading simulated for each MOF, 1 H_2O/Ni^{2+}: A) Ni_2F_2BTDD (0.96% RH), B) Ni_2Cl_2BTDD (4.3% RH), C) Ni_2Br_2BTDD (5.4% RH). The middle row represents a loading of 3 H_2O/Ni^{2+} for each MOF: D) Ni_2F_2BTDD (32.1% RH), E) Ni_2Cl_2BTDD (31.7% RH), F) Ni_2Br_2BTDD (20.2% RH). The bottom row represents the highest water loading simulated for each MOF: G) Ni_2F_2BTDD 12 H_2O/Ni^{2+} (54.0% RH), H) Ni_2Cl_2BTDD 13 H_2O/Ni^{2+} (71.5% RH), I) Ni_2Br_2BTDD 11 H_2O/Ni^{2+} (70.3% RH). Lighter colors correspond to regions of higher water density.

and Cl, these connected chains are forming before water adsorption occurs in Br. As described in Ref. 44, this is attributed to the larger atomic size of Br. Since the Br atom protrudes into the pore more than F or Cl, water also sticks out into the pore to a greater extent in the Br MOF. As the loading is increased, these waters protruding into the pore begin to form H-bonds with each other, coating the surface of the MOF in water molecules. These waters then nucleate the adsorption of more water molecules, causing the pore filling step to occur at the lower value of 24% RH in the Br MOF compared to 32% RH in the F and Cl MOFs.

At the maximum loading in each MOF (Fig. 6.6G-I), water adopts the same interactions with the framework interface as lower loadings but now completely fills the pores. Water can also bridge between different pores through the middle of the organic linker near the framework oxygen atoms. The F MOF adopts an overall circular geometry in the hexagonal pore due to the elongated interactions along the F–Ni–F atoms and formation of H-bonds with the F atoms. Water in the Cl MOF has the highest density next to the Ni^{2+} metal centers, which initiates the H-bonding network in the pore. While water in the Br MOF also has the highest density next to the Ni^{2+} metal centers, areas of little to no water density exist right next to these regions. These areas of low water density near the metal centers support the notion that the Br atoms protrude further into the pore than the other halide atoms, causing water to nucleate pore filling at a lower RH.

Even though water forms H-bonds with the framework atoms, the water molecules exhibit a various H-bonding topology with the different atoms in each MOF (Fig. 6.7), where a H-bond is defined as having an inter-atom distance ≤ 3.5 Å and an angle $\leq 30^{\circ}$. In the F MOF, a greater percent of water molecules donate and accept H-bonds from the framework F atom. On the other hand, water donates and accepts more H-bonds to the framework N atoms in both the Cl and Br MOFs. The timescales of these H_2O–X and H_2O–N H-bonds also differ, which provides a further viewpoint into the enthalpy of adsorption. The H-bond correlation function, a measure of the probability that a H-bond is intact after a specific amount of time,[293] reveals that water

has the longest H-bond lifetime in the Br MOF when interacting with the N atom (Table 6.1 and Supplementary Information Fig. S13). While water has a similar H-bond lifetime with the F atom in the F MOF and the N atom in the Cl MOF, this timescale is much longer with the N atom in the Br MOF. Because of the larger atomic size of Br compared to Cl, the water molecules may be pushed further away from the Br halide atom and towards the framework N atoms. The water molecules then spend a longer amount of time forming H-bonds with the N atom in the Br MOF, leading to a possible explanation of why the Br MOF has a larger enthalpy of adsorption than the Cl MOF. This data reveals that exchanging the halide atom in Ni_2X_2BTDD not only affects how water interacts with each respective halide atom, but varying the halide atom also affects how water interacts with the framework atoms that remain unchanged in each MOF.

6.2 Discussion

Exchanging the halide atoms in the Ni_2X_2BTDD MOF results in three MOFs with different properties and water adsorption capacities. The F and Cl MOFs adsorb over 100% of

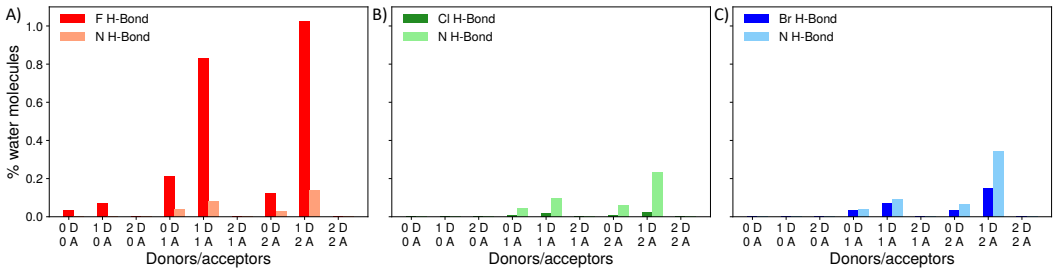

Figure 6.7: H-bonding topology of water in Ni_2X_2BTDD. H-bonding topology when water donates one H-bond to a MOF atom in A) Ni_2F_2BTDD, B) Ni_2Cl_2BTDD, and C) Ni_2Br_2BTDD. Darker colors represent the number of H-bond donors (D) and acceptors (A) when water forms a H-bond with a halide MOF atom (F, Cl, or Br). Lighter colors represent the number of H-bond donors (D) and acceptors (A) when water forms a H-bond with a nitrogen (N) MOF atom. The number of H-bond donors and acceptors are shown as a percent of the total number of water molecules confined in each MOF. The H-bonding topology is shown for the maximum loading of each system: 12 H_2O/Ni^{2+} for F, 13 H_2O/Ni^{2+} for Cl, and 11 H_2O/Ni^{2+} for Br. All axes are on the same scale.

Table 6.1: Relaxation time constants for the H-bond correlation function fit to the exponential $c(t)=Ae^{-t/\tau_2}$ after the 0.2 ps timescale of librations and inter-atom vibrations.[293]

H-bond (MOF)	τ_2 (ps)
H_2O–F (Ni_2F_2BTDD)	77.16
H_2O–N (Ni_2F_2BTDD)	20.44
H_2O–Cl (Ni_2Cl_2BTDD)	11.57
H_2O–N (Ni_2Cl_2BTDD)	77.86
H_2O–Br (Ni_2Br_2BTDD)	24.01
H_2O–N (Ni_2Br_2BTDD)	148.96

their weight in water at 32% RH, and the Br MOF adsorbs a record 64% of its weight in water below 25% RH, one of the best water uptake values reported to date.[44] Furthermore, the Cl and Br MOFs retain most of their water uptake capacities after hundreds of adsorption/desorption cycles. Even though the F MOF is not suitable for atmospheric water capture since it undergoes partial amorphization and a decline in its water uptake capacity after the first adsorption cycle,[44] it is important to understand these MOF–water interactions so that future MOFs do not undergo the same challenges in water adsorption. It is also essential to understand the MOF–water interactions in both the Cl and Br MOFs to disentangle which interactions lead to lower enthalpies of adsorption and pore filling at lower RH values.

Utilizing MD simulations, we have shown that our molecular models achieve agreement with the experimental properties of water in the IR spectra. The DOS spectra decompose the IR lineshape, attributing the main spectral peaks at low RH values to free OH stretches, MOF–water H-bonds, water–water H-bonds, and Fermi resonances; at higher water loadings, multiple H-bonding environments exist that resemble bulk water. The thermodynamic properties of water in Ni_2X_2BTDD begin to reveal the differences that exist among the three MOFs. All three MOFs have larger enthalpies of adsorption at low RH values compared to high RH values, suggesting that there are stronger MOF–water interactions than water–water interactions. This is important to take note of because the MOF–water interactions must be overcome in order to desorb water from the MOF pores. Furthermore, the F MOF has the largest enthalpy of adsorption at all water

loadings; water orients itself along the F–Ni–F atoms and forms a strong H-bond with the F atom of the MOF at all loadings. This molecular-level description of water in the F MOF enables an understanding of why the F MOF undergoes partial amorphization and has a decline in its water uptake capacity after the first adsorption cycle, with water forming the strongest interactions with the F MOF.

On the other hand, the Cl and Br MOFs have the potential to be successful water sorbents. The water adsorption capacity is greater in the Cl MOF than the Br MOF because of the smaller atomic size of Cl, resulting in a larger pore space. After interacting with the Ni^{2+} metal center, water molecules prefer to interact with the N atoms of the framework, forming H_2O–N H-bonds. The Cl MOF also has the lowest enthalpy of adsorption, suggesting that this MOF might need the lowest energy input to desorb water. Due to the large atomic size of Br, the water molecules in the Br MOF protrude into the pore to the greatest extent. This allows water molecules at various Ni^{2+} metal centers to connect to each other, initiating the H-bonding network with fewer water molecules and leading to pore filling at the lowest RH compared to F and Cl. Additionally, water has the longest H-bond lifetime when forming a H-bond with the N framework atom in the Br MOF, leading to the intermediate enthalpy of adsorption for Br.

This in-depth view into the structure, dynamics, and thermodynamics of water confined in Ni_2X_2BTDD has revealed a detailed description of the properties of water in a family of MOFs. Substituting the halide atoms of the MOF affects not only how water interacts with the halide atom, but it affects how water interacts with all the MOF atoms. While water prefers to interact with the F atom in the F MOF, water has the strongest interactions with the N atoms in the Cl and Br MOFs. These differences in the water structure and the subsequent effect on the H-bonding network affect the cycling stability, RH of pore filling, and total water uptake of each MOF, which are all important features for water sorbents. By understanding the behavior of water confined in various MOFs, future water harvesting MOFs can be designed that can adsorb large amounts of water while retaining their stability to provide a source of clean drinking water to all areas of the

world.

6.3 Methods

6.3.1 Force fields and potential energy functions

Each MOF structure was first optimized using periodic density functional theory (DFT) calculations carried out with the Vienna Ab initio Simulation Package (VASP),[216–219] using the PBE exchange-correlation functional[220] with Grimme's D3 dispersion correction[221] in combination with a projector-augmented wave (PAW) treatment[222,223] with a 700 eV kinetic energy cutoff. A $2 \times 2 \times 4$ k-point grid was used, and forces were converged to a tolerance of 0.05 eV/Å. Following periodic optimization, a cluster surrounding the Ni^{2+} metal center was extracted for each MOF (see Supporting Information for details). All bonded parameters involving the Ni^{2+} metal center were fit using a genetic algorithm, and all bonded parameters for the organic linker were taken from the General Amber Force Field (GAFF).[81] Atomic point charges were calculated for the clusters using the charge model 5 (CM5) charge scheme.[91] The Lennard-Jones (LJ) parameters were taken from the Universal Force Field (UFF)[82] for the Ni, F, Cl, and Br atoms, and the LJ parameters for the organic linker atoms (H, C, N, O) were taken from GAFF.[81] Force field parameters are given in Supplementary Tables S1-S15.

The many-body potential energy function MB-pol was used to simulate water.[60–62] MB-pol has been shown to correctly predict the properties of water from the gas to the condensed phase for structural, thermodynamic, and dynamical properties.[63] The many-body dipole moment (MB-μ) was used to calculate the dipole moment of water for the IR spectra.[71] Local mode and local monomer (LM) calculations[57,122,123] from Ref. 74 were utilized to add the Fermi resonance contribution to the IR spectra.

Nonbonded interactions between water and the MOF were represented through electrostatic and Van der Waals (VDW) interactions. The Ni–OW, X–OW (X = F, Cl, Br), and X–HW

interactions were fit to a Buckingham potential using a genetic algorithm (see Supplementary Information for details). Cross interactions between water and the remaining MOF atoms were described through Lennard-Jones (LJ) parameters. The LJ parameters were derived from Lorentz–Berthelot mixing rules using the LJ parameters of the TIP4P/2005 water model,[226] which is the closest point-charge model to MB-pol.[137]

6.3.2 Molecular dynamics simulations

Classical molecular dynamics (MD) simulations were performed using an in-house code based on the DL_POLY_2 simulation package,[176] which was modified to include MB-pol water.[60–62] Simulations for each halide MOF were carried out for a system containing $1 \times 1 \times 3$ unit cells under periodic boundary conditions. The initial configurations for each MD simulation of the different halide MOFs were generated from Packmol.[175] Each configuration started with 54 water molecules (1 H_2O/Ni^{2+}), and an additional 54 water molecules were added to each subsequent simulation (+1 H_2O/Ni^{2+}) up to the point of pore saturation on the adsorption isotherm (12 H_2O/Ni^{2+} for Ni_2F_2BTDD, 13 H_2O/Ni^{2+} for Ni_2Cl_2BTDD, and 11 H_2O/Ni^{2+} for Ni_2Br_2BTDD).[44] MD simulations were first performed utilizing a constant number of molecules, pressure, and temperature in the NPT isobaric–isothermal ensemble. The system was heated to 1000 K for 10 ps at 1.0 atm, cooled to 500 K for 20 ps at 1.0 atm, and cooled to 300 K for 20 ps at 1.0 atm, all in the NPT ensemble, to randomize the initial distribution of water molecules. MD simulations were then performed for 1 ns at 300 K and 1.0 atm in the NPT ensemble to equilibrate the system, calculate structural information, and obtain the average box dimensions. Average box dimensions are listed in Supplementary Tables S16-S18 and were used for all subsequent simulations at each loading. The angles of each simulation box were 90°, 90°, and 120° along the x, y, and z dimensions, respectively. Following the initial equilibration, the system was simulated with a constant number of molecules, volume, and temperature in the NVT canonical ensemble for 100 ps at 300 K followed by a constant number of molecules, volume, and energy in the NVE

microcanonical ensemble for 50 ps to obtain dynamical information, including the IR spectra, where the temperature remained constant around 300 K. Subsequent configurations were heated to 1000 K for 10 ps in the NVT ensemble to randomize the distribution of water, cooled to 300 K for 10 ps in the NVT ensemble, and then run for 50 ps in the NVE ensemble where the temperature remained constant around 300 K. 19 of these additional trajectories were run at each loading for each halide, giving a total of 20 independent MD simulations in which all dynamical properties were averaged over.

All MD simulations were performed with a time step of 0.2 fs, and the equations of motion were propagated according to the velocity-Verlet algorithm. The temperature was maintained at 300 K by a Nosé-Hoover chain of four thermostats.[177] Short-range interactions were truncated at an atom–atom distance of 9.0 Å, and the electrostatics were calculated using the Ewald sum.[80]

Chapter 6, in full, is a reprint of the material as it is being prepared for publication in "Molecular Mechanisms of Water Harvesting in the Ni_2X_2BTDD (X = F, Cl, Br) Metal-Organic Frameworks", Hunter, K.M.; Paesani, F. The dissertation author is the primary investigator and author of this paper.

Chapter 7

Conclusions

Water is one of the most essential molecules to life, yet a majority of the world's population do not have access to clean water. Not only are new sources of water essential, but safe drinking water is needed in all areas of the world, especially the hottest and driest parts of the planet. Therefore, there is an urgent need for new methods of obtaining clean drinking water. Atmospheric water capture is one of the most promising methods of obtaining safe water, and MOFs have been shown to be able to adsorb large amounts of water at low relative humidity, which are critical features for water harvesting. However, a more detailed understanding of atmospheric water capture is needed to provide a clearer picture of the properties that can enhance water adsorption. It is thus essential to have a molecular-level understanding of water in various environments to develop future materials that can contribute to atmospheric water capture.

Various water solutions were first investigated to obtain a complete understanding of the properties of bulk water. The four isotopic solutions neat H_2O, diluted HOD in H_2O, diluted H_2O in D_2O, and diluted HOD in D_2O solutions provided different levels of intermolecular and intramolecular coupling to isolate the various components of the OH stretching region of bulk water. Intermolecular coupling between water molecules revealed the partially quantum mechanical nature of hydrogen bonds in water, whereas intramolecular coupling helped decompose the

importance of the bending overtone within the OH stretching region. Explicit calculation of the Fermi resonance contribution in water provided an increase in the IR intensity around $\sim$3250 cm^{-1}, resulting in quantitative agreement with experiment and allowing this feature in the IR spectra to be attributed to the Fermi resonance.

Having an understanding of bulk water, water confined in MOFs can be studied. It was found that water fills the pores of the Co_2Cl_2BTDD MOF in a deliberate manner. Water first interacts with the hydrophilic sites of the MOF, which contain open metal sites, and subsequently forms one-dimensional hydrogen bonded chains along the interior of the pore surface. These water molecules have distinct environments that result in various dynamical properties, which then nucleate pore filling. Furthermore, there is a structural and dynamical heterogeneity in the interior of the MOF, with water displaying distinct properties as a function of distance from the pore surface. Water near the MOF interface has the slowest dynamics, due to the presence of the MOF, whereas water in the center of the pore resembles bulk water, displaying dynamical properties similar to that of bulk water.

Building on previous studies of water in MOFs, the interactions between water and the framework along with a detailed description of pore filling was investigated for water confined in ZIF-90. It was shown that the use of quantum centroid molecular dynamics (CMD) simulations and the addition of the Fermi resonance, similar to the study done in bulk water, was essential to capture the presence of nuclear quantum effects in confined water and achieve agreement with experimental IR spectra. It was also demonstrated how modifications to existing force fields may be required to correctly reproduce the structure and dynamics of water confined in MOFs. By modifying the Lennard-Jones interactions between water and the carbonyl group of the MOF, which was the primary adsorption site for water in ZIF-90, quantitative agreement with experiment was obtained. This study provided the key detail that varying the interactions between various force fields may be an essential step in performing accurate simulations of water confined in MOFs.

The use of experimental vibrational sum-frequency generation spectroscopy (VSFG), a new technique to study water confined in MOFs, further disentangled the contributions of interfacial water vs. bulk-like water in ZIF-90. In combination with molecular dynamics simulations, these methods discertained the mechanism of pore filling for water. Water was shown to fill one pore at a time, first forming clusters that nucleate pore filling, as opposed to filling all pores simultaneously. Similar techniques can be used to understand the pore filling mechanism for water in various MOFs.

When studying the Ni_2X_2BTDD (X = F, Cl, Br) MOF, even though only the halide atoms are exchanged, the pore filling process and structure of water are different in each MOF. The F MOF has the greatest water adsorption at the lowest RH values, which is attributed to the strong interactions of water with the framework atoms and the formation of hydrogen bonds with the F atoms in the MOF. Water conversely forms strong hydrogen bonds with the N atoms of the Cl and Br MOFs. Furthermore, water completely fills the pores of the Br MOF at 24% RH, the lowest value of all three MOFs. This phenomenon is caused by the large Br atoms protruding into the pore, which enable the water molecules at separate Ni metal centers to form hydrogen bonds with each other that then nucleate pore filling at a lower RH.

This body of work has shown how small variations in MOFs, through exchanging specific atoms or modifying the interactions between water and the framework, can change the properties of water confined in various MOFs. The combination of theory and experiment has been able to shed light on these processes, disentangling the mechanism of pore filling in distinct MOFs and studying the hydrogen bonding network of confined water. The use of accurate models for both water and MOFs have revealed key features in the pore filling mechanisms of water capture that are critical to the design of future water harvesting materials. Water is essential to the world, and the process of atmospheric water capture holds much promise in delivering a source of clean drinking water to the world.

Bibliography

[1] Luigi De Marco, Krupa Ramasesha, and Andrei Tokmakoff. Experimental evidence of fermi resonances in isotopically dilute water from ultrafast broadband ir spectroscopy. *J. Phys. Chem. B*, 117(49):15319–15327, 2013.

[2] Nikita Hanikel, Mathieu S Prévot, and Omar M Yaghi. MOF water harvesters. *Nat. Nanotechnol.*, 15(5):348–355, 2020.

[3] UNICEF. Water security for all, 2021.

[4] Jay R Werber, Chinedum O Osuji, and Menachem Elimelech. Materials for next-generation desalination and water purification membranes. *Nat. Rev. Mater.*, 1(5):1–15, 2016.

[5] Muhammad Qasim, Mohamed Badrelzaman, Noora N Darwish, Naif A Darwish, and Nidal Hilal. Reverse osmosis desalination: A state-of-the-art review. *Desalination*, 459:59–104, 2019.

[6] Haya Nassrullah, Shaheen Fatima Anis, Raed Hashaikeh, and Nidal Hilal. Energy for desalination: A state-of-the-art review. *Desalination*, 491:114569, 2020.

[7] Yu Jie Lim, Kunli Goh, Masaru Kurihara, and Rong Wang. Seawater desalination by reverse osmosis: Current development and future challenges in membrane fabrication–a review. *J. Membr. Sci.*, 629:119292, 2021.

[8] Grégorio Crini and Eric Lichtfouse. Advantages and disadvantages of techniques used for wastewater treatment. *Environ. Chem. Lett.*, 17(1):145–155, 2019.

[9] Sara Rojas and Patricia Horcajada. Metal–organic frameworks for the removal of emerging organic contaminants in water. *Chem. Rev.*, 120(16):8378–8415, 2020.

[10] Elorm Obotey Ezugbe and Sudesh Rathilal. Membrane technologies in wastewater treatment: A review. *Membranes*, 10(5):89, 2020.

[11] Juan Li, Hou Wang, Xingzhong Yuan, Jingjing Zhang, and Jia Wei Chew. Metal-organic framework membranes for wastewater treatment and water regeneration. *Coord. Chem. Rev.*, 404:213116, 2020.

[12] Yaodong Tu, Ruzhu Wang, Yannan Zhang, and Jiayun Wang. Progress and expectation of atmospheric water harvesting. *Joule*, 2(8):1452–1475, 2018.

[13] Xingyi Zhou, Hengyi Lu, Fei Zhao, and Guihua Yu. Atmospheric water harvesting: A review of material and structural designs. *ACS Mater. Lett.*, 2(7):671–684, 2020.

[14] Jay R Werber, Akshay Deshmukh, and Menachem Elimelech. The critical need for increased selectivity not increased water permeability for desalination membranes. *Environ. Sci. Technol. Lett.*, 3(4):112–120, 2016.

[15] Hiroyasu Furukawa, Felipe Gandara, Yue-Biao Zhang, Juncong Jiang, Wendy L Queen, Matthew R Hudson, and Omar M Yaghi. Water adsorption in porous metal–organic frameworks and related materials. *J. Am. Chem. Soc.*, 136(11):4369–4381, 2014.

[16] Dandan Li, Hai-Qun Xu, Long Jiao, and Hai-Long Jiang. Metal-organic frameworks for catalysis: State of the art challenges and opportunities. *EnergyChem*, 1(1):100005, 2019.

[17] Qi Wang and Didier Astruc. State of the art and prospects in metal–organic framework (MOF)-based and MOF-derived nanocatalysis. *Chem. Rev.*, 120(2):1438–1511, 2019.

[18] Hannelore Konnerth, Babasaheb M Matsagar, Season S Chen, Martin HG Prechtl, Fa-Kuen Shieh, and Kevin C-W Wu. Metal-organic framework (MOF)-derived catalysts for fine chemical production. *Coord. Chem. Rev.*, 416:213319, 2020.

[19] Chunyan Du, Zhuo Zhang, Guanlong Yu, Haipeng Wu, Hong Chen, Lu Zhou, Yin Zhang, Yihai Su, Shiyang Tan, Lu Yang, Jiahao Song, and Shitao Wang. A review of metal organic framework (MOFs)-based materials for antibiotics removal via adsorption and photocatalysis. *Chemosphere*, 272:129501, 2021.

[20] Maryum Ali, Erum Pervaiz, Tayyaba Noor, Osama Rabi, Rubab Zahra, and Minghui Yang. Recent advancements in MOF-based catalysts for applications in electrochemical and photoelectrochemical water splitting: A review. *Int. J. Energy Res.*, 45(2):1190–1226, 2021.

[21] Meicheng Wen, Guiying Li, Hongli Liu, Jiangyao Chen, Taicheng An, and Hiromi Yamashita. Metal–organic framework-based nanomaterials for adsorption and photocatalytic degradation of gaseous pollutants: Recent progress and challenges. *Environ. Sci. Nano*, 6(4):1006–1025, 2019.

[22] Barbara Szczęśniak, Jerzy Choma, and Mietek Jaroniec. Gas adsorption properties of hybrid graphene-MOF materials. *J. Colloid Interface Sci.*, 514:801–813, 2018.

[23] Taravat Ghanbari, Faisal Abnisa, and Wan Mohd Ashri Wan Daud. A review on production of metal organic frameworks (MOF) for co_2 adsorption. *Sci. Total. Environ.*, 707:135090, 2020.

[24] Sachin P Shet, S Shanmuga Priya, K Sudhakar, and Muhammad Tahir. A review on current trends in potential use of metal-organic framework for hydrogen storage. *Int. J. Hydrogen Energy*, 46(21):11782–11803, 2021.

[25] Xin Li, Yuxin Liu, Jing Wang, Jorge Gascon, Jiansheng Li, and Bart Van der Bruggen. Metal–organic frameworks based membranes for liquid separation. *Chem. Soc. Rev.*, 46(23):7124–7144, 2017.

[26] Qihui Qian, Patrick A Asinger, Moon Joo Lee, Gang Han, Katherine Mizrahi Rodriguez, Sharon Lin, Francesco M Benedetti, Albert X Wu, Won Seok Chi, and Zachary P Smith. MOF-based membranes for gas separations. *Chem. Rev.*, 120(16):8161–8266, 2020.

[27] Rebecca L Siegelman, Eugene J Kim, and Jeffrey R Long. Porous materials for carbon dioxide separations. *Nat. Mater.*, 20(8):1060–1072, 2021.

[28] Nagy L Torad, Yunqi Li, Shinsuke Ishihara, Katsuhiko Ariga, Yuichiro Kamachi, Hong-Yuan Lian, Hicham Hamoudi, Yoshio Sakka, Watcharop Chaikittisilp, Kevin C-W Wu, and Yusuke Yamauchi. MOF-derived nanoporous carbon as intracellular drug delivery carriers. *Chem. Lett.*, 43(5):717–719, 2014.

[29] Jian Cao, Xuejiao Li, and Hongqi Tian. Metal-organic framework (MOF)-based drug delivery. *Curr. Med. Chem.*, 27(35):5949–5969, 2020.

[30] Harrison D Lawson, S Patrick Walton, and Christina Chan. Metal–organic frameworks for drug delivery: A design perspective. *ACS applied materials & interfaces*, 13(6):7004–7020, 2021.

[31] Vitalie Stavila, A Alec Talin, and Mark D Allendorf. MOF-based electronic and opto-electronic devices. *Chem. Soc. Rev.*, 43(16):5994–6010, 2014.

[32] Weiwei Zhao, Jiali Peng, Weikang Wang, Shujuan Liu, Qiang Zhao, and Wei Huang. Ultrathin two-dimensional metal-organic framework nanosheets for functional electronic devices. *Coord. Chem. Rev.*, 377:44–63, 2018.

[33] Xiaohui Ren, Gengcheng Liao, Zhongjun Li, Hui Qiao, Yuan Zhang, Xiang Yu, Bing Wang, Hui Tan, Li Shi, Xiang Qi, and Han Zhang. Two-dimensional MOF and COF nanosheets for next-generation optoelectronic applications. *Coord. Chem. Rev.*, 435:213781, 2021.

[34] Hiroyasu Furukawa, Kyle E Cordova, Michael O'Keeffe, and Omar M Yaghi. The chemistry and applications of metal-organic frameworks. *Science*, 341(6149), 2013.

[35] Franck Millange and Richard I Walton. MIL-53 and its isoreticular analogues: A review of the chemistry and structure of a prototypical flexible metal-organic framework. *Isr. J. Chem.*, 58(9-10):1019–1035, 2018.

[36] Meizhen Gao, Jing Wang, Zhenghao Rong, Qi Shi, and Jinxiang Dong. A combined experimental-computational investigation on water adsorption in various ZIFs with the sod and rho topologies. *RSC Adv.*, 8(69):39627–39634, 2018.

[37] Mason C Lawrence and Michael J Katz. Analysis of the water adsorption isotherms in uio-based metal–organic frameworks. *J. Phys. Chem. C*, 126(2):1107–1114, 2021.

[38] Jérôme Canivet, Alexandra Fateeva, Youmin Guo, Benoit Coasne, and David Farrusseng. Water adsorption in MOFs: Fundamentals and applications. *Chem. Soc. Rev.*, 43(16):5594–5617, 2014.

[39] Nicholas C Burtch, Himanshu Jasuja, and Krista S Walton. Water stability and adsorption in metal–organic frameworks. *Chem. Rev.*, 114(20):10575–10612, 2014.

[40] Xinlei Liu, Xuerui Wang, and Freek Kapteijn. Water and metal–organic frameworks: From interaction toward utilization. *Chem. Rev.*, 120(16):8303–8377, 2020.

[41] Adam J Rieth, Sungwoo Yang, Evelyn N Wang, and Mircea Dincă. Record atmospheric fresh water capture and heat transfer with a material operating at the water uptake reversibility limit. *ACS Central Sci.*, 3(6):668–672, 2017.

[42] Omar K Farha, Ibrahim Eryazici, Nak Cheon Jeong, Brad G Hauser, Christopher E Wilmer, Amy A Sarjeant, Randall Q Snurr, SonBinh T Nguyen, A Özgür Yazaydın, and Joseph T Hupp. Metal–organic framework materials with ultrahigh surface areas: Is the sky the limit? *J. Am. Chem. Soc.*, 134(36):15016–15021, 2012.

[43] Sofia Calero and P Gómez-Álvarez. Underlying adsorption mechanisms of water in hydrophobic and hydrophilic zeolite imidazolate frameworks: ZIF-71 and ZIF-90. *J. Phys. Chem. C*, 119(41):23774–23780, 2015.

[44] Adam J Rieth, Ashley M Wright, Grigorii Skorupskii, Jenna L Mancuso, Christopher H Hendon, and Mircea Dincă. Record-setting sorbents for reversible water uptake by systematic anion exchanges in metal–organic frameworks. *J. Am. Chem. Soc.*, 141(35):13858–13866, 2019.

[45] Anders Nilsson and Lars GM Pettersson. The structural origin of anomalous properties of liquid water. *Nat. Commun.*, 6(1):1–11, 2015.

[46] K Liu, JD Cruzan, and RJ Saykally. Water clusters. *Science*, 271(5251):929–933, 1996.

[47] Ralf Ludwig. Water: From clusters to the bulk. *Angew. Chem. Int. Ed.*, 40(10):1808–1827, 2001.

[48] William H Robertson, Eric G Diken, Erica A Price, Joong-Won Shin, and Mark A Johnson. Spectroscopic determination of the oh- solvation shell in the OH-·(H_2O) n clusters. *Science*, 299(5611):1367–1372, 2003.

[49] Jeffrey M Headrick, Eric G Diken, Richard S Walters, Nathan I Hammer, Richard A Christie, Jun Cui, Evgeniy M Myshakin, Michael A Duncan, Mark A Johnson, and Kenneth D Jordan. Spectral signatures of hydrated proton vibrations in water clusters. *Science*, 308(5729):1765–1769, 2005.

[50] Francesco Paesani and Gregory A. Voth. the properties of water: Insights from quantum simulations. *J. Phys. Chem. B*, 113(17):5702–5719, 2009.

[51] B.M. Auer and J.L. Skinner. Water: Hydrogen bonding and vibrational spectroscopy in the bulk liquid and at the liquid/vapor interface. *Chem. Phys. Lett.*, 470(1):13 – 20, 2009.

[52] Robert Bukowski, Krzysztof Szalewicz, Gerrit C. Groenenboom, and Ad van der Avoird. Predictions of the properties of water from first principles. *Science*, 315(5816):1249–1252, 2007.

[53] Robert Bukowski, Krzysztof Szalewicz, Gerrit C. Groenenboom, and Ad van der Avoird. Polarizable interaction potential for water from coupled cluster calculations. i. analysis of dimer potential energy surface. *J. Chem. Phys.*, 128(9):094313, 2008.

[54] Robert Bukowski, Krzysztof Szalewicz, Gerrit C. Groenenboom, and Ad van der Avoird. Polarizable interaction potential for water from coupled cluster calculations. ii. applications to dimer spectra virial coefficients and simulations of liquid water. *J. Chem. Phys.*, 128(9):094314, 2008.

[55] Yimin Wang, Benjamin C. Shepler, Bastiaan J. Braams, and Joel M. Bowman. Full-dimensional ab initio potential energy and dipole moment surfaces for water. *J. Chem. Phys.*, 131(5):054511, 2009.

[56] Yimin Wang, Xinchuan Huang, Benjamin C. Shepler, Bastiaan J. Braams, and Joel M. Bowman. Flexible ab initio potential and dipole moment surfaces for water. i. tests and applications for clusters up to the 22-mer. *J. Chem. Phys.*, 134(9):094509, 2011.

[57] Yimin Wang and Joel M. Bowman. Ab initio potential and dipole moment surfaces for water. ii. local-monomer calculations of the infrared spectra of water clusters. *J. Chem. Phys.*, 134(15):154510, 2011.

[58] Volodymyr Babin, Gregory R. Medders, and Francesco Paesani. Toward a universal water model: First principles simulations from the dimer to the liquid phase. *J. Phys. Chem. Lett.*, 3(24):3765–3769, 2012.

[59] Gregory R. Medders, Volodymyr Babin, and Francesco Paesani. a critical assessment of two-body and three-body interactions in water. *J. Chem. Theory Comput.*, 9(2):1103–1114, 2013.

[60] Volodymyr Babin, Claude Leforestier, and Francesco Paesani. Development of a "first principles" water potential with flexible monomers: Dimer potential energy surface vrt spectrum and second virial coefficient. *J. Chem. Theory Comput.*, 9(12):5395–5403, 2013.

[61] Volodymyr Babin, Gregory R Medders, and Francesco Paesani. Development of a "first principles" water potential with flexible monomers. ii: Trimer potential energy surface third virial coefficient and small clusters. *J. Chem. Theory Comput.*, 10(4):1599–1607, 2014.

[62] Gregory R Medders, Volodymyr Babin, and Francesco Paesani. Development of a "first-principles" water potential with flexible monomers. iii. liquid phase properties. *J. Chem. Theory Comput.*, 10(8):2906–2910, 2014.

[63] Sandeep K Reddy, Shelby C Straight, Pushp Bajaj, C Huy Pham, Marc Riera, Daniel R Moberg, Miguel A Morales, Chris Knight, Andreas W Götz, and Francesco Paesani. On the accuracy of the mb-pol many-body potential for water: Interaction energies vibrational frequencies and classical thermodynamic and dynamical properties from clusters to liquid water and ice. *J. Chem. Phys.*, 145(19):194504, 2016.

[64] Jeremy O Richardson, Cristóbal Pérez, Simon Lobsiger, Adam A Reid, Berhane Temelso, George C Shields, Zbigniew Kisiel, David J Wales, Brooks H Pate, and Stuart C Althorpe. Concerted hydrogen-bond breaking by quantum tunneling in the water hexamer prism. *Science*, 351(6279):1310–1313, 2016.

[65] Sandra E. Brown, Andreas W. Götz, Xiaolu Cheng, Ryan P. Steele, Vladimir A. Mandelshtam, and Francesco Paesani. Monitoring water clusters "melt" through vibrational spectroscopy. *J. Am. Chem. Soc.*, 139(20):7082–7088, 2017.

[66] C. Huy Pham, Sandeep K. Reddy, Karl Chen, Chris Knight, and Francesco Paesani. Many-body interactions in ice. *J. Chem. Theory Comput.*, 13(4):1778–1784, 2017.

[67] Zhaoru Sun, Lixin Zheng, Mohan Chen, Michael L Klein, Francesco Paesani, and Xifan Wu. Electron-hole theory of the effect of quantum nuclei on the x-ray absorption spectra of liquid water. *Phys. Rev. Lett.*, 121(13):137401, 2018.

[68] Alex. P Gaiduk, Tuan Anh Pham, Marco Govoni, Francesco Paesani, and Giulia Galli. Electron affinity of liquid water. *Nat. Commun.*, 9:247, 2018.

[69] William T. S. Cole, James D. Farrell, David J. Wales, and Richard J. Saykally. Structure and torsional dynamics of the water octamer from thz laser spectroscopy near 215 μm. *Science*, 352(6290):1194–1197, 2016.

[70] Nagaprasad Reddy Samala and Noam Agmon. Temperature dependence of intramolecular vibrational bands in small water clusters. *J. Phys. Chem. B*, 123(44):9428–9442, 2019.

[71] Gregory R. Medders and Francesco Paesani. Infrared and raman spectroscopy of liquid water through "first-principles" many-body molecular dynamics. *J. Chem. Theory Comput.*, 11(3):1145–1154, 2015.

[72] Shelby C. Straight and Francesco Paesani. Exploring electrostatic effects on the hydrogen bond network of liquid water through many-body molecular dynamics. *J. Phys. Chem. B*, 120(33):8539–8546, 2016.

[73] Sandeep K. Reddy, Daniel R. Moberg, Shelby C. Straight, and Francesco Paesani. Temperature-dependent vibrational spectra and structure of liquid water from classical

and quantum simulations with the mb-pol potential energy function. *J. Chem. Phys.*, 147(24):244504, 2017.

[74] Kelly M Hunter, Farnaz A Shakib, and Francesco Paesani. Disentangling coupling effects in the infrared spectra of liquid water. *J. Phys. Chem. B*, 122(47):10754–10761, 2018.

[75] Gregory R Medders and Francesco Paesani. Dissecting the molecular structure of the air/water interface from quantum simulations of the sum-frequency generation spectrum. *J. Am. Chem. Soc.*, 138(11):3912–3919, 2016.

[76] Daniel R. Moberg, Shelby C. Straight, and Francesco Paesani. Temperature dependence of the air/water interface revealed by polarization sensitive sum-frequency generation spectroscopy. *J. Phys. Chem. B*, 122(15):4356–4365, 2018.

[77] Daniel R. Moberg, Shelby C. Straight, Christopher Knight, and Francesco Paesani. Molecular origin of the vibrational structure of ice ih. *J. Phys. Chem. Lett.*, 8(12):2579–2583, 2017.

[78] Daniel R Moberg, Peter J Sharp, and Francesco Paesani. Molecular-level interpretation of vibrational spectra of ordered ice phases. *J. Phys. Chem. B*, 122(46):10572–10581, 2018.

[79] Daniel R Moberg, Daniel Becker, Christoph W Dierking, Florian Zurheide, Bernhard Bandow, Udo Buck, Arpa Hudait, Valeria Molinero, Francesco Paesani, and Thomas Zeuch. The end of ice i. *Proc. Natl. Acad. Sci. U.S.A.*, 116(49):24413–24419, 2019.

[80] Andrew R Leach. *Molecular Modelling: Principles and Applications*. Pearson Education Limited, Essex, U.K., 2nd ed. edition, 2001.

[81] Junmei Wang, Romain M Wolf, James W Caldwell, Peter A Kollman, and David A Case. Development and testing of a general amber force field. *J. Comput. Chem.*, 25(9):1157–1174, 2004.

[82] Anthony K Rappé, Carla J Casewit, KS Colwell, William A Goddard III, and W Mason Skiff. Uff a full periodic table force field for molecular mechanics and molecular dynamics simulations. *J. Am. Chem. Soc.*, 114(25):10024–10035, 1992.

[83] Louis Vanduyfhuys, Steven Vandenbrande, Toon Verstraelen, Rochus Schmid, Michel Waroquier, and Veronique Van Speybroeck. Quickff: A program for a quick and easy derivation of force fields for metal-organic frameworks from ab initio input. *J. Comput. Chem.*, 36(13):1015–1027, 2015.

[84] Matthew A Addicoat, Nina Vankova, Ismot Farjana Akter, and Thomas Heine. Extension of the universal force field to metal–organic frameworks. *J. Chem. Theory Comput.*, 10(2):880–891, 2014.

[85] Sareeya Bureekaew, Saeed Amirjalayer, Maxim Tafipolsky, Christian Spickermann, Tapta Kanchan Roy, and Rochus Schmid. MOF-FF–a flexible first-principles derived force field for metal-organic frameworks. *Phys. Status Solidi B*, 250(6):1128–1141, 2013.

[86] Damien E Coupry, Matthew A Addicoat, and Thomas Heine. Extension of the universal force field for metal–organic frameworks. *J. Chem. Theory Comput.*, 12(10):5215–5225, 2016.

[87] Tingting Weng and JR Schmidt. Flexible and transferable ab initio force field for zeolitic imidazolate frameworks: ZIF-FF. *J. Phys. Chem. A*, 123(13):3000–3012, 2019.

[88] Zachary L Terranova and Francesco Paesani. The effects of framework dynamics on the behavior of water adsorbed in the [zn (l-l)(cl)] and co-MOF-74 metal–organic frameworks. *Phys. Chem. Chem. Phys.*, 18(11):8196–8204, 2016.

[89] Jordi Cirera, Jeffrey C Sung, Porter B Howland, and Francesco Paesani. The effects of electronic polarization on water adsorption in metal-organic frameworks: H_2O in MIL-53 (cr). *J. Chem. Phys.*, 137(5):054704, 2012.

[90] Thomas A Manz and David S Sholl. Improved atoms-in-molecule charge partitioning functional for simultaneously reproducing the electrostatic potential and chemical states in periodic and nonperiodic materials. *J. Chem. Theory Comput.*, 8(8):2844–2867, 2012.

[91] Aleksandr V Marenich, Steven V Jerome, Christopher J Cramer, and Donald G Truhlar. Charge model 5: An extension of hirshfeld population analysis for the accurate description of molecular interactions in gaseous and condensed phases. *J. Chem. Theory Comput.*, 8(2):527–541, 2012.

[92] Rossend Rey, Klaus B. Møller, and James T. Hynes. Ultrafast vibrational population dynamics of water and related systems: A theoretical perspective. *Chem. Rev.*, 104(4):1915–1928, 2004.

[93] H. J. Bakker and J. L. Skinner. Vibrational spectroscopy as a probe of structure and dynamics in liquid water. *Chem. Rev.*, 110(3):1498–1517, 2010.

[94] Fivos Perakis, Luigi De Marco, Andrey Shalit, Fujie Tang, Zachary R. Kann, Thomas D. Kühne, Renato Torre, Mischa Bonn, and Yuki Nagata. Vibrational spectroscopy and dynamics of water. *Chem. Rev.*, 116(13):7590–7607, 2016.

[95] John E. Bertie and Zhida Lan. Infrared intensities of liquids xx: The intensity of the oh stretching band of liquid water revisited and the best current values of the optical constants of H_2O(l) at 25°c between 15000 and 1 cm^{-1}. *Appl. Spectrosc.*, 50(8):1047–1057, 1996.

[96] C. J. Fecko, J. D. Eaves, J. J. Loparo, A. Tokmakoff, and P. L. Geissler. Ultrafast hydrogen-bond dynamics in the infrared spectroscopy of water. *Science*, 301(5640):1698–1702, 2003.

[97] Christopher J. Fecko, Joseph J. Loparo, Sean T. Roberts, and Andrei Tokmakoff. Local hydrogen bonding dynamics and collective reorganization in water: Ultrafast infrared spectroscopy of HOD/D_2O. *J. Chem. Phys.*, 122(5):054506, 2005.

[98] John B. Asbury, Tobias Steinel, C. Stromberg, S. A. Corcelli, C. P. Lawrence, J. L. Skinner, and M. D. Fayer. Water dynamics: Vibrational echo correlation spectroscopy and comparison to molecular dynamics simulations. *J. Phys. Chem. A*, 108(7):1107–1119, 2004.

[99] Joseph J. Loparo, Sean T. Roberts, Rebecca A. Nicodemus, and Andrei Tokmakoff. Variation of the transition dipole moment across the oh stretching band of water. *Chem. Phys.*, 341(1):218 – 229, 2007.

[100] Rebecca A. Nicodemus, S. A. Corcelli, J. L. Skinner, and Andrei Tokmakoff. Collective hydrogen bond reorganization in water studied with temperature-dependent ultrafast infrared spectroscopy. *J. Phys. Chem. B*, 115(18):5604–5616, 2011.

[101] Krupa Ramasesha, Luigi De Marco, Aritra Mandal, and Andrei Tokmakoff. Water vibrations have strongly mixed intra- and intermolecular character. *Nat. Chem.*, 5:935–940, 2013.

[102] Luigi De Marco, Krupa Ramasesha, and Andrei Tokmakoff. Experimental evidence of fermi resonances in isotopically dilute water from ultrafast broadband ir spectroscopy. *J. Phys. Chem. B*, 117(49):15319–15327, 2013.

[103] Luigi De Marco, William Carpenter, Hanchao Liu, Rajib Biswas, Joel M. Bowman, and Andrei Tokmakoff. Differences in the vibrational dynamics of H_2O and D_2O: Observation of symmetric and antisymmetric stretching vibrations in heavy water. *J. Phys. Chem. Lett.*, 7(10):1769–1774, 2016.

[104] Rossend Rey, Klaus B. Møller, and James T. Hynes. Hydrogen bond dynamics in water and ultrafast infrared spectroscopy. *J. Phys. Chem. A*, 106(50):11993–11996, 2002.

[105] C. P. Lawrence and J. L. Skinner. Vibrational spectroscopy of hod in liquid D_2O. i. vibrational energy relaxation. *J. Chem. Phys.*, 117(12):5827–5838, 2002.

[106] C. P. Lawrence and J. L. Skinner. Vibrational spectroscopy of hod in liquid D_2O. ii. infrared line shapes and vibrational stokes shift. *J. Chem. Phys.*, 117(19):8847–8854, 2002.

[107] C. P. Lawrence and J. L. Skinner. Vibrational spectroscopy of hod in liquid D_2O. iii. spectral diffusion and hydrogen-bonding and rotational dynamics. *J. Chem. Phys.*, 118(1):264–272, 2003.

[108] C. P. Lawrence and J. L. Skinner. Vibrational spectroscopy of hod in liquid D_2O. vi. intramolecular and intermolecular vibrational energy flow. *J. Chem. Phys.*, 119(3):1623–1633, 2003.

[109] Klaus B. Møller, Rossend Rey, and James T. Hynes. Hydrogen bond dynamics in water and ultrafast infrared spectroscopy: A theoretical study. *J. Phys. Chem. A*, 108(7):1275–1289, 2004.

[110] S. A. Corcelli, C. P. Lawrence, and J. L. Skinner. Combined electronic structure/molecular dynamics approach for ultrafast infrared spectroscopy of dilute HOD in liquid H_2O and D_2O. *J. Chem. Phys.*, 120(17):8107–8117, 2004.

[111] S. A. Corcelli and J. L. Skinner. Infrared and raman line shapes of dilute HOD in liquid H_2O and D_2O from 10 to 90 °c. *J. Phys. Chem. A*, 109(28):6154–6165, 2005.

[112] B. M. Auer and J. L. Skinner. Ir and raman spectra of liquid water: Theory and interpretation. *J. Chem. Phys.*, 128(22):224511, 2008.

[113] Francesco Paesani, Sotiris S. Xantheas, and Gregory A. Voth. Infrared spectroscopy and hydrogen-bond dynamics of liquid water from centroid molecular dynamics with an ab initio-based force field. *J. Phys. Chem. B*, 113(39):13118–13130, 2009.

[114] Mino Yang and J. L. Skinner. Signatures of coherent vibrational energy transfer in ir and raman line shapes for liquid water. *Phys. Chem. Chem. Phys.*, 12:982–991, 2010.

[115] L. Shi, S. M. Gruenbaum, and J. L. Skinner. Interpretation of ir and raman line shapes for H_2O and D_2O ice ih. *J. Phys. Chem. B*, 116(47):13821–13830, 2012.

[116] Yimin Wang and Joel M. Bowman. Ir spectra of the water hexamer: Theory with inclusion of the monomer bend overtone and experiment are in agreement. *J. Phys. Chem. Lett.*, 4(7):1104–1108, 2013.

[117] Yicun Ni and J. L. Skinner. Ir and sfg vibrational spectroscopy of the water bend in the bulk liquid and at the liquid-vapor interface respectively. *J. Chem. Phys.*, 143(1):014502, 2015.

[118] Hanchao Liu, Yimin Wang, and Joel M. Bowman. Quantum calculations of the ir spectrum of liquid water using ab initio and model potential and dipole moment surfaces and comparison with experiment. *J. Chem. Phys.*, 142(19):194502, 2015.

[119] Gregory R. Medders and Francesco Paesani. on the interplay of the potential energy and dipole moment surfaces in controlling the infrared activity of liquid water. *J. Chem. Phys.*, 142(21):212411, 2015.

[120] Hanchao Liu, Yimin Wang, and Joel M. Bowman. Transferable ab initio dipole moment for water: Three applications to bulk water. *J. Phys. Chem. B*, 120(8):1735–1742, 2016.

[121] Gregory R. Medders and Francesco Paesani. Many-body convergence of the electrostatic properties of water. *J. Chem. Theory Comput.*, 9(11):4844–4852, 2013.

[122] Xiaolu Cheng and Ryan P. Steele. Efficient anharmonic vibrational spectroscopy for large molecules using local-mode coordinates. *J. Chem. Phys.*, 141(10):104105, 2014.

[123] Xiaolu Cheng, Justin J. Talbot, and Ryan P. Steele. Tuning vibrational mode localization with frequency windowing. *J. Chem. Phys.*, 145(12):124112, 2016.

[124] Jianshu Cao and Gregory A Voth. The formulation of quantum statistical mechanics based on the feynman path centroid density. i. equilibrium properties. *J. Chem. Phys.*, 100(7):5093–5105, 1994.

[125] Jianshu Cao and Gregory A Voth. The formulation of quantum statistical mechanics based on the feynman path centroid density. ii. dynamical properties. *J. Chem. Phys.*, 100(7):5106–5117, 1994.

[126] Jianshu Cao and Gregory A Voth. The formulation of quantum statistical mechanics based on the feynman path centroid density. iii. phase space formalism and analysis of centroid molecular dynamics. *J. Chem. Phys.*, 101(7):6157–6167, 1994.

[127] Jianshu Cao and Gregory A Voth. The formulation of quantum statistical mechanics based on the feynman path centroid density. iv. algorithms for centroid molecular dynamics. *J. Chem. Phys.*, 101(7):6168–6183, 1994.

[128] Jianshu Cao and Gregory A Voth. The formulation of quantum statistical mechanics based on the feynman path centroid density. v. quantum instantaneous normal mode theory of liquids. *J. Chem. Phys.*, 101(7):6184–6192, 1994.

[129] Tyler D. Hone, Peter J. Rossky, and Gregory A. Voth. a comparative study of imaginary time path integral based methods for quantum dynamics. *J. Chem. Phys.*, 124(15):154103, 2006.

[130] Alexei A. Kananenka and J. L. Skinner. Fermi resonance in oh-stretch vibrational spectroscopy of liquid water and the water hexamer. *J. Chem. Phys.*, 148(24):244107, 2018.

[131] Frank Neese. the orca program system. *WIREs Comput. Mol. Sci.*, 2(1):73–78, 2012.

[132] J. Towns, T. Cockerill, M. Dahan, I. Foster, K. Gaither, A. Grimshaw, V. Hazlewood, S. Lathrop, D. Lifka, G. D. Peterson, R. Roskies, J. R. Scott, and N. Wilkins-Diehr. Xsede: Accelerating scientific discovery. *Comput. Sci. Eng.*, 16(5):62–74, Sept 2014.

[133] Joel G Davis, Kamil P Gierszal, Ping Wang, and Dor Ben-Amotz. Water structural transformation at molecular hydrophobic interfaces. *Nature*, 491(7425):582–585, 2012.

[134] Kenichiro Koga, GT Gao, Hideki Tanaka, and Xiao Cheng Zeng. Formation of ordered ice nanotubes inside carbon nanotubes. *Nature*, 412(6849):802–805, 2001.

[135] Urszula Kosinska Eriksson, Gerhard Fischer, Rosmarie Friemann, Giray Enkavi, Emad Tajkhorshid, and Richard Neutze. Subangstrom resolution x-ray structure details aquaporin-water interactions. *Science*, 340(6138):1346–1349, 2013.

[136] Michael D Fayer and Nancy E Levinger. Analysis of water in confined geometries and at interfaces. *Annu. Rev. Anal. Chem.*, 3:89–107, 2010.

[137] Arpa Hudait, Daniel R Moberg, Yuqing Qiu, Nathan Odendahl, Francesco Paesani, and Valeria Molinero. Preordering of water is not needed for ice recognition by hyperactive antifreeze proteins. *Proc. National Acad. Sci.*, 115(33):8266–8271, 2018.

[138] Alexei Kiselev, Felix Bachmann, Philipp Pedevilla, Stephen J Cox, Angelos Michaelides, Dagmar Gerthsen, and Thomas Leisner. Active sites in heterogeneous ice nucleation—the example of k-rich feldspars. *Science*, 355(6323):367–371, 2017.

[139] Yuqing Qiu, Nathan Odendahl, Arpa Hudait, Ryan Mason, Allan K Bertram, Francesco Paesani, Paul J DeMott, and Valeria Molinero. Ice nucleation efficiency of hydroxylated organic surfaces is controlled by their structural fluctuations and mismatch to ice. *J. Am. Chem. Soc.*, 139(8):3052–3064, 2017.

[140] Laura Fumagalli, Ali Esfandiar, Rene Fabregas, Sheng Hu, Pablo Ares, Amritha Janardanan, Qian Yang, Boya Radha, Takashi Taniguchi, Kenji Watanabe, Gabriel Gomila, Kostya S. Novoselov, and Andre K. Geim. Anomalously low dielectric constant of confined water. *Science*, 360(6395):1339–1342, 2018.

[141] B Radha, Ali Esfandiar, FC Wang, AP Rooney, K Gopinadhan, Ashok Keerthi, Artem Mishchenko, Amritha Janardanan, Peter Blake, Laura Fumagalli, Marcelo Lozada-Hidalgo, Slaven Garaj, S.J. Haigh, I.V. Grigorieva, HengAn Wu, and Andre K. Geim. Molecular transport through capillaries made with atomic-scale precision. *Nature*, 538(7624):222–225, 2016.

[142] Lars Gunnar Moody Pettersson, Richard Humfry Henchman, and Anders Nilsson. Water–the most anomalous liquid. *Chem. Rev.*, 116(13):7459–7462, 2016.

[143] Gerardo Andrés Cisneros, Kjartan Thor Wikfeldt, Lars Ojamäe, Jibao Lu, Yao Xu, Hedieh Torabifard, Albert P Bartók, Gábor Csányi, Valeria Molinero, and Francesco Paesani. Modeling molecular interactions in water: From pairwise to many-body potential energy functions. *Chem. Rev.*, 116(13):7501–7528, 2016.

[144] Paola Gallo, Katrin Amann-Winkel, Charles Austen Angell, Mikhail Alexeevich Anisimov, Frédéric Caupin, Charusita Chakravarty, Erik Lascaris, Thomas Loerting, Athanassios Zois Panagiotopoulos, John Russo, Jonas Alexander Sellberg, Harry Eugene Stanley, Hajime Tanaka, Carlos Vega, Limei Xu, and Lars Gunnar Moody Pettersson. Water: A tale of two liquids. *Chem. Rev.*, 116(13):7463–7500, 2016.

[145] Michele Ceriotti, Wei Fang, Peter G Kusalik, Ross H McKenzie, Angelos Michaelides, Miguel A Morales, and Thomas E Markland. Nuclear quantum effects in water and aqueous systems: Experiment theory and current challenges. *Chem. Rev.*, 116(13):7529–7550, 2016.

[146] Nancy E Levinger. Water in confinement. *Science*, 298(5599):1722–1723, 2002.

[147] Silvina Cerveny, Francesco Mallamace, Jan Swenson, Michael Vogel, and Limei Xu. Confined water as model of supercooled water. *Chem. Rev.*, 116(13):7608–7625, 2016.

[148] Ramya H Tunuguntla, Robert Y Henley, Yun-Chiao Yao, Tuan Anh Pham, Meni Wanunu, and Aleksandr Noy. Enhanced water permeability and tunable ion selectivity in subnanometer carbon nanotube porins. *Science*, 357(6353):792–796, 2017.

[149] Oleg Byl, Jin-Chen Liu, Yang Wang, Wai-Leung Yim, J Karl Johnson, and John T Yates. Unusual hydrogen bonding in water-filled carbon nanotubes. *J. Am. Chem. Soc.*, 128(37):12090–12097, 2006.

[150] Gerhard Hummer, Jayendran C Rasaiah, and Jerzy P Noworyta. Water conduction through the hydrophobic channel of a carbon nanotube. *Nature*, 414(6860):188–190, 2001.

[151] Subramanian Vaitheeswaran, Jayendran C Rasaiah, and Gerhard Hummer. Electric field and temperature effects on water in the narrow nonpolar pores of carbon nanotubes. *J. Chem. Phys.*, 121(16):7955–7965, 2004.

[152] Jayendran C Rasaiah, Shekhar Garde, and Gerhard Hummer. Water in nonpolar confinement: From nanotubes to proteins and beyond. *Annu. Rev. Phys. Chem.*, 59:713–740, 2008.

[153] V Crupi, F Longo, D Majolino, and V Venuti. Vibrational properties of water molecules adsorbed in different zeolitic frameworks. *J. Phys. Condens. Matter*, 18(15):3563, 2006.

[154] Javier Carrasco, Andrew Hodgson, and Angelos Michaelides. A molecular perspective of water at metal interfaces. *Nat. Mater.*, 11(8):667–674, 2012.

[155] Martijn F De Lange, Karlijn JFM Verouden, Thijs JH Vlugt, Jorge Gascon, and Freek Kapteijn. Adsorption-driven heat pumps: The potential of metal–organic frameworks. *Chem. Rev.*, 115(22):12205–12250, 2015.

[156] Adam J Rieth, Ashley M Wright, Sameer Rao, Hyunho Kim, Alina D LaPotin, Evelyn N Wang, and Mircea Dincă. Tunable metal–organic frameworks enable high-efficiency cascaded adsorption heat pumps. *J. Am. Chem. Soc.*, 140(50):17591–17596, 2018.

[157] Casey R Wade, Tachmajal Corrales-Sanchez, Tarun C Narayan, and Mircea Dincă. Postsynthetic tuning of hydrophilicity in pyrazolate MOFs to modulate water adsorption properties. *Energy & Environmental Science*, 6(7):2172–2177, 2013.

[158] Adam J Rieth and Mircea Dincă. Controlled gas uptake in metal–organic frameworks with record ammonia sorption. *J. Am. Chem. Soc.*, 140(9):3461–3466, 2018.

[159] Hyunho Kim, Sungwoo Yang, Sameer R Rao, Shankar Narayanan, Eugene A Kapustin, Hiroyasu Furukawa, Ari S Umans, Omar M Yaghi, and Evelyn N Wang. Water harvesting from air with metal-organic frameworks powered by natural sunlight. *Science*, 356(6336):430–434, 2017.

[160] Adam J Rieth, Yuri Tulchinsky, and Mircea Dincă. High and reversible ammonia uptake in mesoporous azolate metal–organic frameworks with open mn co and ni sites. *J. Am. Chem. Soc.*, 138(30):9401–9404, 2016.

[161] Kui Tan, Sebastian Zuluaga, Qihan Gong, Pieremanuele Canepa, Hao Wang, Jing Li, Yves J Chabal, and Timo Thonhauser. Water reaction mechanism in metal organic frameworks with coordinatively unsaturated metal ions: MOF-74. *Chem. Mater.*, 26(23):6886–6895, 2014.

[162] Ashley M Wright, Adam J Rieth, Sungwoo Yang, Evelyn N Wang, and Mircea Dincă. Precise control of pore hydrophilicity enabled by post-synthetic cation exchange in metal–organic frameworks. *Chem. Sci.*, 9(15):3856–3859, 2018.

[163] Simona Dalla Bernardina, Erwan Paineau, Jean-Blaise Brubach, Patrick Judeinstein, Stéphan Rouzière, Pascale Launois, and Pascale Roy. Water in carbon nanotubes: The peculiar hydrogen bond network revealed by infrared spectroscopy. *J. Am. Chem. Soc.*, 138(33):10437–10443, 2016.

[164] JD Eaves, JJ Loparo, Ch J Fecko, ST Roberts, A Tokmakoff, and PL Geissler. Hydrogen bonds in liquid water are broken only fleetingly. *Proc. National Acad. Sci.*, 102(37):13019–13022, 2005.

[165] Quan Du, Eric Freysz, and Y Ron Shen. Surface vibrational spectroscopic studies of hydrogen bonding and hydrophobicity. *Science*, 264(5160):826–828, 1994.

[166] Shumei Sun, Fujie Tang, Sho Imoto, Daniel R Moberg, Tatsuhiko Ohto, Francesco Paesani, Mischa Bonn, Ellen HG Backus, and Yuki Nagata. Orientational distribution of free oh groups of interfacial water is exponential. *Phys. Rev. Lett.*, 121(24):246101, 2018.

[167] Francesco Paesani. Getting the right answers for the right reasons: Toward predictive molecular simulations of water with many-body potential energy functions. *Acc. Chem. Res.*, 49(9):1844–1851, 2016.

[168] Gregory R Medders and Francesco Paesani. Water dynamics in metal–organic frameworks: Effects of heterogeneous confinement predicted by computational spectroscopy. *J. Phys. Chem. Lett.*, 5(16):2897–2902, 2014.

[169] Zachary L Terranova, Matthew M Agee, and Francesco Paesani. Water structure and dynamics in homochiral [zn (l-l)(x)] metal–organic frameworks. *J. Phys. Chem. C*, 119(32):18239–18247, 2015.

[170] YLA Rezus and HJ Bakker. On the orientational relaxation of hdo in liquid water. *J. Chem. Phys.*, 123(11):114502, 2005.

[171] Kazimierz Krynicki, Christopher D Green, and David W Sawyer. Pressure and temperature dependence of self-diffusion in water. *Faraday Discuss. Chem. Soc.*, 66:199–208, 1978.

[172] Jeffrey R Errington and Pablo G Debenedetti. Relationship between structural order and the anomalies of liquid water. *Nature*, 409(6818):318–321, 2001.

[173] Michael A Henderson. The interaction of water with solid surfaces: Fundamental aspects revisited. *Surf. Sci. Rep.*, 46(1-8):1–308, 2002.

[174] Paul Kubelka and Franz Munk. An article on optics of paint layers. *Z. Tech. Phys*, 12(593-601):259–274, 1931.

[175] Leandro Martínez, Ricardo Andrade, Ernesto G Birgin, and José Mario Martínez. Packmol: A package for building initial configurations for molecular dynamics simulations. *J. Comput. Chem.*, 30(13):2157–2164, 2009.

[176] W Smith and TR Forester. Dl_poly_2. 0: A general-purpose parallel molecular dynamics simulation package. *J. Mol. Graph.*, 14(3):136–141, 1996.

[177] Mark E. Tuckerman. *Statistical Mechanics: Theory and Molecular Simulation*. Oxford University Press, 2010.

[178] Byung Hee Hong, Jin Yong Lee, Chi-Wan Lee, Jong Chan Kim, Sung Chul Bae, and Kwang S Kim. Self-assembled arrays of organic nanotubes with infinitely long one-dimensional h-bond chains. *J. Am. Chem. Soc.*, 123(43):10748–10749, 2001.

[179] Vipin Amoli, Joo Sung Kim, Eunsong Jee, Yoon Sun Chung, So Young Kim, Jehyoung Koo, Hanbin Choi, Yunah Kim, and Do Hwan Kim. A bioinspired hydrogen bond-triggered ultrasensitive ionic mechanoreceptor skin. *Nat. Commun.*, 10(1):1–13, 2019.

[180] Nitin Mehra, Madelyn Jeske, Xutong Yang, Junwei Gu, Marjan Alsadat Kashfipour, Yifan Li, Jessi Alan Baughman, and Jiahua Zhu. Hydrogen-bond driven self-assembly of two-dimensional supramolecular melamine-cyanuric acid crystals and its self-alignment in polymer composites for enhanced thermal conduction. *ACS Appl. Polym. Mater.*, 1(6):1291–1300, 2019.

[181] Yinyan Gong, Yan Xu, Yong Zhou, Can Li, Xinjuan Liu, Lengyuan Niu, Yongli Huang, Xi Zhang, and Chang Q Sun. Hydrogen bond network relaxation resolved by alcohol hydration (methanol ethanol and glycerol). *J. Raman Spectrosc.*, 48(3):393–398, 2017.

[182] Sunatda Arayachukiat, Chutima Kongtes, Alexander Barthel, Sai VC Vummaleti, Albert Poater, Sippakorn Wannakao, Luigi Cavallo, and Valerio D'Elia. Ascorbic acid as a bifunctional hydrogen bond donor for the synthesis of cyclic carbonates from co_2 under ambient conditions. *ACS Sustain. Chem. Eng.*, 5(8):6392–6397, 2017.

[183] Daniel Munoz-Santiburcio and Dominik Marx. Chemistry in nanoconfined water. *Chem. Sci.*, 8(5):3444–3452, 2017.

[184] Haoyuan Wang, Jackson C Wagner, Wenfan Chen, Chenglai Wang, and Wei Xiong. Spatially dependent h-bond dynamics at interfaces of water/biomimetic self-assembled lattice materials. *Proc. Natl. Acad. Sci. U.S.A.*, 117(38):23385–23392, 2020.

[185] Jiebo Li, Zhen Chi, Ruzhan Qin, Li Yan, Xubo Lin, Mingjun Hu, Guangcun Shan, Hailong Chen, and Yu-Xiang Weng. Hydrogen bond interaction promotes flash energy transport at mxene-solvent interface. *J. Phys. Chem. C*, 124(19):10306–10314, 2020.

[186] Fangfang He, Qian Wang, Cuifang Hu, Wen He, Xueying Luo, Ling Huang, Daojiang Gao, Jian Bi, Xin Wang, and Guohong Zou. Centrosymmetric $(nh_4)_2sbcl(so_4)_2$ and non-centrosymmetric $(nh_4)sbcl_2(so_4)$: Synergistic effect of hydrogen-bonding interactions and lone-pair cations on the framework structures and macroscopic centricities. *Cryst. Growth Des.*, 18(10):6239–6247, 2018.

[187] Changyou Shao, Huanliang Chang, Meng Wang, Feng Xu, and Jun Yang. High-strength tough and self-healing nanocomposite physical hydrogels based on the synergistic effects of dynamic hydrogen bond and dual coordination bonds. *ACS Appl. Mater. Interfaces*, 9(34):28305–28318, 2017.

[188] Haoyuan Wang, Wenfan Chen, Jackson C Wagner, and Wei Xiong. Local ordering of lattice self-assembled sds@2β-cd materials and adsorbed water revealed by vibrational sum frequency generation microscope. *J. Phys. Chem. B*, 123(29):6212–6221, 2019.

[189] Andrew W Knight, Nikolai G Kalugin, Eric Coker, and Anastasia G Ilgen. Water properties under nano-scale confinement. *Sci. Rep.*, 9(1):1–12, 2019.

[190] Sudip Chakraborty, Hemant Kumar, Chandan Dasgupta, and Prabal K Maiti. Confined water: Structure dynamics and thermodynamics. *Acc. Chem. Res.*, 50(9):2139–2146, 2017.

[191] Biswaroop Mukherjee, Prabal K Maiti, Chandan Dasgupta, and AK Sood. Jump reorientation of water molecules confined in narrow carbon nanotubes. *J. Phys. Chem. B*, 113(30):10322–10330, 2009.

[192] A Barati Farimani and Narayana R Aluru. Spatial diffusion of water in carbon nanotubes: From fickian to ballistic motion. *J. Phys. Chem. B*, 115(42):12145–12149, 2011.

[193] Steven A Yamada, Jae Yoon Shin, Ward H Thompson, and Michael D Fayer. Water dynamics in nanoporous silica: Utrafast vibrational spectroscopy and molecular dynamics simulations. *J. Phys. Chem. C*, 123(9):5790–5803, 2019.

[194] Howe-Siang Tan, Ivan R Piletic, and MD Fayer. Orientational dynamics of water confined on a nanometer length scale in reverse micelles. *J. Chem. Phys.*, 122(17):174501, 2005.

[195] Alessandra Scodinu and John T Fourkas. Comparison of the orientational dynamics of water confined in hydrophobic and hydrophilic nanopores. *J. Phys. Chem. B*, 106(40):10292–10295, 2002.

[196] Kenji Sumida, David L Rogow, Jarad A Mason, Thomas M McDonald, Eric D Bloch, Zoey R Herm, Tae-Hyun Bae, and Jeffrey R Long. Carbon dioxide capture in metal–organic frameworks. *Chem. Rev.*, 112(2):724–781, 2012.

[197] Rachel B Getman, Youn-Sang Bae, Christopher E Wilmer, and Randall Q Snurr. Review and analysis of molecular simulations of methane hydrogen and acetylene storage in metal–organic frameworks. *Chem. Rev.*, 112(2):703–723, 2012.

[198] Anastasiya Bavykina, Nikita Kolobov, Il Son Khan, Jeremy A Bau, Adrian Ramirez, and Jorge Gascon. Metal–organic frameworks in heterogeneous catalysis: Recent progress new trends and future perspectives. *Chem. Rev.*, 120(16):8468–8535, 2020.

[199] Timur Islamoglu, Zhijie Chen, Megan C Wasson, Cassandra T Buru, Kent O Kirlikovali, Unjila Afrin, Mohammad Rasel Mian, and Omar K Farha. Metal–organic frameworks against toxic chemicals. *Chem. Rev.*, 120(16):8130–8160, 2020.

[200] Dae-Woon Lim and Hiroshi Kitagawa. Proton transport in metal–organic frameworks. *Chem. Rev.*, 120(16):8416–8467, 2020.

[201] Mark D Allendorf, Renhao Dong, Xinliang Feng, Stefan Kaskel, Dariusz Matoga, and Vitalie Stavila. Electronic devices using open framework materials. *Chem. Rev.*, 120(16):8581–8640, 2020.

[202] Agnes E Thorarinsdottir and T David Harris. Metal–organic framework magnets. *Chem. Rev.*, 120(16):8716–8789, 2020.

[203] Farhad Fathieh, Markus J Kalmutzki, Eugene A Kapustin, Peter J Waller, Jingjing Yang, and Omar M Yaghi. Practical water production from desert air. *Sci. Adv.*, 4(6):eaat3198, 2018.

[204] Nikita Hanikel, Mathieu S Prévot, Farhad Fathieh, Eugene A Kapustin, Hao Lyu, Haoze Wang, Nicolas J Diercks, T Grant Glover, and Omar M Yaghi. Rapid cycling and exceptional yield in a metal-organic framework water harvester. *ACS Cent. Sci.*, 5(10):1699–1706, 2019.

[205] Zhijie Chen, Penghao Li, Xuan Zhang, Peng Li, Megan C Wasson, Timur Islamoglu, J Fraser Stoddart, and Omar K Farha. Reticular access to highly porous acs-MOFs with rigid trigonal prismatic linkers for water sorption. *J. Am. Chem. Soc.*, 141(7):2900–2905, 2019.

[206] JM Salazar, G Weber, JM Simon, I Bezverkhyy, and JP Bellat. Characterization of adsorbed water in MIL-53 (al) by ftir spectroscopy and ab-initio calculations. *J. Chem. Phys.*, 142(12):124702, 2015.

[207] Adam J Rieth, Kelly M Hunter, Mircea Dincă, and Francesco Paesani. Hydrogen bonding structure of confined water templated by a metal-organic framework with open metal sites. *Nat. Commun.*, 10(1):1–7, 2019.

[208] Jesse G McDaniel, Song Li, Emmanouil Tylianakis, Randall Q Snurr, and JR Schmidt. Evaluation of force field performance for high-throughput screening of gas uptake in metal–organic frameworks. *J. Phys. Chem. C*, 119(6):3143–3152, 2015.

[209] Tim M Becker, Azahara Luna-Triguero, Jose Manuel Vicent-Luna, Li-Chiang Lin, David Dubbeldam, Sofia Calero, and Thijs JH Vlugt. Potential of polarizable force fields for predicting the separation performance of small hydrocarbons in m-MOF-74. *Phys. Chem. Chem. Phys.*, 20(45):28848–28859, 2018.

[210] Tim M Becker, Li-Chiang Lin, David Dubbeldam, and Thijs JH Vlugt. Polarizable force field for co_2 in m-MOF-74 derived from quantum mechanics. *J. Phys. Chem. C*, 122(42):24488–24498, 2018.

[211] Shanelle Suepaul, Katherine A Forrest, Tony Pham, and Brian Space. Investigating the effects of linker extension on h_2 sorption in the rht-metal–organic framework nu-111 by molecular simulations. *Cryst. Growth Des.*, 18(12):7599–7610, 2018.

[212] Adam Hogan and Brian Space. Next-generation accurate transferable and polarizable potentials for material simulations. *J. Chem. Theory Comput.*, 16(12):7632–7644, 2020.

[213] Aurélie U Ortiz, Alexy P Freitas, Anne Boutin, Alain H Fuchs, and François-Xavier Coudert. What makes zeolitic imidazolate frameworks hydrophobic or hydrophilic? the impact of geometry and functionalization on water adsorption. *Phys. Chem. Chem. Phys.*, 16(21):9940–9949, 2014.

[214] Aisheng Huang, Wei Dou, and Jürgen Caro. Steam-stable zeolitic imidazolate framework ZIF-90 membrane with hydrogen selectivity through covalent functionalization. *J. Am. Chem. Soc.*, 132(44):15562–15564, 2010.

[215] Tingxu Yang and Tai-Shung Chung. Room-temperature synthesis of ZIF-90 nanocrystals and the derived nano-composite membranes for hydrogen separation. *J. Mater. Chem. A*, 1(19):6081–6090, 2013.

[216] Georg Kresse and Jürgen Hafner. Ab initio molecular dynamics for liquid metals. *Phys. Rev. B*, 47(1):558, 1993.

[217] Georg Kresse and Jürgen Hafner. Ab initio molecular-dynamics simulation of the liquid-metal–amorphous-semiconductor transition in germanium. *Phys. Rev. B*, 49(20):14251, 1994.

[218] Georg Kresse and Jürgen Furthmüller. Efficiency of ab-initio total energy calculations for metals and semiconductors using a plane-wave basis set. *Comput. Mater. Sci.*, 6(1):15–50, 1996.

[219] Georg Kresse and Jürgen Furthmüller. Efficient iterative schemes for ab initio total-energy calculations using a plane-wave basis set. *Phys. Rev. B*, 54(16):11169, 1996.

[220] John P Perdew, Kieron Burke, and Matthias Ernzerhof. Generalized gradient approximation made simple. *Phys. Rev. Lett.*, 77(18):3865, 1996.

[221] Stefan Grimme, Jens Antony, Stephan Ehrlich, and Helge Krieg. A consistent and accurate ab initio parametrization of density functional dispersion correction (dft-d) for the 94 elements h-pu. *J. Chem. Phys.*, 132(15):154104, 2010.

[222] Peter E Blöchl. Projector augmented-wave method. *Phys. Rev. B*, 50(24):17953, 1994.

[223] Georg Kresse and Daniel Joubert. From ultrasoft pseudopotentials to the projector augmented-wave method. *Phys. Rev. B*, 59(3):1758, 1999.

[224] Marc Riera, Eric P Yeh, and Francesco Paesani. Data-driven many-body models for molecular fluids: CO_2/H_2O mixtures as a case study. *J. Chem. Theory Comput.*, 16(4):2246–2257, 2020.

[225] Marc Riera, Alan Hirales, Raja Ghosh, and Francesco Paesani. Data-driven many-body models with chemical accuracy for CH_4/H_2O mixtures. *J. Phys. Chem. B*, 124(49):11207–11221, 2020.

[226] Jose LF Abascal and Carlos Vega. A general purpose model for the condensed phases of water: Tip4p/2005. *J. Chem. Phys.*, 123(23):234505, 2005.

[227] Francesco Paesani and Gregory A Voth. A quantitative assessment of the accuracy of centroid molecular dynamics for the calculation of the infrared spectrum of liquid water. *J. Chem. Phys.*, 132(1):014105, 2010.

[228] Mariana Rossi, Hanchao Liu, Francesco Paesani, Joel Bowman, and Michele Ceriotti. Communication: On the consistency of approximate quantum dynamics simulation methods for vibrational spectra in the condensed phase. *J. Chem. Phys.*, 141(18):181101, 2014.

[229] Frank Neese. The orca program system. *Wiley Interdiscip. Rev.: Comput. Mol. Sci.*, 2(1):73–78, 2012.

[230] Anne B McCoy. The role of electrical anharmonicity in the association band in the water spectrum. *J. Phys. Chem. B*, 118(28):8286–8294, 2014.

[231] George Trenins, Michael J Willatt, and Stuart C Althorpe. Path-integral dynamics of water using curvilinear centroids. *J. Chem. Phys.*, 151(5):054109, 2019.

[232] Sandeep K Reddy, Raphael Thiraux, Bethany A Wellen Rudd, Lu Lin, Tehseen Adel, Tatsuya Joutsuka, Franz M Geiger, Heather C Allen, Akihiro Morita, and Francesco Paesani. Bulk contributions modulate the sum-frequency generation spectra of water on model sea-spray aerosols. *Chem*, 4(7):1629–1644, 2018.

[233] Scott Habershon, Thomas E Markland, and David E Manolopoulos. Competing quantum effects in the dynamics of a flexible water model. *J. Chem. Phys.*, 131(2):024501, 2009.

[234] Mei-Hui Yu, Xiao-Ting Liu, Brian Space, Ze Chang, and Xian-He Bu. Metal-organic materials with triazine-based ligands: From structures to properties and applications. *Coord. Chem. Rev.*, 427:213518, 2021.

[235] Volodymyr Bon, Irena Senkovska, Jack D Evans, Michelle Wöllner, Markus Hölzel, and Stefan Kaskel. Insights into the water adsorption mechanism in the chemically stable zirconium-based MOF dut-67–a prospective material for adsorption-driven heat transformations. *J. Mater. Chem. A*, 7(20):12681–12690, 2019.

[236] Shyamapada Nandi, Himanshu Aggarwal, Mohammad Wahiduzzaman, Youssef Belmabkhout, Guillaume Maurin, Mohamed Eddaoudi, and Sabine Devautour-Vinot. Revisiting the water sorption isotherm of MOF using electrical measurements. *Chem. Commun.*, 55(88):13251–13254, 2019.

[237] Yunsong Li, Xinjiang Wang, Dongyan Xu, Jae Dong Chung, Massoud Kaviany, and Baoling Huang. H_2O adsorption/desorption in MOF-74: Ab initio molecular dynamics and experiments. *J. Phys. Chem. C*, 119(23):13021–13031, 2015.

[238] Marina V Solovyeva, Alexandr I Shkatulov, Larisa G Gordeeva, Elizaveta A Fedorova, Tamara A Krieger, and Yuri I Aristov. Water vapor adsorption on cau-10-x: Effect of functional groups on adsorption equilibrium and mechanisms. *Langmuir*, 37(2):693–702, 2021.

[239] Bingqiong Tan, Yanshu Luo, Xianghui Liang, Shuangfeng Wang, Xuenong Gao, Zhengguo Zhang, and Yutang Fang. One-pot synthesis of two-linker mixed al-based metal–organic frameworks for modulated water vapor adsorption. *Crystal Growth & Design*, 20(10):6565–6572, 2020.

[240] Kelly M Hunter, Jackson C Wagner, Mark Kalaj, Seth M Cohen, Wei Xiong, and Francesco Paesani. Simulation meets experiment: Unraveling the properties of water in metal–organic frameworks through vibrational spectroscopy. *J. Phys. Chem. C*, 125(22):12451–12460, 2021.

[241] Paul J Brimmer and Peter R Griffiths. Angular dependence of diffuse reflectance infrared spectra. part iii: Linearity of kubelka-munk plots. *Appl. Spectrosc.*, 42(2):242–247, 1988.

[242] Paul J Brimmer and Peter R Griffiths. Effect of absorbing matrixes on diffuse reflectance infrared spectra. *Anal. Chem.*, 58(11):2179–2184, 1986.

[243] Jinda Sirita, Sukon Phanichphant, and Frederic C Meunier. Quantitative analysis of adsorbate concentrations by diffuse reflectance ft-ir. *Anal. Chem.*, 79(10):3912–3918, 2007.

[244] Jill M Olinger and Peter R Griffiths. Quantitative effects of an absorbing matrix on near-infrared diffuse reflectance spectra. *Anal. Chem.*, 60(21):2427–2435, 1988.

[245] Fabrice Salles, Sandrine Bourrelly, Hervé Jobic, Thomas Devic, Vincent Guillerm, Philip Llewellyn, Christian Serre, Gérard Ferey, and Guillaume Maurin. Molecular insight into the adsorption and diffusion of water in the versatile hydrophilic/hydrophobic flexible mIL-53 (cr) MOF. *J. Phys. Chem. C*, 115(21):10764–10776, 2011.

[246] Pascal DC Dietzel, Rune E Johnsen, Richard Blom, and Helmer Fjellvåg. Structural changes and coordinatively unsaturated metal atoms on dehydration of honeycomb analogous microporous metal–organic frameworks. *Chem. Eur. J.*, 14(8):2389–2397, 2008.

[247] Nikita Hanikel, Xiaokun Pei, Saumil Chheda, Hao Lyu, WooSeok Jeong, Joachim Sauer, Laura Gagliardi, and Omar M Yaghi. Evolution of water structures in metal-organic frameworks for improved atmospheric water harvesting. *Science*, 374(6566):454–459, 2021.

[248] Hongda Zhang and Randall Q Snurr. Computational study of water adsorption in the hydrophobic metal–organic framework ZIF-8: Adsorption mechanism and acceleration of the simulations. *J. Phys. Chem. C*, 121(43):24000–24010, 2017.

[249] Paulo GM Mileo, Kyung Ho Cho, Jaedeuk Park, Sabine Devautour-Vinot, Jong-San Chang, and Guillaume Maurin. Unraveling the water adsorption mechanism in the mesoporous MIL-100 (fe) metal–organic framework. *J. Phys. Chem. C*, 123(37):23014–23025, 2019.

[250] Wen Hui Yin, Yang Yang Xiong, Hui Qiong Wu, Yuan Tao, Li Xiao Yang, Jian Qiang Li, Xiao Lan Tong, and Feng Luo. Functionalizing a metal–organic framework by a photoassisted multicomponent postsynthetic modification approach showing highly effective hg (ii) removal. *Inorg. Chem.*, 57(15):8722–8725, 2018.

[251] Feng-Ming Zhang, Hong Dong, Xin Zhang, Xiao-Jun Sun, Ming Liu, Dou-Dou Yang, Xin Liu, and Jin-Zhi Wei. Postsynthetic modification of ZFF-90 for potential targeted codelivery of two anticancer drugs. *ACS Applied Materials & Interfaces*, 9(32):27332–27337, 2017.

[252] Thorn A Dramstad, Zhihao Wu, Grace M Gretz, and Aaron M Massari. Thin films and bulk phases conucleate at the interfaces of pentacene thin films. *J. Phys. Chem. C*, 125(30):16803–16809, 2021.

[253] Gaia Neri, James Walsh, Gilberto Teobaldi, Paul M Donaldson, and Alexander J Cowan. Detection of catalytic intermediates at an electrode surface during carbon dioxide reduction by an earth-abundant catalyst. *Nat. Catal.*, 1(12):952–959, 2018.

[254] Hao Lu, Yu-Chieh Huang, Johannes Hunger, Denis Gebauer, Helmut Cölfen, and Mischa Bonn. Role of water in caco3 biomineralization. *J. Am. Chem. Soc.*, 143(4):1758–1762, 2021.

[255] Jiahui Zhang, Junjun Tan, Ruoqi Pei, Shuji Ye, and Yi Luo. Ordered water layer on the macroscopically hydrophobic fluorinated polymer surface and its ultrafast vibrational dynamics. *J. Am. Chem. Soc.*, 143(33):13074–13081, 2021.

[256] Stefan M Piontek, Mark DelloStritto, Bijoya Mandal, Tim Marshall, Michael L Klein, and Eric Borguet. Probing heterogeneous charge distributions at the α-Al_2O_3 (0001)/H_2O interface. *J. Am. Chem. Soc.*, 142(28):12096–12105, 2020.

[257] Prerna Sudera, Jenée D Cyran, Malte Deiseroth, Ellen HG Backus, and Mischa Bonn. Interfacial vibrational dynamics of ice ih and liquid water. *J. Am. Chem. Soc.*, 142(28):12005–12009, 2020.

[258] Cheng Wang, Teng Zhang, and Wenbin Lin. Rational synthesis of noncentrosymmetric metal–organic frameworks for second-order nonlinear optics. *Chem. Rev.*, 112(2):1084–1104, 2012.

[259] M Luke McDermott, Heather Vanselous, Steven A Corcelli, and Poul B Petersen. Dna's chiral spine of hydration. *ACS Central Sci.*, 3(7):708–714, 2017.

[260] Saranya Pullanchery and Sylvie Roke. Handy water: Chiral superstructures around peptide β-sheets. *Proc. National Acad. Sci.*, 118(2), 2021.

[261] Haoyuan Wang and Wei Xiong. Vibrational sum-frequency generation hyperspectral microscopy for molecular self-assembled systems. *Annu. Rev. Phys. Chem.*, 72:279–306, 2021.

[262] Benjamin Doughty, Yi Rao, Samuel W Kazer, Sheldon JJ Kwok, Nicholas J Turro, and Kenneth B Eisenthal. Probing the relative orientation of molecules bound to dna through controlled interference using second-harmonic generation. *Proc. National Acad. Sci.*, 110(15):5756–5758, 2013.

[263] Daniela Rodriguez, Maria D Marquez, Oussama Zenasni, Long T Han, Steven Baldelli, and T Randall Lee. Surface dipoles induce uniform orientation in contacting polar liquids. *Chem. Mater.*, 32(18):7832–7841, 2020.

[264] YR Shen. Surface properties probed by second-harmonic and sum-frequency generation. *Nature*, 337(6207):519–525, 1989.

[265] Haoyuan Wang, Tian Gao, and Wei Xiong. Self-phase-stabilized heterodyne vibrational sum frequency generation microscopy. *ACS Photonics*, 4(7):1839–1845, 2017.

[266] Takayuki Miyamae, Haruhisa Akiyama, Masaru Yoshida, and Nobuyuki Tamaoki. Characterization of poly (n-isopropylacrylamide)-grafted interfaces with sum-frequency generation spectroscopy. *Macromolecules*, 40(13):4601–4606, 2007.

[267] Xiaofan Xu, Y Ron Shen, and Chuanshan Tian. Phase-sensitive sum frequency vibrational spectroscopic study of air/water interfaces: H_2O D_2O and diluted isotopic mixtures. *J. Chem. Phys.*, 150(14):144701, 2019.

[268] Laura L Olenick, Julianne M Troiano, Nikolay Smolentsev, Paul E Ohno, Sylvie Roke, and Franz M Geiger. Polycation interactions with zwitterionic phospholipid monolayers on oil nanodroplet suspensions in water (d2o) probed by sum frequency scattering. *J. Phys. Chem. B*, 122(19):5049–5056, 2018.

[269] Guang Lu and Joseph T Hupp. Metal- organic frameworks as sensors: A ZIF-8 based fabry- pérot device as a selective sensor for chemical vapors and gases. *J. Am. Chem. Soc.*, 132(23):7832–7833, 2010.

[270] De-Sheng Zheng, Yuan Wang, An-An Liu, and Hong-Fei Wang. Microscopic molecular optics theory of surface second harmonic generation and sum-frequency generation spectroscopy based on the discrete dipole lattice model. *Int. Rev. Phys. Chem.*, 27(4):629–664, 2008.

[271] Ethan A Perets and Elsa CY Yan. Chiral water superstructures around antiparallel β-sheets observed by chiral vibrational sum frequency generation spectroscopy. *J. Phys. Chem. Lett.*, 10(12):3395–3401, 2019.

[272] Bruno G Nicolau, Natalia Garcıa-Rey, Bogdan Dryzhakov, and Dana D Dlott. Interfacial processes of a model lithium ion battery anode observed in situ with vibrational sum-frequency generation spectroscopy. *J. Phys. Chem. C*, 119(19):10227–10233, 2015.

[273] Shiang-Tai Lin, Prabal K Maiti, and William A Goddard III. Two-phase thermodynamic model for efficient and accurate absolute entropy of water from molecular dynamics simulations. *J. Phys. Chem. B*, 114(24):8191–8198, 2010.

[274] Shiang-Tai Lin, Mario Blanco, and William A Goddard III. The two-phase model for calculating thermodynamic properties of liquids from molecular dynamics: Validation for the phase diagram of lennard-jones fluids. *J. Chem. Phys.*, 119(22):11792–11805, 2003.

[275] Tod A Pascal, Shiang-Tai Lin, and William A Goddard III. Thermodynamics of liquids: Standard molar entropies and heat capacities of common solvents from 2pt molecular dynamics. *Phys. Chem. Chem. Phys.*, 13(1):169–181, 2011.

[276] Buddha Ratna Shrestha, Sreekiran Pillai, Adriano Santana, Stephen H Donaldson Jr, Tod A Pascal, and Himanshu Mishra. Nuclear quantum effects in hydrophobic nanoconfinement. *J. Phys. Chem. Lett.*, 10(18):5530–5535, 2019.

[277] Duo Wang, Diling Yang, Charley Huang, Yueying Huang, Dingzheng Yang, Hao Zhang, Qi Liu, Tian Tang, Mohamed Gamal El-Din, Tom Kemppi, Basil Perdicakis, and Hongbo Zeng. Stabilization mechanism and chemical demulsification of water-in-oil and oil-in-water emulsions in petroleum industry: A review. *Fuel*, 286:119390, 2021.

[278] Mesfin M Mekonnen and Arjen Y Hoekstra. Four billion people facing severe water scarcity. *Sci. Adv.*, 2(2):e1500323, 2016.

[279] Ariel Dinar, Amanda Tieu, and Helen Huynh. Water scarcity impacts on global food production. *Glob. Food Secur.*, 23:212–226, 2019.

[280] Maryam Salehi. Global water shortage and potable water safety; today's concern and tomorrow's crisis. *Environ. Int.*, 158:106936, 2022.

[281] Amir H Farmahini, Shreenath Krishnamurthy, Daniel Friedrich, Stefano Brandani, and Lev Sarkisov. Performance-based screening of porous materials for carbon capture. *Chem. Rev.*, 121(17):10666–10741, 2021.

[282] Marta Mon, Rosaria Bruno, Jesus Ferrando-Soria, Donatella Armentano, and Emilio Pardo. Metal–organic framework technologies for water remediation: Towards a sustainable ecosystem. *J. Mater. Chem. A*, 6(12):4912–4947, 2018.

[283] Cheng Wang, Bing An, and Wenbin Lin. Metal–organic frameworks in solid–gas phase catalysis. *ACS Catal.*, 9(1):130–146, 2018.

[284] Mengjie Hao, Muqing Qiu, Hui Yang, Baowei Hu, and Xiangxue Wang. Recent advances on preparation and environmental applications of MOF-derived carbons in catalysis. *Sci. Total. Environ.*, 760:143333, 2021.

[285] Ralph Freund, Orysia Zaremba, Giel Arnauts, Rob Ameloot, Grigorii Skorupskii, Mircea Dincă, Anastasiya Bavykina, Jorge Gascon, Aleksander Ejsmont, Joanna Goscianska, Markus Kalmutzki, Ulrich L achelt, Evelyn Ploetz, Christian S. Diercks, and Stefan Wuttke. The current status of MOF and COF applications. *Angew. Chem. Int. Ed.*, 60(45):23975–24001, 2021.

[286] Jian Zheng, Rama S Vemuri, Luis Estevez, Phillip K Koech, Tamas Varga, Donald M Camaioni, Thomas A Blake, B Peter McGrail, and Radha Kishan Motkuri. Pore-engineered metal–organic frameworks with excellent adsorption of water and fluorocarbon refrigerant for cooling applications. *J. Am. Chem. Soc.*, 139(31):10601–10604, 2017.

[287] Hyunho Kim, Sameer R Rao, Eugene A Kapustin, Lin Zhao, Sungwoo Yang, Omar M Yaghi, and Evelyn N Wang. Adsorption-based atmospheric water harvesting device for arid climates. *Nat. Commun.*, 9(1):1–8, 2018.

[288] Kyung Ho Cho, D Damasceno Borges, U Lee, Ji Sun Lee, Ji Woong Yoon, Sung June Cho, Jaedeuk Park, Walter Lombardo, Dohyun Moon, Alessio Sapienza, Guillaume Maurin, and Jong-San Chang. Rational design of a robust aluminum metal-organic framework for multi-purpose water-sorption-driven heat allocations. *Nat. Commun.*, 11(1):1–8, 2020.

[289] Lifeng Yang, Karam B Idrees, Zhijie Chen, Julia Knapp, Yongwei Chen, Xingjie Wang, Ran Cao, Xuan Zhang, Huabin Xing, Timur Islamoglu, and Omar K. Farha. Nanoporous water-stable zr-based metal–organic frameworks for water adsorption. *ACS Appl. Nano Mater.*, 4(5):4346–4350, 2021.

[290] Lu Wang, Kecheng Wang, Hao-Tian An, Hongliang Huang, Lin-Hua Xie, and Jian-Rong Li. A hydrolytically stable cu (ii)-based metal- organic framework with easily accessible ligands for water harvesting. *ACS Applied Materials & Interfaces*, 13(41):49509–49518, 2021.

[291] Wei Gong, Haomiao Xie, Karam B Idrees, Florencia A Son, Zhijie Chen, Fanrui Sha, Yan Liu, Yong Cui, and Omar K Farha. Water sorption evolution enabled by reticular construction of zirconium metal–organic frameworks based on a unique [2.2] paracyclophane scaffold. *J. Am. Chem. Soc.*, 2022.

[292] Jackson C Wagner, Kelly M Hunter, Francesco Paesani, and Wei Xiong. Water capture mechanisms at zeolitic imidazolate framework interfaces. *J. Am. Chem. Soc.*, 143(50):21189–21194, 2021.

[293] Alenka Luzar and David Chandler. Hydrogen-bond kinetics in liquid water. *Nature*, 379(6560):55–57, 1996.